

Development and characterization of solid oxide electrolysis cells  
based on zirconia and ceria based electrolyte for hydrogen production from steam



A Thesis Submitted in Partial Fulfillment of the Requirements  
for the Degree of Master of Engineering in Chemical Engineering

Department of Chemical Engineering

FACULTY OF ENGINEERING

Chulalongkorn University

Academic Year 2019

Copyright of Chulalongkorn University

การพัฒนาและการวิเคราะห์คุณลักษณะของเซลล์อิเล็กโทรไลซิสแบบออกไซด์ของแข็ง  
ที่ใช้อิเล็กโทรไลต์ชนิดซีเรียและเซอร์โคเนียเป็นฐานสำหรับผลิตไฮโดรเจนจากไอน้ำ



วิทยานิพนธ์นี้เป็นส่วนหนึ่งของการศึกษาตามหลักสูตรปริญญาวิศวกรรมศาสตรมหาบัณฑิต  
สาขาวิชาวิศวกรรมเคมี ภาควิชาวิศวกรรมเคมี  
คณะวิศวกรรมศาสตร์ จุฬาลงกรณ์มหาวิทยาลัย  
ปีการศึกษา 2562  
ลิขสิทธิ์ของจุฬาลงกรณ์มหาวิทยาลัย

Thesis Title	Development and characterization of solid oxide electrolysis cells based on zirconia and ceria based electrolyte for hydrogen production from steam
By	Miss Parintorn Temluxame
Field of Study	Chemical Engineering
Thesis Advisor	Assistant Professor Pattaraporn Kim, Ph.D.

---

Accepted by the FACULTY OF ENGINEERING, Chulalongkorn University in  
Partial Fulfillment of the Requirement for the Master of Engineering

..... Dean of the FACULTY OF  
ENGINEERING  
(Professor SUPOT TEACHAVORASINSKUN, D.Eng.)

THESIS COMMITTEE

..... Chairman  
(Professor MUENDUEN PHISALAPHONG, Ph.D.)

..... Thesis Advisor  
(Assistant Professor Pattaraporn Kim, Ph.D.)

..... Examiner  
(Professor SUTTICHAJ ASSABUMRUNGRAT, Ph.D.)

..... External Examiner  
(Pramote Puengjinda, Ph.D.)

ปริญญ์ เต็มลักษณะมี : การพัฒนาและการวิเคราะห์คุณลักษณะของเซลล์อิเล็กโทรไลต์แบบออกไซด์ของแข็ง ที่ใช้อิเล็กโทรไลต์ชนิดซีเรียและเซอร์โคเนียเป็นฐานสำหรับผลิตไฮโดรเจนจากไอน้ำ. ( Development and characterization of solid oxide electrolysis cells based on zirconia and ceria based electrolyte for hydrogen production from steam) อ.ที่ปรึกษาหลัก : ผศ. ดร.ภัทรพร คิม

งานวิจัยนี้ศึกษาการแยกสลายโมกุลไอน้ำด้วยไฟฟ้าสำหรับการผลิตไฮโดรเจนในเซลล์อิเล็กโทรไลต์แบบออกไซด์ของแข็ง (SOEC) สแกนเดียมไอออน ซีเรียมไอออน และแกโดลิเนียมไอออนถูกเจือลงในเซอร์โคเนีย (SCGZ) และเปรียบเทียบกับอิเล็กโทรไลต์ชนิดเซอร์โคเนียเจือด้วยอิตเทรียม (YSZ) และซีเรียเจือด้วยแกโดลิเนียม (GDC) เซลล์ชนิดที่มีอิเล็กโทรไลต์เป็นฐานถูกเตรียมขึ้น อิเล็กโทรไลต์ชนิด SCGZ และ YSZ มีความหนาแน่นสูง โดยมีค่าความหนาแน่นสัมพัทธ์มากกว่า 95% ในขณะที่ GDC มีความหนาแน่นน้อยกว่า ค่าพลังงานก่อกัมมันต์ของการนำของ SCGZ มีค่าต่ำที่สุดที่ 65.58 กิโลจูลต่อโมล แต่อย่างไรก็ตามการเปลี่ยนแปลงเฟสจะถูกตรวจพบภายหลังขั้นตอนการสังเคราะห์อิเล็กโทรไลต์ชนิดนี้ เซลล์ชนิดที่มีขั้วแคโทดเป็นฐานที่ประกอบด้วย SCGZ เป็นอิเล็กโทรไลต์ (Ni-SCGZ/SCGZ/BSCF) แสดงความสามารถทางไฟฟ้าเคมีที่สูงที่สุด ทำการทดสอบความทนทานของเซลล์ในระบบอิเล็กโทรไลต์เป็นเวลา 60 ชั่วโมง (ที่กระแสไฟฟ้า 0.3 แอมป์ต่อตารางเซนติเมตร อุณหภูมิ 800 องศาเซลเซียส และอัตราส่วนไอน้ำต่อไฮโดรเจนเท่ากับ 70:30) เซลล์ Ni-GDC/YSZ/GDC/BSCF เสื่อมความสามารถอย่างรวดเร็ว (0.0057 โวลต์ต่อชั่วโมง) ในขณะที่ความสามารถของเซลล์ชนิด Ni-YSZ/YSZ/BSCF และ Ni-SCGZ/SCGZ/BSCF ค่อนข้างเสถียรภายใต้สภาวะปฏิบัติการเดียวกัน ขั้ว BSCF ยังคงยึดติดกับอิเล็กโทรไลต์ชนิด SCGZ และไม่พบการเปลี่ยนแปลงเฟสเพิ่มเติมภายหลังการทดสอบ แต่อย่างไรก็ตามการคงเสถียรภาพของเฟสชนิดควิบิกซึ่งเป็นเฟสที่มีค่าการนำสูงใน SCGZ ด้วยการเติม 1-2% โดยโมลของบิสมาทออกไซด์ลงใน SCGZ ได้ถูกตรวจสอบ โดยพบว่าบิสมาทออกไซด์ประพุดิตัวเป็นทั้งสารที่เพิ่มเสถียรภาพของเฟสและสารที่ช่วยในการเผาผลาญอิเล็กโทรไลต์ นอกจากนี้ค่าการนำไอออนของอิเล็กโทรไลต์ยังได้รับการปรับปรุงด้วยการเติมบิสมาทออกไซด์อีกด้วย

สาขาวิชา วิศวกรรมเคมี  
ปีการศึกษา 2562

ลายมือชื่อนิสิต .....  
ลายมือชื่อ อ.ที่ปรึกษาหลัก .....

# # 6170209121 : MAJOR CHEMICAL ENGINEERING

KEYWORD: Solid oxide electrolysis cell, Hydrogen, Steam electrolysis,  
Scandium, Zirconia, Bismuth oxide, Phase transformation

Parintorn Temluxame : Development and characterization of solid oxide electrolysis cells based on zirconia and ceria based electrolyte for hydrogen production from steam. Advisor: Asst. Prof. Pattaraporn Kim, Ph.D.

Steam electrolysis for hydrogen production is investigated in solid oxide electrolysis cell (SOEC).  $\text{Sc}^{3+}$ ,  $\text{Ce}^{4+}$ , and  $\text{Gd}^{3+}$  are doped in zirconia (SCGZ) and compared with yttria stabilized zirconia (YSZ) and gadolinium doped ceria (GDC) electrolyte. Electrolyte-supported cells are fabricated. The SCGZ and YSZ electrolytes are dense with >95% relative density while GDC is less densified. The activation energy of conduction of the SCGZ electrolyte is the lowest at  $65.58 \text{ kJ mol}^{-1}$  although phase transformation is detected after electrolyte fabrication process. Cathode-supported cell having SCGZ electrolyte (Ni-SCGZ/SCGZ/BSCF) shows the highest electrochemical performance. Durability test of the cells in electrolysis mode is carried out over 60 h ( $0.3 \text{ A cm}^{-2}$ ,  $800 \text{ }^\circ\text{C}$ ,  $\text{H}_2\text{O}$  to  $\text{H}_2$  ratio of 70:30). Significant performance degradation of Ni-GDC/YSZ/GDC/BSCF cell is observed ( $0.0057 \text{ V h}^{-1}$ ) whereas the performance of Ni-YSZ/YSZ/BSCF and Ni-SCGZ/SCGZ/BSCF are rather stable under the same operating conditions. The BSCF remains attaching to the SCGZ electrolyte and additional phase transformation is not observed after prolong operation. However, stabilization of high conducting cubic phase by adding 1-2 mol% of  $\text{Bi}_2\text{O}_3$  in SCGZ is also investigated.  $\text{Bi}_2\text{O}_3$  is found to act as both phase stabilizer and sintering aid. In addition, the ionic conductivity of the electrolyte is also improved with adding  $\text{Bi}_2\text{O}_3$ .

Field of Study: Chemical Engineering

Student's Signature .....

Academic Year: 2019

Advisor's Signature .....

## ACKNOWLEDGEMENTS

My deep and sincere gratitude goes first to my thesis advisor, Assistant Professor Pattaraporn Kim, for all the opportunities and invaluable help throughout university life. Her enthusiasm, indomitable spirit, and patient support have deeply inspired me and pushed me to this far. I would not through difficult times and this thesis would not have been completed without all the support that I have always received from her. It was a great chance in my life to work and study under her guidance.

Besides my advisor, I would like to thank Professor Muenduen Phisalaphong, as a chairman, and the rest of my thesis committee: Professor Suttichai Assabumrungrat, Dr. Pramote Puengjinda, for their insightful comment and their valuable guidance on my research.

My sincere thanks also go to PTT Public Company Limited team for their supports, professional guidance, and useful recommendations on this project; I also thank the Thailand Science Research and Innovation (TSRI), and National Science and Technology Development Agency (NSTDA) for support and the STEM Workforce scholarship.

My appreciation also extends to my colleagues and the technicians in the laboratory of the Center of Excellence on Catalysis and Catalytic Reaction Engineering (CECC) for providing assistance in handling with the instrument and analyzing data.

In addition, I would like to thank my parents for their sympathetic ear and continuous encouragement, especially my father, who always sacrifices his valuable time and personal happiness to facilitate me throughout this research. Finally, I could not have completed this dissertation without the support from my special friend, who always be my happiness among the stressful circumstances.

Parintorn Temluxame

## TABLE OF CONTENTS

	Page
ABSTRACT (THAI).....	iii
ABSTRACT (ENGLISH).....	iv
ACKNOWLEDGEMENTS .....	v
TABLE OF CONTENTS .....	vi
LIST OF TABLES.....	ix
LIST OF FIGURES .....	xi
CHAPTER I INTRODUCTION.....	1
1.1 Background.....	1
1.2 Objective.....	3
1.3 Scope of study .....	4
1.4 Expected benefits.....	5
CHAPTER II THEORY AND LITERATURE REVIEW .....	6
2.1 Theory .....	6
2.1.1 Hydrogen characteristics .....	6
2.1.2 General principles of solid oxide electrolysis cell.....	7
2.2 Literature reviews.....	11
2.2.1 Electrolyte materials.....	11
2.2.1.1 Stabilized zirconia .....	13
2.2.1.2 Ceria-based oxide.....	20
2.2.2 Electrode materials .....	22
2.2.2.1 Cathode (Fuel electrode).....	22

2.2.2.1.1 Effect of nickel content.....	25
2.2.2.1.2 Effect of Pore former .....	27
2.2.2.2 Anode (Oxygen electrode) .....	28
2.2.3 Operating conditions.....	31
CHAPTER III EXPERIMENTAL.....	35
3.1 Chemicals and equipment.....	35
3.1.1 Chemicals.....	35
3.1.2 Tool and equipment.....	36
3.2 Experimental.....	37
3.2.1 Electrolyte-supported cells fabrication .....	37
3.2.2 Cathode-supported cells fabrication.....	39
3.2.3 Electrochemical performance measurement.....	42
3.2.4 Characterization .....	43
CHAPTER IV RESULTS AND DISCUSSION .....	45
4.1 Phase and microstructure analysis of electrolyte.....	45
4.2 Activation energy of conduction.....	51
4.3 Electrochemical performance of electrolyte-supported cells.....	53
4.4 Microstructure analysis of Ni-SCGZ/SCGZ/BSCF cathode-supported cell.....	56
4.5 Electrochemical performance of cathode-supported cell.....	57
4.5.1 Performance discrepancy between the electrolysis and galvanic modes .....	57
4.5.2 Effect of temperature.....	60
4.5.3 Effect of steam content at hydrogen electrode .....	61
4.5.4 Durability test.....	62



4.6 Oxidation tolerance of Ni-electrolyte.....	64
4.7 Rhombohedral phase suppression for SCGZ electrolyte .....	66
4.7.1 Phase analysis and microstructure .....	67
4.7.2 Electrochemical performance measurement.....	75
4.7.3 Structural stability test .....	79
CHAPTER V CONCLUSIONS AND RECOMENDATIONS.....	83
5.1 Conclusions.....	83
5.2 Recommendations.....	84
REFERENCES .....	86
APPENDIX.....	100
APPENDIX A LATTICE PARAMETER AND CELL PROPERTIES CALCULATION .....	101
APPENDIX B ELECTROCHEMICAL MEASUREMENT CONDITION.....	105
APPENDIX C ELECTROCHEMICAL CALCULATION .....	106
VITA.....	110

## LIST OF TABLES

	Page
<b>Table 1</b> Hydrogen and other fuels properties.....	7
<b>Table 2</b> Electrolyzer type .....	8
<b>Table 3</b> Phase analysis of $\text{Sc}_2\text{O}_3\text{-ZrO}_2$ system .....	16
<b>Table 4</b> Ionic conductivity of different ceria-based electrolyte .....	20
<b>Table 5</b> Properties of SOEC electrolyte.....	21
<b>Table 6</b> Properties of SOEC anode .....	30
<b>Table 7</b> Effect of sintering temperature and pressing pressure on the volume shrinkage and relative density of GDC, YSZ, and SCGZ electrolyte.....	49
<b>Table 8</b> Parameters extracted from the EIS response of Pt/electrolyte/Pt operating at controlled potential of 1.1 V, temperature of 800 °C, and $\text{H}_2\text{O}:\text{H}_2$ ratio of 70:30 the cathode chamber and ambient air at the anode chamber.....	54
<b>Table 9</b> Parameters extracted from the EIS response of Ni-SCGZ/SCGZ/BSCF in electrolytic (1.1 V) and galvanic modes (0.6 V) at temperature of 800 °C and $\text{H}_2\text{O}:\text{H}_2$ ratio of 70:30 the cathode chamber and ambient air at the anode chamber.....	59
<b>Table 10</b> $\text{H}_2$ production rate of Ni-electrolyte/electrolyte/BSCF operating at varied applied potential 0.9-1.8 V at 800 °C under $\text{H}_2\text{O}$ to $\text{H}_2$ ratio of 70:30 at the cathode and ambient air at the anode.....	60
<b>Table 11</b> The XRD peak area ratio of the rhombohedral to the cubic phase (sintered SCGZ electrolyte at 1300 °C and 1450 °C for 4 hours).....	68
<b>Table 12</b> The percentages of volume shrinkage and relative density of 0-2 mol% $\text{Bi}_2\text{O}_3$ -doped SCGZ electrolyte at different sintering temperatures .....	72
<b>Table 13</b> Average grain size of the sintered SCGZ electrolyte with and without $\text{Bi}_2\text{O}_3$ doping (1-2 mol%).....	74

<b>Table 14</b> The parameters obtained from the EIS response of Pt/SCGZ/Pt and Pt/2Bi10SCGZ/Pt at operating temperature of 800 °C under potentiostatic mode of 1.1 V and H <sub>2</sub> O:H <sub>2</sub> ratio of 70:30 .....	78
<b>Table A.1</b> The calculated data of spacing of the crystal layers ( $d_{hk}$ ) for 1Bi10SCGZ	103
<b>Table A.2</b> The calculated data of lattice parameter for 1Bi10SCGZ .....	103
<b>Table B.1</b> Gas flow rate to cathode at varied H <sub>2</sub> O:H <sub>2</sub> from 60:40 to 90:10.....	105



## LIST OF FIGURES

	Page
Fig. 1 Thermodynamic of electrolysis.....	9
Fig. 2 Schematic of a solid oxide electrolysis cell (SOEC).....	10
Fig. 3 Operation modes of high temperature steam electrolysis (HTE).....	10
Fig. 4 SEM image of suitable electrolyte structure (Left) cross-sectional view of Ni-GDC/YSZ/GDC/LSM-YSZ (Right) Top view of 1 wt% ZnO-BSC electrolyte.....	12
Fig. 5 (Left) Effect of temperature (Right) or electrolyte thickness on ASR .....	12
Fig. 6 Relationship between ionic conductivity at 1000 °C and association enthalpies as a function of dopant cation radius .....	13
Fig. 7 Effect of dopant concentration on electrolyte ionic conductivity .....	14
Fig. 8 Effect of temperature on oxygen ion conductivity of zirconia electrolyte.....	15
Fig. 9 a binary $ZrO_2$ - $Sc_2O_3$ phase diagram .....	16
Fig. 10 Arrhenius plot of ionic conductivities for ScSZ.....	17
Fig. 11 XRD patterns of 11ScSZ powders calcined 4 hours at various temperatures..	18
Fig. 12 SEM micrographs of ScSZ sintered at (a) 800 °C (b) 900 °C (c) 1000 °C (d) 1100 °C for 4 hours.....	18
Fig. 13 XRD patterns of 10ScSZ-doped with different amount of $Bi_2O_3$ sintered at 1300 °C for 2 hours .....	20
Fig. 14 Effect of dopant concentration on GDC ionic conductivity .....	21
Fig. 15 (Left) Triple-phase boundary and (Right) SEM image of Ni/YSZ electrode .....	23
Fig. 16 Electrical conductivity of Ni/10ScSZ as a function of Ni content and sintering temperature.....	25
Fig. 17 Porosity variation as a function of sinter temperature of Ni/10Sc1CeSZ .....	26
Fig. 18 Porosity of cathode substrate as a function of pore former content.....	27

<b>Fig. 19</b> Electrical conductivity of cathode as a function of porosity .....	28
<b>Fig. 20</b> ASR of BSCF in comparison with other oxygen electrode materials.....	31
<b>Fig. 21</b> IV curve of Ni-YSZ at different temperature and inlet gas compositions.....	32
<b>Fig. 22</b> IV curves in SOEC mode as a function of gas feed to electrode at 900 °C.....	33
<b>Fig. 23</b> Hydrogen production rate of BSCF and LSM as a function of voltages .....	33
<b>Fig. 24</b> Electrolyte-supported cells fabrication .....	38
<b>Fig. 25</b> Electrolyte-supported cells (cross-sectional view).....	39
<b>Fig. 26</b> Electrolyte-supported cells (Pt/YSZ/GDC/Pt cross-sectional view) .....	39
<b>Fig. 27</b> Cathode-supported cells fabrication .....	41
<b>Fig. 28</b> Cathode-supported cells (cross-sectional view).....	41
<b>Fig. 29</b> Cathode-supported cells (Ni-GDC/YSZ/GDC/BSCF cross-sectional view) .....	41
<b>Fig. 30</b> platinum wire attachment for an electrical connection.....	42
<b>Fig. 31</b> Schematic drawing of the test system .....	42
<b>Fig. 32</b> X-ray diffraction pattern: (top) SCGZ electrolyte powder (bottom) magnified peak over $2\theta$ ranging from $45^\circ$ to $56^\circ$ .....	46
<b>Fig. 33</b> X-ray diffraction pattern: (top) sintered SCGZ electrolyte (bottom) magnified peak over $2\theta$ ranging from $46^\circ$ to $56^\circ$ .....	47
<b>Fig. 34</b> Images of different electrolyte pellets after sintering.....	48
<b>Fig. 35</b> SEM images of (a) GDC sintered at 1300 °C, (b) YSZ sintered at 1450 °C, (c) SCGZ sintered at 1450 °C, and (d) cross-sectional image of the bi-layered GDC/YSZ electrolyte.....	50
<b>Fig. 36</b> SEM images of GDC electrolyte sintered at (a) 1200 °C, (b) 1250 °C, (c) 1300 °C, (d) 1350 °C, (d) 1400 °C, and (e) 1450 °C .....	51
<b>Fig. 37</b> Activation energy of conduction ( $E_a$ ) and the conductivity of Bi-layered GDC/YSZ, YSZ and SCGZ electrolyte at various operating temperatures.....	51

<b>Fig. 38</b> The EIS response of Pt/electrolyte/Pt at controlled potential of 1.1 V, operating temperature of 800 °C, and H <sub>2</sub> O:H <sub>2</sub> ratio of 70:30 at the cathode chamber and ambient air at the anode chamber .....	53
<b>Fig. 39</b> I/V response of Pt/electrolyte/Pt when the electrolyte is Bi-layered GDC/YSZ, YSZ and SCGZ, under H <sub>2</sub> O:H <sub>2</sub> ratio of 70:30 at the cathode chamber and ambient air at the anode chamber .....	56
<b>Fig. 40</b> SEM image of (a) Ni-SCGZ electrode, (b) SCGZ electrolyte, and (c) cross-sectional image of Ni-SCGZ/SCGZ/BSCF layers .....	57
<b>Fig. 41</b> I/V response of Ni-electrolyte/electrolyte/BSCF when the electrolyte was Bi-layered GDC/YSZ, YSZ and SCGZ, operated at 800 °C under H <sub>2</sub> O to H <sub>2</sub> of 70:30 at the cathode and ambient air at the anode .....	58
<b>Fig. 42</b> The EIS response of Ni-SCGZ/SCGZ/BSCF in electrolytic (1.1 V) and galvanic modes (0.6 V) at 800 °C under H <sub>2</sub> O:H <sub>2</sub> ratio of 70:30 at the cathode chamber and ambient air at the anode chamber .....	59
<b>Fig. 43</b> The I/V response of Ni-SCGZ/SCGZ/BSCF at varied operating temperatures from 600 °C to 900 °C (H <sub>2</sub> O:H <sub>2</sub> of 70:30 at the cathode chamber and ambient air at the anode chamber).....	61
<b>Fig. 44</b> The I/V response of Ni-SCGZ/SCGZ/BSCF at varied steam to hydrogen from 60:40 to 90:10 at 800 °C.....	62
<b>Fig. 45</b> Potential monitoring of cathode-supported cells under electrolysis condition (0.3 A cm <sup>-2</sup> for Ni-GDC/YSZ/GDC/BSCF, Ni-YSZ/YSZ/BSCF and Ni-SCGZ/SCGZ/BSCF, 800 °C, H <sub>2</sub> O:H <sub>2</sub> = 70:30, 60 h).....	63
<b>Fig. 46</b> SEM images of (a) Ni-SCGZ electrode, (b) SCGZ electrolyte, and (c) cross-sectional image of Ni-SCGZ/SCGZ/BSCF layers after durability test .....	63
<b>Fig. 47</b> X-ray diffraction pattern after durability test: (top) sintered SCGZ electrolyte (bottom) magnified peak over 2θ ranging from 46° to 56°.....	64
<b>Fig. 48</b> The oxidation of Ni-electrolyte (GDC/YSZ, SCGZ and YSZ) cermet at 800 °C in air .....	65

<b>Fig. 49</b> TGA/DSC of electrolyte powder (GDC, SCGZ and YSZ).....	66
<b>Fig. 50</b> The XRD patterns of the SCGZ pellets sintered at 500 °C to 1450 °C.....	67
<b>Fig. 51</b> Magnified scale of the XRD pattern of the SCGZ sintered at 1100-1450 °C.....	68
<b>Fig. 52</b> SEM images of the SCGZ electrolyte sintered at varied temperatures: (a) 1300 °C; (b) 1350 °C; (c) 1400 °C; and (d) 1450 °C.....	69
<b>Fig. 53</b> The XRD patterns of (a) the SCGZ with different Bi <sub>2</sub> O <sub>3</sub> contents, sintered at 1450 °C (b) magnified scale over 2θ ranging from 59.5° to 61°.....	69
<b>Fig. 54</b> The XRD peak area ratio of rhombohedral to cubic phase in SCGZ with different Bi <sub>2</sub> O <sub>3</sub> concentrations, sintered at 1450 °C for 4 hours.....	71
<b>Fig. 55</b> SEM images of 1 mol% Bi <sub>2</sub> O <sub>3</sub> -doped SCGZ at different sintering temperatures: (a) 1300 °C; (b) 1350 °C; (c) 1400 °C; and (d) 1450 °C.....	73
<b>Fig. 56</b> SEM images of 2 mol% Bi <sub>2</sub> O <sub>3</sub> -doped SCGZ at different sintering temperatures: (a) 1300 °C; (b) 1350 °C; (c) 1400 °C; and (d) 1450 °C.....	73
<b>Fig. 57</b> Grain size distribution of SCGZ (left) and 2Bi10SCGZ (right) sintered at 1350 °C.....	75
<b>Fig. 58</b> Activation energy of conduction (E <sub>a</sub> ) and the conductivity of SCGZ sintered at 1450 °C and 2Bi10SCGZ sintered at 1350 °C.....	76
<b>Fig. 59</b> EIS response of Pt/SCGZ/Pt and Pt/2Bi10SCGZ/Pt at operating temperature of 800 °C under potentiostatic mode of 1.1 V and H <sub>2</sub> O:H <sub>2</sub> ratio of 70:30.....	78
<b>Fig. 60</b> I/V curve of Pt/SCGZ/Pt and Pt/2Bi10SCGZ/Pt at operating temperature of 800 °C under steam electrolysis and H <sub>2</sub> O:H <sub>2</sub> ratio of 70:30.....	79
<b>Fig. 61</b> The XRD patterns of: (a) SCGZ sintered at 1450 °C; (b) 2Bi10SCGZ sintered at 1350 °C before and after annealing (800 °C for 48 hours); (c) the magnified scale over 2θ ranging from 59.5° to 61° of SCGZ sintered at 1450 °C after annealing; and, (d) 2Bi10SCGZ sintered at 1350 °C after annealing.....	80

- Fig. 62** SEM images of the electrolyte after annealing at 800°C for 48 hours: (a) SCGZ sintered at 1450 °C, (b) 2Bi10SCGZ sintered at 1350 °C; and EDX-mapping of 2Bi10SCGZ sintered at 1350 °C (c) before and (d) after annealing..... 81
- Fig. 63** TGA/DSC of electrolyte powder (SCGZ and 2Bi10SCGZ) ..... 82
- Fig. A.1** XRD patterns of the SCGZ with different Bi<sub>2</sub>O<sub>3</sub> contents sintered at 1450 °C. .... 102
- Fig. C.1** I/V response of Pt/electrolyte/Pt when the electrolyte is Bi-layered GDC/YSZ, YSZ and SCGZ, under H<sub>2</sub>O:H<sub>2</sub> ratio of 70:30 at 800 °C..... 106
- Fig. C.2** Activation energy of conduction (E<sub>a</sub>) and the conductivity of Bi-layered GDC/YSZ, YSZ and SCGZ electrolyte at various operating temperatures..... 108





# CHAPTER I

## INTRODUCTION

### 1.1 Background

Global demand for energy is significantly increasing nowadays in accordance with the rate of population and economic growth in all aspects, i.e., economic, social and cultural. This is also a key factor that Thailand relies massively on energy to be a driving force for the economy and various systems development. Regarding this issue, the development of energy technology has gained much attention and continually requires more research and development. Alternative energy technology has also considered as one of the topics in National Economic and Social Development Plan to increase energy efficiency and reducing energy demand.

The global hydrogen ( $H_2$ ) demand has been continuous increases each year for a wide range of applications, i.e., in food, metal, glass and chemical industries. Hydrogen is also one of alternative energy carriers with high energy content and is expected to play important role in the future. However, majority of hydrogen is currently produced from hydrocarbon-based feedstock, which is limited resources, creating the challenging situations for a country reliance on imports of refining crude oil to help meet the petroleum demand. Moreover,  $H_2$  production from hydrocarbon feedstock generates carbon dioxide ( $CO_2$ ) emission which is a significant contributor to global warming. Developing effective and affordable methods for producing hydrogen with less damage to the environment is a goal of the hydrogen economy.

Steam electrolysis in solid oxide electrolysis cell (SOEC) is among  $H_2$  production methods which can utilize of water to produce syngas ( $H_2$ ), as presented in Eqs. (1)-(3). Steam can be converted into  $H_2$  through an electrochemical reaction. Pure  $H_2$  can be produced without the need for further processing to remove

impurities. If the electricity required for this process is derived from renewable energy sources, then this represents a low carbon route to H<sub>2</sub> production.



In this device, the product can be controlled by controlling the amount of electricity input in the process. Moreover, the high operating temperatures of electrolysis reaction reduce the electricity requirement in process and permit to using of the industrial wasted heat from other industrial processes to operate, resulting in lower production costs which can be compared to the traditional hydrogen production method.

The importance of this project focuses on H<sub>2</sub> production through electrochemical operation of solid oxide electrolysis cell (SOEC). This will encourage sustainable energy and support a carbon-neutral society.

However, energy demand for electrolysis process is a major issue relating implementation of SOEC and H<sub>2</sub>/syngas production cost. Therefore, the challenge of the research is to increase performance and durability of the SOEC. Electrolyte is one important part to determine SOEC performance. Generally, 8 mol% yttria stabilized zirconia (YSZ) is widely used as the electrolyte in solid oxide fuel cell and has been also applied for SOEC due to high stability property of zirconia-based material. Comparing to YSZ, ceria-based material such as trivalent doped ceria can provide relatively higher ionic conductivity. However, the ceria-based material still exhibits low stability due to the reduction of Ce<sup>4+</sup> to Ce<sup>3+</sup> under low oxygen partial pressure [1-3]. Therefore, it is of interest to optimize both high oxygen conductivity and chemical stability resulting in a material that simultaneously meets all the requirements for SOEC electrolyte. With an attempt to optimize both ionic conductivity from zirconia and chemical stability from ceria, Scandium, cerium and gadolinium doped zirconia (Sc<sub>0.1</sub>Ce<sub>0.005</sub>Gd<sub>0.005</sub>Zr<sub>0.89</sub>O<sub>2</sub>, SCGZ) electrolyte for SOEC was

studied in this research, comparing with 8 mol% yttria-stabilized zirconia ( $Y_{0.08}Zr_{0.92}O_2$ , YSZ) and gadolinium doped ceria ( $Gd_{0.1}Ce_{0.9}O_{1.9}$ , GDC) electrolyte.

In this work, suitable SOEC electrolytes including: scandium cerium gadolinium doped zirconia, yttria stabilize zirconia, and gadolinium doped ceria were investigated for used in solid oxide electrolysis cell. Crystalline phase of sintered electrolyte was investigated to detect the low conducting phase in which result to the cell degradation problems. Electrolyte-supported cells were fabricated to determine electrolyte performances in terms of conductivity as a function of temperature and activation energy of conduction. Cathode-supported cells of Ni-electrolyte/electrolyte/BSCF ( $Ba_{0.5}Sr_{0.5}Co_{0.8}Fe_{0.2}O_3$ ) were also fabricated to assess the cell performance and durability. The electrochemical performance of the cells over a range of steam partial pressures and temperatures including the discrepancy between the electrolysis and galvanic modes were investigated, as well as the cell microstructure before and after SOEC operation. Degradation characteristics, as well as oxidation tolerance, of cathode-supported cells were compared. In addition, 1-2 mol% of bismuth oxide ( $Bi_2O_3$ ) doped in SCGZ electrolyte were also studied, comparing to the bare SCGZ. The phase stabilization, sintering behavior, and electrochemical performance over a range of temperatures were investigated, through the fabricated electrolyte-supported cells. Decreasing unwanted low conducting phase, lowering sintering temperature, and increasing ion conductivity were expected in the presence of  $Bi_2O_3$ .

## 1.2 Objective

To investigate and develop the performance and durability of SOEC electrolyte including: scandium cerium gadolinium doped zirconia, yttria stabilize zirconia, and gadolinium doped ceria, for used in solid oxide electrolysis cell for hydrogen production through steam electrolysis.

### 1.3 Scope of study

1.3.1 Determine an appropriate electrolyte material consisting of  $\text{Sc}_{0.1}\text{Ce}_{0.005}\text{Gd}_{0.005}\text{Zr}_{0.89}\text{O}_2$  (SCGZ),  $\text{Y}_{0.08}\text{Zr}_{0.92}\text{O}_2$  (YSZ) and  $\text{Gd}_{0.1}\text{Ce}_{0.9}\text{O}_{1.9}$  (GDC).

1.3.2 Study electrolyte materials properties which are purity of substances, crystalline phase of sintered electrolytes, particle sizes, and surface areas.

1.3.3 Fabricate electrolyte- and cathode-supported cells by mold and press, and dip-coating technique.

1.3.4 Determine appropriate conditions to fabricate electrolyte-supported cells, consisting of the effect of sintering temperature and effect of pressing pressure on structure.

1.3.5 Study electrolyte-supported cells properties after fabrication process including cell microstructure, grain size, relative density, linear shrinkage, and volume shrinkage.

1.3.6 Measure electrolyte performances in term of the conductivity of SOEC electrolyte by using current/voltage measurement (I/V curve), electrochemical impedance spectroscopy (EIS) and calculation of activation energy.

1.3.7 Comparatively study the oxidation tolerance of Ni-electrolyte cathode.

1.3.8 Use  $\text{Ba}_{0.5}\text{Sr}_{0.5}\text{Co}_{0.8}\text{Fe}_{0.2}\text{O}_3$  (BSCF) as an anode in cathode support cells.

1.3.9 Measure cells performance toward hydrogen production from  $\text{H}_2\text{O}$  and  $\text{H}_2$  by using current/voltage measurement (I/V curve) and electrochemical impedance spectroscopy (EIS) and degradation characteristic.

1.3.10 Study cathode-supported cells properties after SOEC operation including phase stabilization, cell microstructure, grain size, and cell delamination and phase stabilization.

1.3.11 Determine appropriate condition to increase hydrogen production, i.e., steam to hydrogen ratio ( $\text{H}_2\text{O}:\text{H}_2$ ), operating temperature and applied voltage.

1.3.12 Determine 1-2 mol% bismuth oxide ( $\text{Bi}_2\text{O}_3$ ) doped in SCGZ electrolyte through the fabricated electrolyte-supported cell.

## 1.4 Expected benefits

1.4.1 Obtain oxide-conducting electrolyte for SOEC with high performance in terms of chemically stability and ionic conductivity.

1.4.2 Increase H<sub>2</sub> potential to play a key role in a clean, secure and affordable energy.

1.4.3 Reduce environmental problems caused by CO<sub>2</sub> emissions from H<sub>2</sub> production from petroleum-based feedstock.



## CHAPTER II

### THEORY AND LITERATURE REVIEW

#### 2.1 Theory

This part aims to provide characteristics of hydrogen which is future potential energy including with a background on fuel cells, particularly solid oxide electrolysis cell (SOEC) which is taken as the pollutant-free production method for hydrogen in this study.

##### 2.1.1 Hydrogen characteristics

Hydrogen ( $H_2$ ) has been considered as a clean, practical and potential energy source for the future. It has a high energy content compared with other fuels, and it also can be converted to other usable energy. In order to store hydrogen, it can be stored by compressed under low pressure or by underground storage. Furthermore, it can be safely distributed or transported by pipeline, rail or truck [4]. Therefore, hydrogen is a good choice for alternative fuel. Details of the physical and chemical properties of hydrogen and other fuel are summarized in Table 1.

Hydrogen primarily uses today is by industry, namely: ammonia production, urea production and cracking of petrochemicals [5]. Even though hydrogen is the most abundant element in nature, it is mostly combined with other elements, therefore, Energy usage is always occurred in the hydrogen production [4]. Presently, most of this hydrogen is produced from various fossil fuels such as natural gas oil and coal through one of the various ways: steam reforming, gasification, partial oxidation [5]. Natural gas steam reforming has become the commercial cheapest method of producing hydrogen [4]. However, this method depends on a limit fossil fuel and liberate carbon dioxide leading to elimination of demand for using hydrogen. Therefore, thermochemical water splitting, photocatalytic water splitting or water electrolysis have become an interesting process which is the pollutant-free

hydrogen production methods. The electrolysis of water is the best production way to produce hydrogen because of comparable cost with the traditional process if electricity from industrial or renewable sources is utilized.

**Table 1** Hydrogen and other fuels properties [4, 6]

Property	Hydrogen	Methanol	Ethanol	Automotive gasoline
Molecular weight (g mol <sup>-1</sup> )	2.02	32.04	46.06	~107.00
Density at 20°C and 1 atm (kg m <sup>-3</sup> )	0.084	791	789	751
Normal boiling point (°C)	-252.8	64.5	78.5	27-225
CO <sub>2</sub> production (per energy unit)	0	1.5	-	1.8
Energy Content (MJ kg <sup>-1</sup> )	120	19.7	29.6	46.4

### 2.1.2 General principles of solid oxide electrolysis cell

Production of hydrogen for use as alternative fuels is currently an interesting topic since the amount of use of hydrogen continues to increase with the rate of economic and social growth. Electrolysis is a promising well-known process to split water (H<sub>2</sub>O) into hydrogen (H<sub>2</sub>) and oxygen (O<sub>2</sub>) by using electrical energy. Purification procedures (Purification process) is not needed for this method [7]. For this reason, the cost of hydrogen production can be decreased. There are mainly two types of electrolyzer consist of low temperature electrolyzer (LTE) and high temperature electrolyzer (HTE). Their characteristics are summarized in Table 2.

**Table 2** Electrolyzer type [4],[7]

Property	Alkaline	PEM	SOEC
Electrolyte	KOH	Polymer	Ceramic
Operating temperature	50-200 °C	50-100 °C	500-1000 °C
Charge carrier	OH <sup>-</sup>	H <sup>+</sup>	O <sup>2-</sup>
Efficiency and cost	80%, Lowest	94.4%, Highest	90%, Medium

The major problem of LTE, such as alkaline (AFC) and proton exchange membrane (PEM), is the slow reaction rate [7]. In addition, high electrical power is required due to low operating temperature according to equation (4).

$$\Delta H = \Delta G + T\Delta S \quad (4)$$

Where the minimum electric energy demand for electrolysis is equal to Gibbs free energy change ( $\Delta G$ ),  $\Delta H$  is the enthalpy change and  $T\Delta S$  is the thermal energy requirements of the process ( $\text{J mol}^{-1} \text{H}_2$ ).

Although all energy requirements do not vary with the operating temperature as given in Fig. 1. However, the electrical energy requirement,  $\Delta G$ , decreases with increasing temperature. Therefore, high temperature electrolyzer can decrease the cost of hydrogen production, particularly if the heat energy demand can be integrated with the external heat sources, such as the use of waste heat sources from other industries (500-750 degree Celsius) [8], nuclear power (500-750 degree Celsius) [9], and renewable energy.



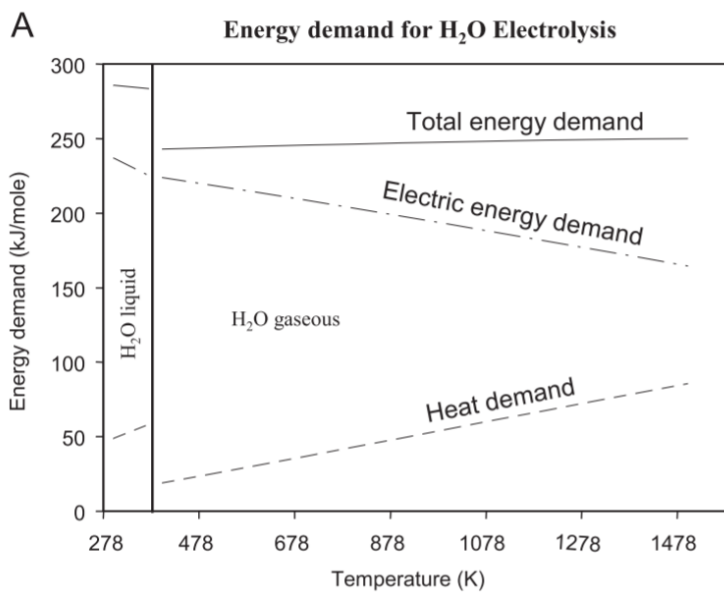


**Fig. 1** Thermodynamic of electrolysis [10]

SOEC is a high temperature electrolyzer which operates in the region of 500-1000 degree Celsius [7]. Therefore, the high reaction rate can be achieved without expensive catalysts. Solid oxide electrolysis cell (SOEC) is a reverse reaction of “solid oxide fuel cell” that is an electrochemical device that converts chemical energy into electrical energy directly. The schematic diagrams of oxygen ion conductor for SOEC is depicted in Eq. (5-7) and Fig. 2.

Negative electrode, H<sub>2</sub> electrode :



Positive electrode, O<sub>2</sub> electrode :



Overall reaction :



For oxygen ion conductor, water is converted to steam using thermal and electrical energy, and then supply to cathode to form hydrogen (H<sub>2</sub>) as well as oxygen ion (O<sup>2-</sup>). After that, oxygen ion migrates through electrolyte to form oxygen molecules at the anode surface.

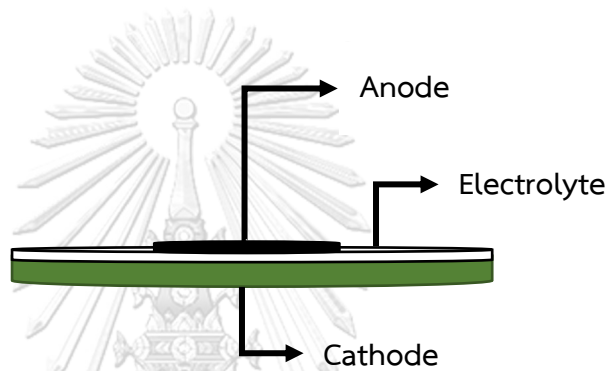
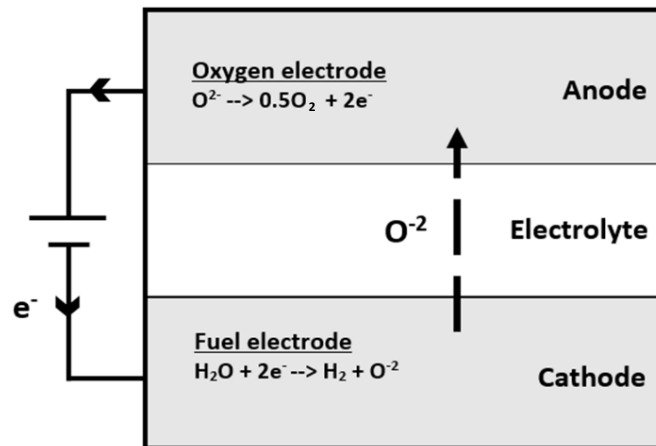


Fig. 2 Schematic of a solid oxide electrolysis cell (SOEC)

Thermodynamically, SOEC can operate isothermally at three different modes depending on an operating voltage which consist of thermoneutral, endothermic and exothermic [11, 12], as shown in Fig. 3.

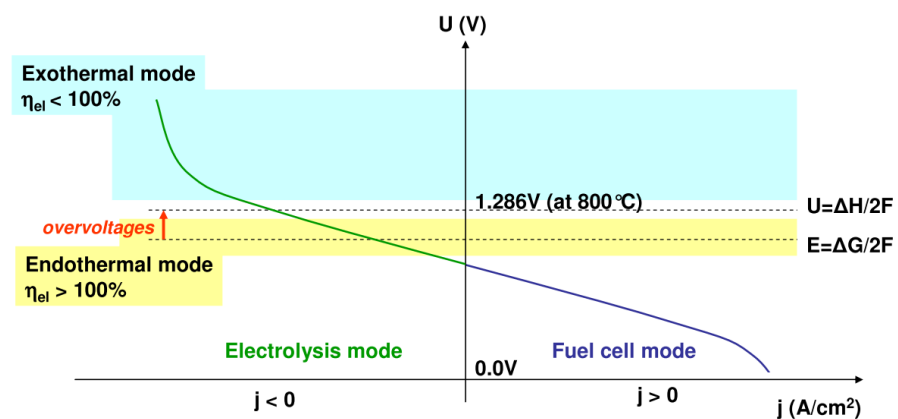


Fig. 3 Operation modes of high temperature steam electrolysis (HTE)

In the thermoneutral mode, the heat demand to dissociate water equals the heat released within the cell, therefore external heat supply is not required. In the endothermic mode, the operating voltage is low leading to low heat caused than the reaction requires. Thus, external heat is required to maintain the temperature. The merit of this process is to attain long-term degradation rates due to low power densities. Finally, In the exothermic mode, the heat from large overpotential is more than the reaction required, thereby it is necessary to remove to maintain a constant operating temperature. The advantage of this process is exceeding energy can be used again in the system to preheat the inlet gas.

## 2.2 Literature reviews

Literature review relating to the solid oxide electrolysis cell for hydrogen synthesis has been done focusing on efficiently, highly capable and durable of the cell. The review is divided into three parts. The first and second parts are electrolyte material and electrode material, relating increasing the cell efficiency to achieve high conductivity under operating temperatures through material selection. The last part is SOEC operating conditions relating to the effect of reaction conditions, including operating temperature, the proportion of the feed gases and the electric potential focusing on creating high current with low resistance.

### 2.2.1 Electrolyte materials

Electrolyte is the key component of SOEC. Electrolyte materials should be chemically stable together with good ionic conductivity to reach a high energy conversion efficiency. The dense and thin electrolyte must be required to prohibit the recombination of  $H_2$  and  $O_2$ , and minimize the ohmic overpotential. In addition, the electrical conductivity of electrolytes should negligible at the cell operating temperature. The availability of electronic conduction will lower the ionic conduction of electrolytes [13]. Suitable electrolyte microstructure analyzed by scanning electron microscopy (SEM) was shown in Fig. 4.

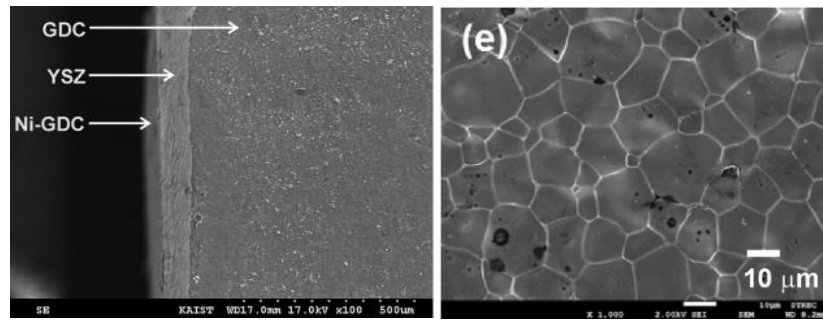


Fig. 4 SEM image of suitable electrolyte structure (Left) cross-sectional view of Ni-GDC/YSZ/GDC/LSM-YSZ (Right) Top view of 1 wt% ZnO-BSC electrolyte [1]

As presented in Fig. 4, the suitable electrolyte should have no open pores along the electrolyte layer (GDC, YSZ) and grain boundary. The large grain size of electrolyte structure represents the low grain boundary density which normally inhibit the ion mobility in oxygen vacancies leading to lower ion conductivity of electrolyte, as shown in Fig. 4(Right). Moreover, the large grain size also represents the denser electrolyte enhancing the ability to prohibit gas recombination in SOEC operation. Therefore, the large grain size microstructure of electrolyte is required.

Theoretically, the electrolyte performance depends mainly on operation temperature, thickness, and material properties. High operation temperature is required to increase the ionic conductivity of the materials, while higher electrolyte thickness will increase the area-specific resistance (ASR) as shown in Fig. 5.

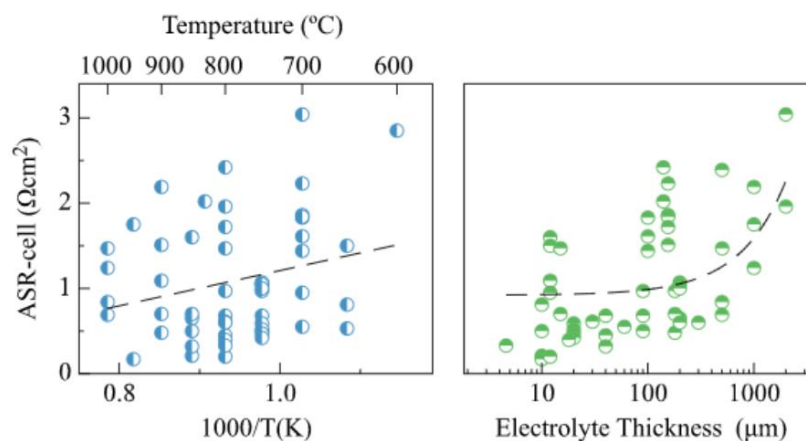
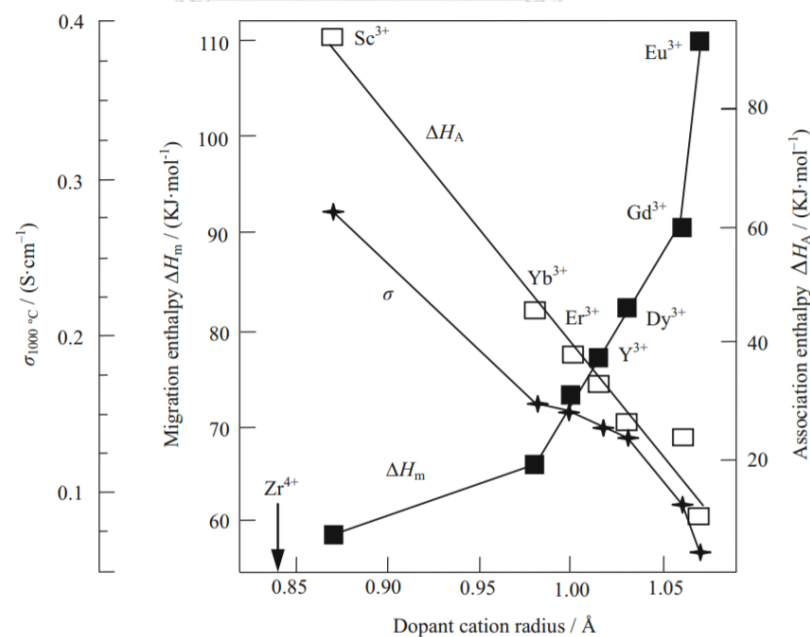


Fig. 5 (Left) Effect of temperature (Right) or electrolyte thickness on ASR [14]

In case of material properties, there are many types of oxygen ion conducting electrolytes. It can be divided commonly used electrolytes into two parts: stabilized zirconia and ceria-based oxides.

### 2.2.1.1 Stabilized zirconia

Zirconium dioxide has a high melting point about 2700°C, however, the phase transformation from monoclinic to tetragonal occurred around 1100°C resulting in volume change [15]. This undesirable phase transformation can be prevented by stabilization of cubic structure with some alkaline-earth or rare-earth oxide. There are reported that these dopants can increase the amount of oxygen vacancies, affecting to increase the conductivity of oxygen ion [16]. Fig. 6 presents the relationship between ionic conductivity and dopant ionic radius. It can be seen that among  $\text{Y}_2\text{O}_3$ ,  $\text{Yb}_2\text{O}_3$ , and  $\text{Sc}_2\text{O}_3$ ,  $\text{Sc}_2\text{O}_3$  dopant exhibits high conductivity when doping into zirconia material. Because the ionic radius of  $\text{Sc}^{3+}$  is more close to that of  $\text{Zr}^{4+}$ , therefore, the distortion of the lattice by the substitution of  $\text{Sc}^{3+}$  for  $\text{Zr}^{4+}$  does not significantly affect the migration of oxygen ions [17, 18].



**Fig. 6** Relationship between ionic conductivity at 1000 °C and association enthalpies as a function of dopant cation radius [19]

Moreover, kilner and brook [18] reports that the ionic size mismatch relates to the association enthalpy as presented in Fig. 6. The association enthalpy varies with dopant radius, agreeing well with the trend towards lower value of activation energy ( $E_a$ ) when dopant radius approaches to zirconia host radius. Due to the increasing ionic radius, the lattice will be in high strain energy from large ionic mismatch. Therefore, less energy is required for the strain compensated pair and hence the association enthalpy decrease with dopant ionic radius [20].

The ionic conductivity of electrolyte also depends on the concentration of dopants, as shown in Fig. 7.

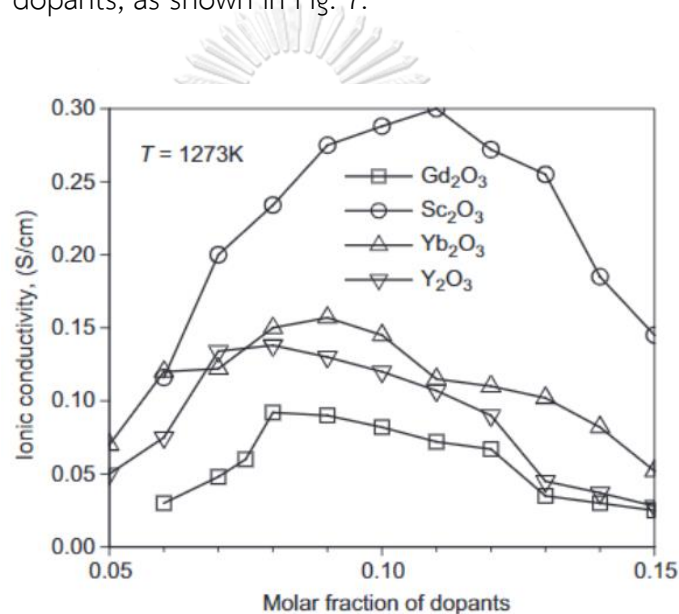
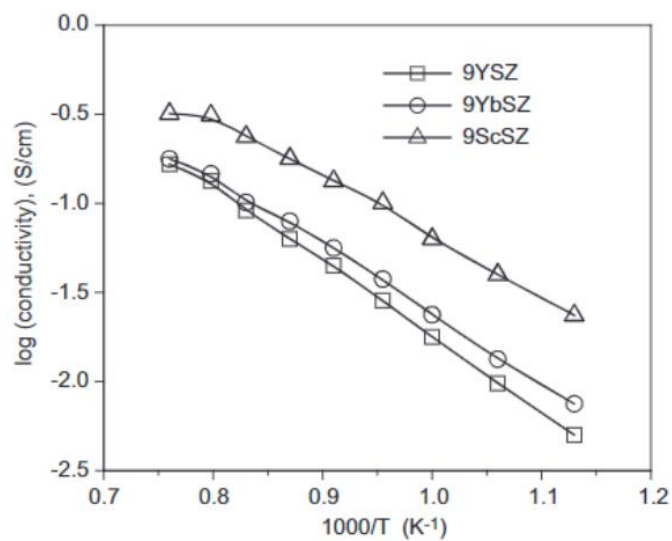


Fig. 7 Effect of dopant concentration on electrolyte ionic conductivity [21]

As presented in Fig. 7, the oxygen vacancies are increased with the concentration of dopants, resulting in higher conductivity. However, the formation of defect associates between oxygen ion vacancies and dopant cations will occur at high dopant concentrations which can turn the results into lower conductivity [22]. The maximum oxygen ion conductivity (about  $0.3 \text{ S cm}^{-1}$  at  $1000^\circ\text{C}$ ) of ScSZ (Scandia stabilized zirconia) can be obtained when the molar fraction of  $\text{Sc}_2\text{O}_3$  is around 8-12%. In case of YSZ (Yttria-stabilized zirconia), the maximum oxygen ion conductivity of YSZ was observed around 8% molar fraction of  $\text{Y}_2\text{O}_3$  which is the lowest solubility limit of  $\text{Y}_2\text{O}_3$  in  $\text{ZrO}_2$  [19].

8% mol Ytria-stabilized zirconia (YSZ) is the most common electrolyte material for SOEC operation due to its high oxygen ion conductivity, good mechanical strength and much more economical [16]. Nevertheless, there are some reports on alternative electrolyte materials due to limitation of YSZ at lower temperatures. Fig. 8 shows the effect of temperature on oxygen ion conductivity of 9YSZ, 9YbSZ, and 9ScSZ.

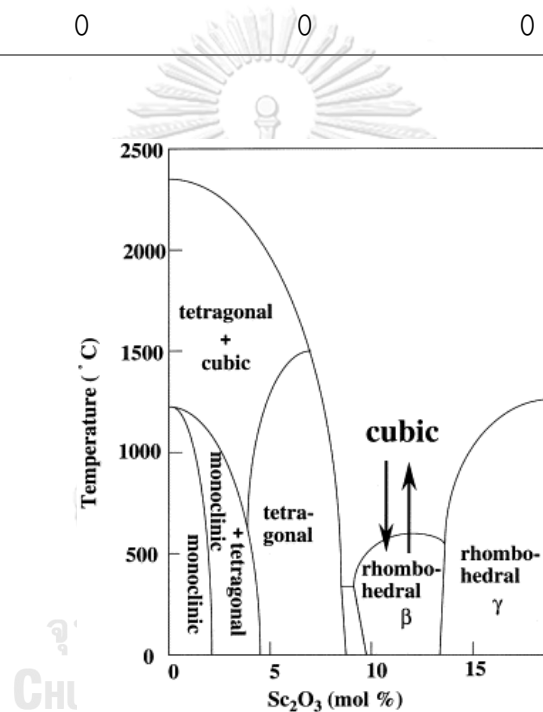


**Fig. 8** Effect of temperature on oxygen ion conductivity of zirconia electrolyte [23]

The conductivity of oxygen increases in following order: YSZ < YbSZ < ScSZ. ScSZ exhibited a large difference among other electrolytes at low temperatures. Therefore, it can indicate that ScSZ can be used as an intermediate-temperature electrolyte, resulting in lower energy cost. Even though ScSZ exhibited higher conductivity than YSZ, it more suffers from degradation during long term operation than YSZ. Yamamoto et al. [24] reports that the conductivity of as-sintered 8ScSZ decrease with time from  $0.24 \text{ S cm}^{-1}$  to  $0.13 \text{ S cm}^{-1}$  after 2000 hours due to the phase transition to poorly conducting phase (rhombohedral  $\beta$ -phase,  $\text{Sc}_2\text{ZrO}_{17}$ ). The room temperature XRD results of ScSZ electrolyte as a function of  $\text{Sc}_2\text{O}_3$  concentration, including with a binary  $\text{ZrO}_2$ - $\text{Sc}_2\text{O}_3$  phase diagram, are summarized as shown in Table 3 and Fig. 9.

**Table 3** Phase analysis of  $\text{Sc}_2\text{O}_3\text{-ZrO}_2$  system [24]

Composition $\text{Sc}_2\text{O}_3$ mol%	Phase			
	Monoclinic	Tetragonal	Cubic	Rhombohedral
2.9	0	100	0	0
4.9	0	89	11	0
7.8	0	67	33	0
8.0	0	0	100	0
11.0	0	0	0	100
12.0	0	0	0	100

**Fig. 9** a binary  $\text{ZrO}_2\text{-Sc}_2\text{O}_3$  phase diagram [25]

It was found that when doping amount of  $\text{Sc}_2\text{O}_3$  more than 10% mol on  $\text{ZrO}_2$ , the  $\text{Sc}_2\text{O}_3\text{-ZrO}_2$  system exhibits cubic phase at high temperature and transforms into rhombohedral phase at low temperature [26]. Therefore, the volume change of about 0.15% is observed, leading to crack or delamination of electrode from electrolyte [27]. For electrochemical properties, the conductivity of rhombohedral phase is lower than cubic phase. Thus, the conductivity at low temperature is lower due to the presence of rhombohedral phase leading the temperature conductivity relationship follow an Arrhenius equation is broken, as



shown in Fig. 10 [28]. Moreover, the driving force for homogeneous distribution of cation in ScSZ is very weak, resulting in a poor sintering property [29]. It can be seen that the ScSZ direct usage as an electrolyte seems to be prohibited.

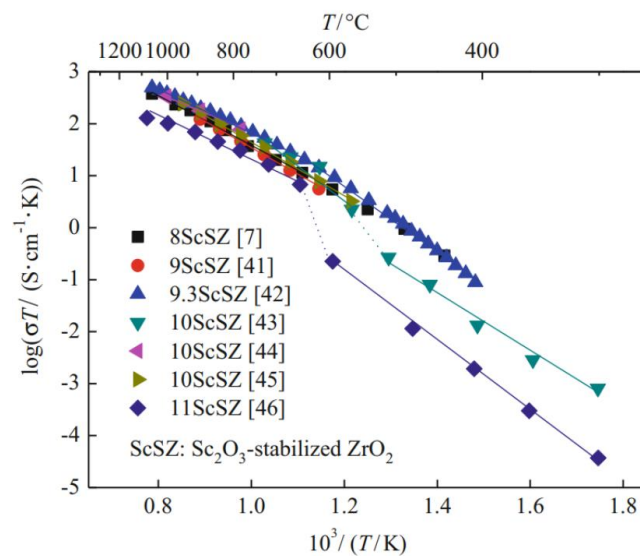


**Fig. 10** Arrhenius plot of ionic conductivities for ScSZ [28]

According to this problem, many studies have been conducted to stabilize the cubic phase of  $\text{Sc}_2\text{O}_3\text{-ZrO}_2$  system. There are reported that even high sintering temperatures provide larger grain size for electrolyte structure, the phase transformation undergoes in  $\text{Sc}_2\text{O}_3\text{-ZrO}_2$  system at this condition. It is therefore of great way to achieve cubic phase stability by lowering sintering temperature of electrolyte, as presented in Fig. 11. From XRD patterns of 11ScSZ, the sintered powder at 1100 °C exhibited the rhombohedral phase peak together with high conducting cubic phase peak, while the powder sintered at lower temperature than 900 °C are all in cubic phase structure [30]. It can be seen that rhombohedral  $\beta$ -phase peak was not detected at low sintering temperature.

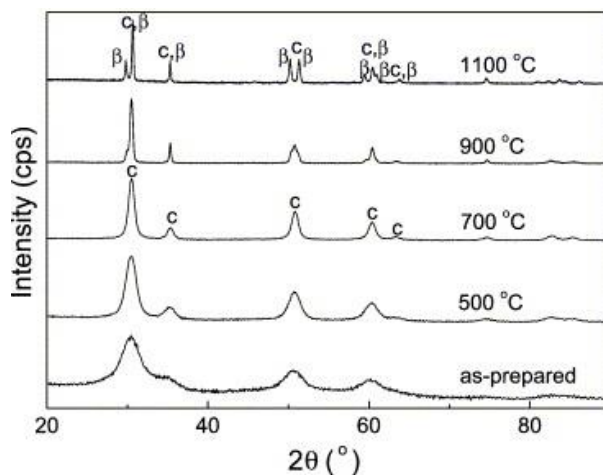


**Fig. 11** XRD patterns of 11ScSZ powders calcined 4 hours at various temperatures [30]

However, with low sintering temperature, the low densification electrolyte structure is unavoidable, noticed by SEM micrographs as presented in Fig. 12. The average grain size of 0.3  $\mu\text{m}$  was achieved for 11ScSZ sintered at 1100  $^{\circ}\text{C}$  [30]. While sintering at 900  $^{\circ}\text{C}$  and 800  $^{\circ}\text{C}$ , the average grain size decreased down to 80 and 30 nm, respectively, affecting ion conductivity.

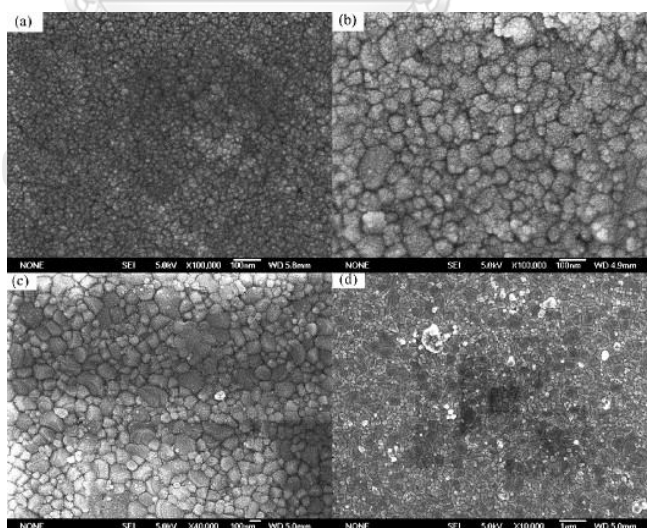


**Fig. 12** SEM micrographs of ScSZ sintered at (a) 800  $^{\circ}\text{C}$  (b) 900  $^{\circ}\text{C}$  (c) 1000  $^{\circ}\text{C}$  (d) 1100  $^{\circ}\text{C}$  for 4 hours [30]

Therefore, to stabilize cubic phase structure as well as maintain high physical properties of electrolyte, substituting 1 mol% of  $\text{Sc}_2\text{O}_3$  for other lanthanum oxides such as  $\text{Gd}_2\text{O}_3$ ,  $\text{CeO}_2$ ,  $\text{Bi}_2\text{O}_3$ , and  $\text{Yb}_2\text{O}_3$  have been studied [31]. There are reported that co-doped samples improve the stability of cubic phase even sintering at high temperature, agreeing well with the phase diagram of  $\text{ZrO}_2$ - $\text{Gd}_2\text{O}_3$  and  $\text{ZrO}_2$ - $\text{Yb}_2\text{O}_3$  that  $\beta$ -phase was not observed in the binary system [32]. The co-doped sample was also reported to exhibit higher conductivity compared to the bare ScSZ electrolyte sample [32]. The trivalent dopant introduces oxygen vacancy in the structure leading the oxygen mobility increase, whereas, the  $\text{Ce}^{4+}$  dopant enhances the cubic symmetry of the oxygen sublattice leading to higher ion conductivity as well. It should be noted that the larger atom dopant can introduce lattice strains and inhibits the motion of oxygen vacancies, lowering in ionic conductivity [32]. Therefore, the  $\text{Yb}^{3+}$  (0.985 Å) co-doped sample achieved the highest conductivity, followed by  $\text{Ce}^{4+}$  (0.97 Å) and  $\text{Gd}^{3+}$ -doped 10ScSZ (1.053 Å), respectively. Even  $\text{Ce}^{4+}$  has a higher ionic radius than  $\text{Yb}^{3+}$  dopant, but  $\text{Ce}^{4+}$  does not enhance ionic conductivity by introducing oxygen vacancies as mention earlier. Therefore, the conductivity of  $\text{Ce}^{4+}$ -doped 10ScSZ sample is in between  $\text{Yb}^{3+}$  and  $\text{Gd}^{3+}$ -doped 10ScSZ.  $\text{Ce}^{4+}$  dopant showed the best result in improving the phase stability even lower conductivity than  $\text{Yb}_2\text{O}_3$ -doped 10ScSZ was shown [33]. However, the rapid degradation problem is observed when compared to YSZ for long term operation.

In case of  $\text{Bi}_3\text{O}_3$ ,  $\text{Bi}_2\text{O}_3$  is normally known to be one of sintering aid to decrease sintering temperature of YSZ [34]. It is therefore of an interesting way to maintain an adequate cubic structure, as well as to gain applicable low sintering temperature for SOEC. There are reported that the additional  $\text{Bi}_2\text{O}_3$  can aid the sintering process of ScSZ electrolyte. In addition, cubic-rhombohedral phase transformation and conductivity of ScSZ were improved with the presence of  $\text{Bi}_2\text{O}_3$  [34, 35]. It should be noted that at least 1 mol% of  $\text{Bi}_2\text{O}_3$  is required to maintain cubic phase. As shown in Fig. 13, the rhombohedral phase peak was not detected in 10ScSZ electrolyte sintered at 1300 °C when doping with  $\text{Bi}_2\text{O}_3$  more than 1 mol% [35].

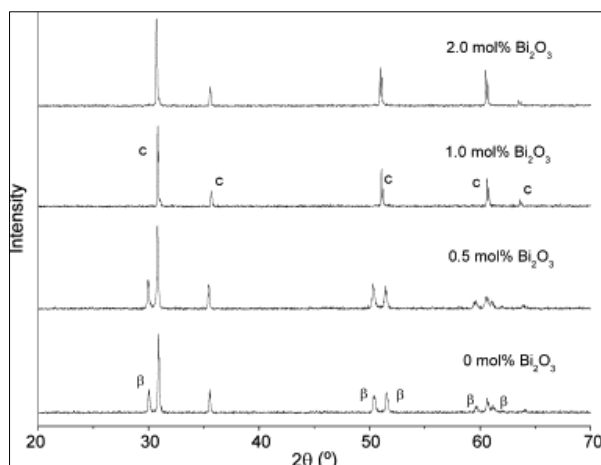


**Fig. 13** XRD patterns of 10ScSZ-doped with different amount of  $\text{Bi}_2\text{O}_3$  sintered at 1300 °C for 2 hours [35]

#### 2.1.2.2 Ceria-based oxide

Ceria-based electrolyte has been reported as a promising intermediate-temperature electrolyte (500-800 °C), providing more benefits in terms of ionic conductivity, compared with YSZ electrolyte. Doping proper divalent and trivalent cation in which has an ionic radius close to  $\text{Ce}^{4+}$  can increase the conductivity of the ceria-based electrolyte, as well as zirconia-based electrolyte.  $\text{Sm}^{3+}$ ,  $\text{Gd}^{3+}$ ,  $\text{La}^{3+}$ ,  $\text{Yb}^{3+}$ ,  $\text{Y}^{3+}$  and  $\text{Ca}^{2+}$  have been investigated as a dopant for ceria-based electrolyte [17]. Table 4 [36] shows the conductivity data of some ceria-based electrolyte prepared by oxalate coprecipitation method.

**Table 4** Ionic conductivity of different ceria-based electrolyte [36]

Material	Conductivity ( $\text{S cm}^{-1}$ )	Temperature (°C)
20GDC	$4.2 \times 10^{-2}$	700
( $\text{Gd}^{3+}$ -doped ceria)	$9.0 \times 10^{-2}$	800
20SDC	$4.1 \times 10^{-2}$	700
( $\text{Sm}^{3+}$ -doped ceria)	$8.8 \times 10^{-2}$	800
20YDC	$3.5 \times 10^{-2}$	700
( $\text{Y}^{3+}$ -doped ceria)	$7.7 \times 10^{-2}$	800

GDC (Gadolinium doped ceria) exhibited the highest ionic conductivity at intermediate operating temperature, higher than the YSZ conventional electrolyte which is about  $10^{-4}$  S  $\text{cm}^{-1}$  at temperature 600 °C. The properties of GDC electrolyte material compared with YSZ electrolyte are listed in Table 5.

**Table 5** Properties of SOEC electrolyte [37]

Properties	YSZ	GDC
TEC ( $10^{-6}$ °C $^{-1}$ )	10.5	11.9
Ionic conductivity (S $\text{cm}^{-1}$ )	0.01 (800 °C)	0.1 (800 °C)
Surface exchange coefficient (cm s $^{-1}$ )	$10^{-18}$ - $10^{-19}$ (700-900 °C)	$10^{-18}$ - $10^{-19}$ (600-700 °C)
Oxygen exchange coefficient (cm $^2$ s $^{-1}$ )	$10^{-15}$ - $10^{-16}$ (700-900 °C)	$10^{-18}$ - $10^{-19}$ (600-700 °C)

It is found that GDC achieves better performance than YSZ electrolyte. In addition, there are reported that the conductivity of GDC increases with increasing dopant concentration. After reaching the maximum, the conductivity of GDC decreases with increasing the amount of dopant. The maximum conductivity of GDC is obtained at approximately 20 mol%, as shown in Fig. 14 [23].

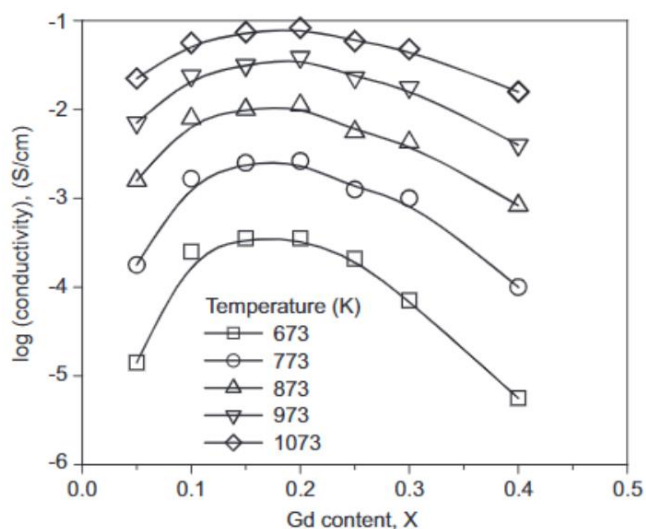


**Fig. 14** Effect of dopant concentration on GDC ionic conductivity [23]

The main problem of ceria-based electrolyte is the partially reduced of  $\text{Ce}^{4+}$  to  $\text{Ce}^{3+}$  under a reducing environment, leading to electronic conduction which causes a partial internal short circuit within electrolyte as well as poor hydrogen evolution in SOEC mode [17]. The high voltage of SOEC condition was reported to increase the maximum tensile stress by seven times, and also decrease the permission of oxygen partial pressure at the electrode-electrolyte interface [38]. In addition, mechanical failure is observed due to lattice expansion from  $\text{Ce}^{4+}$  (0.97 Å) to  $\text{Ce}^{3+}$  (1.143 Å) [39].

Steele [40] reported that 10GDC is more stable to electronic conduction than 20GDC when operating at 500-800 °C. This problem can be resolved by fabrication other types of electrolyte layer, such as YSZ or LSGM, to be the buffer layer prohibiting the reducing environment from ceria [1, 41]. Kim et al. [41] reported that the approximately 1-2 mm of YSZ buffer layer thickness was sufficient to be the electron blockage, nonetheless, the thermal expansion mismatch between two electrolyte layers should be minimized. There are reported that the bi-layered GDC/YSZ electrolytes exhibited the ASR value (area-specific resistance) of  $0.2 \Omega \text{ cm}^{-2}$ , lower in comparison with GDC and YSZ electrolytes operated in the same condition [1].

## 2.2.2 Electrode materials

Electrode material is divided into two parts. The first part is cathode or fuel electrode. The second part is anode or oxygen electrode. Gas transportation inside of electrode and between electrode-electrolyte interface is required. Therefore, suitable porosity and pore size are necessary properties. Moreover, electrode materials should have chemical and physical stability under highly oxidizing and reducing environment, as well as compatible with other components.

### 2.2.2.1 Cathode (Fuel electrode)

As oxygen partial pressure on the cathode side is on the range  $10^{-12}$  to  $10^{-16}$  bar at 1000 °C [42]. Thus, the metallic material of noble metal (such as

platinum) and non-precious metal (such as nickel) is an alternative possible way for the hydrogen electrode [43]. Ni has become a widely used material in SOEC and SOFC due to its high electrochemical reactivity, and lower cost than noble metal [16, 44]. However, Ni mainly conducts electrons during hydrogen reduction reaction leading the reaction take place only at the interface between cathode and electrolyte, which is the triple-phase boundary position (TPB). Furthermore, the pore structure of cathode also might get closed due to the low melting point of Ni. Thus, ion-conducting particles, such as YSZ electrolyte material, are usually mixed with Ni particles to extend the electrochemical reaction zone for the fuel electrode [16]. This type of electrode is also known as cermet electrode [45]. This electrode is synthesized under the concept of combining the properties of two types of material: ceramic and metal. The basic ceramic properties are highly resistant toward heating and chemical reaction, especially oxidation reaction. When ceramic is combined with metals which have high flexibility and good thermal conduction properties, resulting in a good catalytic electrode for high-temperature steam electrolysis. Moreover, the thermal expansion coefficient (TEC) of electrode and electrolyte material are hardly different. Thus, it can also resolve the segregation problem between electrode and electrolyte layers. For Ni-YSZ electrode, TPB is the boundary where Ni, YSZ, and open pores meet to form the transport path of electrons, oxygen ions, and gas as shown in Fig. 15.

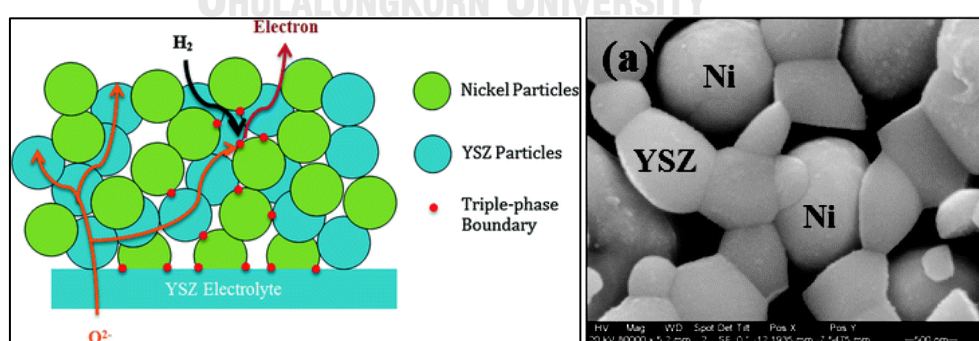


Fig. 15 (Left) Triple-phase boundary and (Right) SEM image of Ni/YSZ electrode [46, 47]

Porous Ni-electrolyte cathode is usually prepared by mixing NiO powder and electrolyte powder, followed by ceramic fabricating method such as dry pressing, tape casting or freeze tape casting. The electrochemical performance of the conventional Ni-YSZ cermet has been investigated by several researchers. Kim et al. [48] studied the IV response under SOEC operation using Ni-YSZ as the cathode. At 850 °C, the current density of 0.3 A cm<sup>-2</sup> of Ni-YSZ/YSZ/LSM-YSZ cathode-supported cell was reported when applied the thermoneutral voltage of 1.3 V at 70% H<sub>2</sub> and 30% H<sub>2</sub>O. It should be noted that the configuration of cell significantly influences cell performance.

Although Ni-based cermet is widely used as a cathode for solid oxide electrolyte cells. However, the Ni-electrolyte electrode instability is still an unsolvable problem that should be aware of. Several authors have reported the degradation of cermet material on SOEC application. Ni particles were oxidized rapidly when exposed to high steam and low hydrogen partial pressure resulting in electrical conductivity loss, electrode performance loss, and delamination between the electrode layer and electrolyte [49]. Recycling of product gas may be the solution to this problem to avoid the re-oxidation of Ni to NiO. Nonetheless, requiring of hydrogen to produce hydrogen could result in incongruousness. Moreover, Ni tends to agglomerate after prolonged operation – resulting in decreasing TPB active sites [50]. For this reason, new materials have been researched for use as fuel electrodes.

Perovskite-type is one of alternative materials for avoiding oxidation reaction of cathode. Due to the mixed ionic and electronic conduction property (MIEC), and the redox-stable property of perovskite, therefore, metal oxide is not required to be an electrons carrier. An additional advantage is that most ceramic oxides have a high melting point, resulting in higher thermal stability during prolonged operation. Perovskite materials, such as strontium ferrite molybdate (SFM) [51], lanthanum-doped strontium vanadate (LSV) [52], and strontium-doped lanthanum manganite partially substituted with chromium (LSCM) [53], have been studied as a fuel electrode. These materials exhibit high activity in both oxidizing and reducing environment without requirement of reducing gas flowing over electrode



[54]. However, perovskite electrode performance for steam electrolysis is still a challenge due to inadequate catalytic property of ceramic material which not comparable to the traditional Ni metal.

#### 2.2.2.1.1 Effect of nickel content

The proper ratio between metal and ceramic components is the key factor to create both continuous electronic and ionic conducting paths. There should have enough metal components to provide sufficient electrocatalytic activity, porosity, and electronic conducting path. While there should have enough ceramic components to provide an ionic conducting path together with a similar thermal expansion to electrolyte. Therefore, the percolation limit of cermet is significant. Pratihari et al. [55] reported that the change from non-metallic to metallic behavior takes place at 20 vol% Ni for the Ni/8YSZ prepared by electroless coating techniques, lower than the value of 30 vol% Ni prepared by other techniques [56]. A similar change around 30 vol% Ni for Ni/10ScSZ cermet also reported, as presented in Fig. 16.

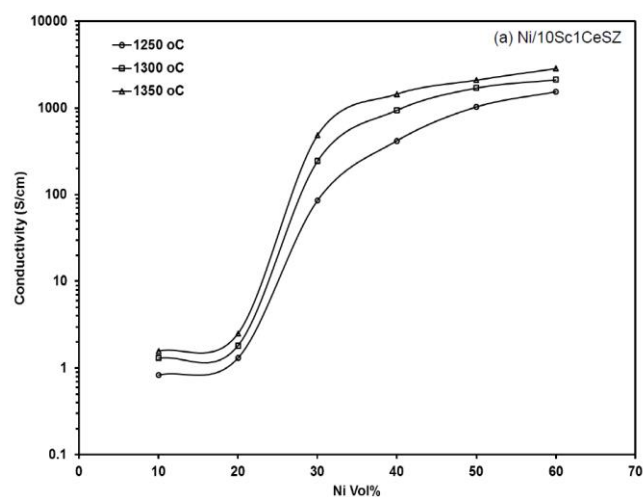


**Fig. 16** Electrical conductivity of Ni/10ScSZ as a function of Ni content and sintering temperature [57]

The electrical conductivity of Ni/10ScSZ film, 30 mm thickness, was measured under 10% H<sub>2</sub> and 90% N<sub>2</sub> at 700 °C. All these plots exhibited a rapid change in electrical conductivity around 30 vol% Ni, changing from ionic conduction to electronic conduction. For this reason, reducing the Ni content below 20-45 vol% normally lost electrical percolation network, leading to a higher resistance [57]. Therefore, the amount of Ni in the cermet should be typically at least 20-30 vol% to achieve the percolation threshold for electronic conductivity.

The porosity of cathode is another important factor associated with the composition of the cermet, which has direct effect on the mass transport of steam to TPB – relating to the increasing gas transport to reactive sites. The proper amount of porosity is required to maintain the mechanical strength and cathode performance. Normally, there are two main factors affecting porosity on cathode: Ni content and sintering temperature. There are reported that the porosity increases as the Ni content increases and continuity of porosity in cathode should have more than 30 vol% to facilitate the mass transport of gas [58]. For Ni/8YSZ cathode, typical porosity about 35 vol% was found for 40 vol% Ni and 60 vol% YSZ (approximately 60 wt% Ni – 40 wt% YSZ), as well as Ni-10ScSZ which achieved higher porosity than 30 vol% at the same Ni and electrolyte content as shown in Fig. 17 [57, 59]. Moreover, it is showed that high sintering temperature provides denser cathode, resulting in strong Ni-Ni contact. Therefore, the denser cathode is expected to have higher electronic conductivity, even porosity is lower [57].

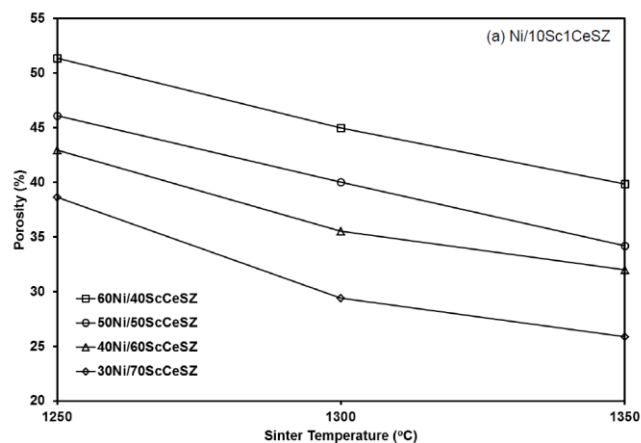


Fig. 17 Porosity variation as a function of sinter temperature of Ni/10Sc1CeSZ [57]

### 2.2.2.1.2 Effect of Pore former

Gas permeability and electrical conductivity of SOEC cathode significantly depend on the cathode microstructure; for example, the amount of porosity, pore shape, and the distribution of pore. Commonly, the partial pressure of steam in SOEC is more than 70%. Moreover, the steam diffusion process is much more difficult than hydrogen. Therefore, the remaining porosity in cathode structure is not adequate for SOEC operation. For this reason, pore former is required for cathode to enhance porosity and improve the steam diffusion process. The porosity of cathode as a function of pore former content was shown in Fig. 18 [58].

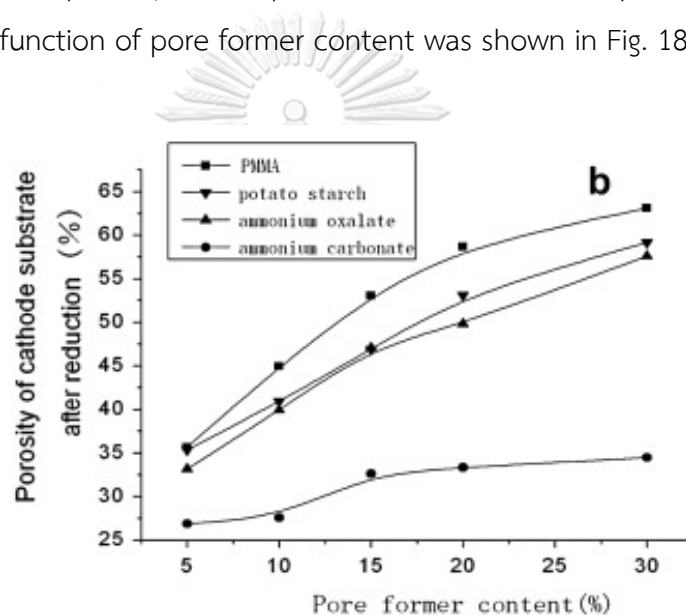


Fig. 18 Porosity of cathode substrate as a function of pore former content [58]

The porosity of cathode increased with the pore former content. The best pore former was the PMMA which porosity increased from 35% to 64% when pore former content increased from 5% to 30%. The second is potato starch which porosity increased from 35% to 59% at the same condition. Nonetheless, there are reported that the electrical conductivity of cathode decreased with increased porosity due to lower continuity of metal in cathode, as shown in Fig. 19.

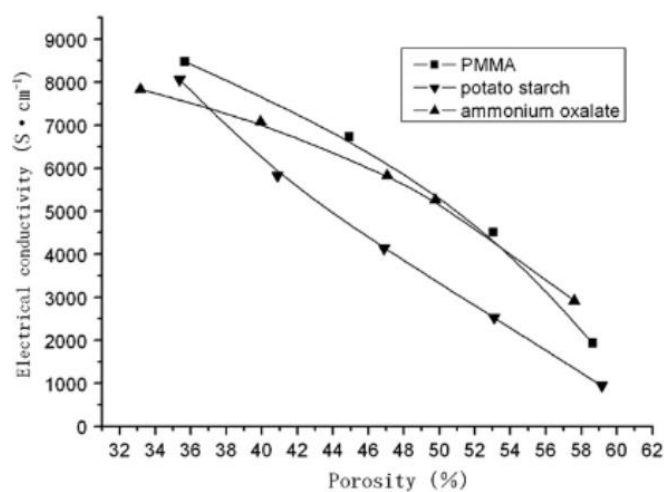


Fig. 19 Electrical conductivity of cathode as a function of porosity [58]

According to the porosity requirement of SOEC was in the range of 30-50%. At 50% porosity, PMMA and ammonium oxalate had conductivity more than 5000 S cm<sup>-1</sup>, while potato starch was more than only 3000 S cm<sup>-1</sup> which could reach the requirement of electrical conductivity. However, the cathode began to collapse, and the strength was also reduced when the pore former content of PMMA and potato starch were more than 10%. Therefore, PMMA and potato starch below 10% are the best amount meeting the requirement of porosity with a value of 45% and 40%, respectively.

#### 2.2.2.2 Anode (Oxygen electrode)

The oxygen electrode has to withstand with high oxidizing environment. Therefore, only two classes of material are feasible as anode for SOEC: noble metals such as platinum and gold; and electronically conducting mixed oxides. Similar to cathode, cost is significant for material consideration. Thus, only of electronically conducting mixed oxides are appropriate material for using as anode in SOEC. In early studies on SOECs, mixed oxides with perovskite structure are the most commonly used as oxygen electrode with an acceptable electrochemical activity such as strontium doped lanthanum manganite (LSM) [16, 60]. 20 mol% strontium doped lanthanum manganite perovskites (LSM) is an electronic conductor material.

Therefore, the electrochemical reaction sites (TPB) mainly exist at the interfaces between anode and electrolyte [61]. However, oxygen enables to migrate through oxygen vacancy in oxygen lattice created by the substitution of  $\text{La}^{3+}$  by  $\text{Sr}^{2+}$  and partial reduction of  $\text{Mn}^{4+}$  and  $\text{Mn}^{3+}$  [62, 63]. Thus, the relatively low ionic conductivity and slow oxygen reduction kinetics are the main problem for this material due to the absence of oxygen vacancy continuity. Bo et al. [64] reported that an area specific resistance (ASR) data of LSM electrode measured from Ni-YSZ/YSZ/LSM cell was only  $3.7 \Omega \text{ cm}^{-2}$  at  $950 \text{ }^\circ\text{C}$  under SOEC operation, even high-temperature electrolysis was used.

Due to similarity of thermal expansion coefficient between LSM and YSZ ( $10.6\text{-}11 \times 10^{-6} \text{ K}^{-1}$ ). Enhancing of ionic phases, such as YSZ, above percolation limit is required for increasing TPB reaction sites [65, 66]. However, it was found that high oxygen partial pressures took place between the interfaces of LSM-YSZ electrode and YSZ electrolyte during steam electrolysis, leading to the delamination of oxygen electrodes which is the major degradation issue in SOEC. In addition, there are reported that the diffusion of  $\text{MnO}_x$  from LSM into YSZ was found, leading to the reaction between free  $\text{La}_2\text{O}_3$  or  $\text{SrO}$  with YSZ which can form the low conducting phase of  $\text{La}_2\text{Zr}_2\text{O}_7$  or  $\text{SrZrO}_3$ . Over-doping of  $\text{MnO}_x$  in the LSM can solve this problem [67]. The other composite electrodes of YSZ, such as  $\text{La}_{0.8}\text{Sr}_{0.2}\text{FeO}_3$  (LSF) and  $\text{La}_{0.8}\text{Sr}_{0.2}\text{CoO}_3$  (LSC), are continuously being proposed as SOEC oxygen electrodes. There are reported that LSC-YSZ exhibited stable decrease in performance within 100 hours, due to occurring of the reaction between LSC and YSZ. For comparison, LSF-YSZ exhibited higher short-term stability than LSC-YSZ at temperature below  $800 \text{ }^\circ\text{C}$ , and also exhibited higher catalytic activity to oxygen evolution than LSM-YSZ.

Recently, mixed ion- and electron-conducting (MIEC) electrodes have also been investigated for SOEC, such as lanthanum strontium ferrite (LSF) [68], and lanthanum strontium cobaltite ferrite (LSCF), due to their high electrical and ionic conductivity. LSCF is an interesting material because of being an oxygen-deficient perovskite, resulting in high migration of oxygen ions through the oxygen vacancies [69]. This material exhibited higher performance than LSM-YSZ and LSF in both SOFC and SOEC modes with higher surface exchange coefficient and diffusivity of oxygen;

and lower polarization resistance [70]. Performance stability of LSCF and LSF was also improved when operating at SOEC mode. However, the delamination between electrolyte and anode layers was observed in MIEC electrodes because of high thermal expansion coefficient of MIEC material ( $12.2-20.5 \times 10^{-6} \text{ }^\circ\text{C}^{-1}$ ), corroborating to degradation in cell performance [71]. In addition, there are reported that MIEC, especially LSCF, performed less well for oxygen evolution when compared to oxygen reduction. This behavior corresponded with an expected decrease in oxygen vacancy concentration when operating mode change from SOFC to SOEC. The properties of each type anode materials are listed in Table 6.

**Table 6** Properties of SOEC anode [37]

Properties	LSM	LSM-YSZ	LSCF
TEC ( $10^{-6} \text{ }^\circ\text{C}^{-1}$ )	12	11.5	14-17
Electronic conductivity ( $\text{S cm}^{-1}$ )	190 (900 $^\circ\text{C}$ )	-	275 (700 $^\circ\text{C}$ )
Ionic conductivity ( $\text{S cm}^{-1}$ )	$10^{-6}-10^{-7}$ (900-1000 $^\circ\text{C}$ )	$10^{-3}$ (900 $^\circ\text{C}$ )	0.01 (700 $^\circ\text{C}$ )
Surface exchange coefficient ( $\text{cm s}^{-1}$ )	$10^{-8}-10^{-9}$ (700-900 $^\circ\text{C}$ )	$10^{-6}-10^{-7}$ (800-900 $^\circ\text{C}$ )	$10^{-6}-10^{-7}$ (650-750 $^\circ\text{C}$ )
Oxygen exchange coefficient ( $\text{cm}^2 \text{ s}^{-1}$ )	$10^{-13}-10^{-16}$ (700-900 $^\circ\text{C}$ )	$10^{-9}$ (800-900 $^\circ\text{C}$ )	$10^{-7}-10^{-12}$ (750-850 $^\circ\text{C}$ )

Perovskite-type  $\text{Ba}_{0.5}\text{Sr}_{0.5}\text{Co}_{0.8}\text{Fe}_{0.2}\text{O}_{3-\delta}$  (BSCF) was also proposed as an oxygen electrode for both SOEC and SOFC. Bo et al. [72] reported that an area specific resistance (ASR) data of the BSCF/YSZ electrode as low as  $0.27 \text{ } \Omega \text{ cm}^{-2}$  at 800  $^\circ\text{C}$  which lower than commonly used oxygen electrode as LSM and other electrode materials, such as LSCF, in both of SOEC and SOFC modes. It can indicate that BSCF material has high oxygen permeation fluxes and exceptional catalytic properties. BSCF was also studied under SOEC operation by Kim-Lohsoontorn et al. [73]. They reported that even electrochemical performance of BSCF cell was significantly high,

however, performance decay under electrolysis mode was observed (initial potential of 1.17 V and degradation rate of  $0.02 \text{ V h}^{-1}$ ) when compared to a relatively stable LSM-YSZ cell performance. ASR of BSCF in comparison with other oxygen electrodes was shown in Fig. 20.

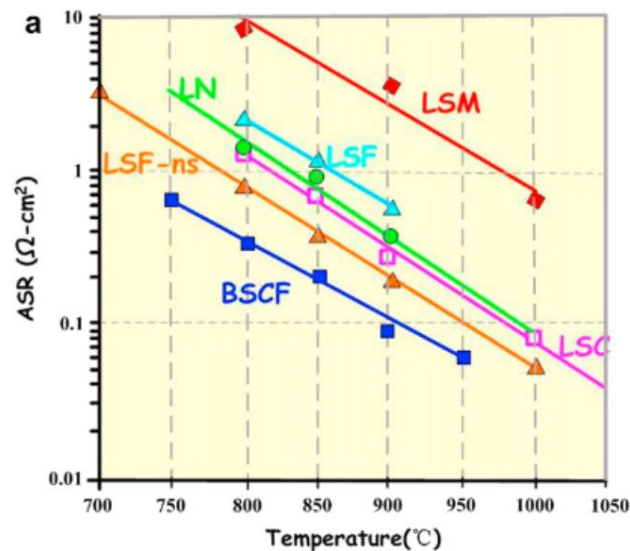


Fig. 20 ASR of BSCF in comparison with other oxygen electrode materials [72]

### 2.2.3 Operating conditions

The efficient electrolysis process needs to be done in suitable conditions; for example, operating temperature, the ratio of gas supplied to the fuel electrode, and applied voltage to achieve high-performance production resulting in lower operating costs. For this reason, there are many researches discuss the optimum conditions for the electrolysis process.

In case of temperature variation, the electrochemical reaction process at different operating temperatures has a significant effect on the current density. In which when the reaction temperature is increased, electrolyte cells can generate more electricity represented higher hydrogen production, as shown in Fig. 21.

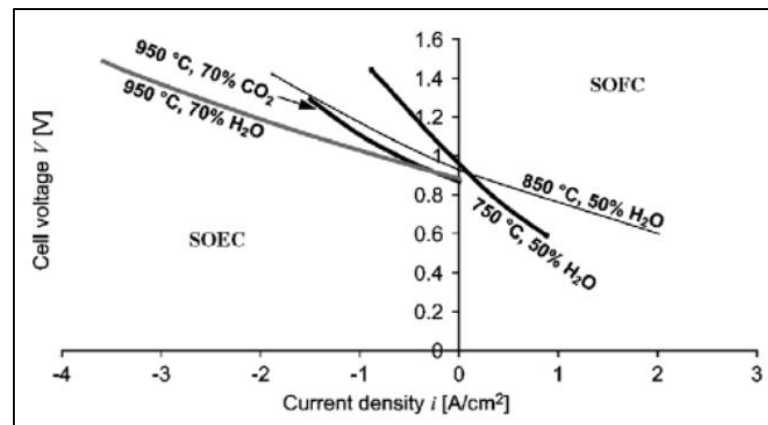


Fig. 21 IV curve of Ni-YSZ at different temperature and inlet gas compositions [10]

Fig. 21 presented IV curves of Ni-YSZ/YSZ/LSM-YSZ operating under both of SOEC and SOFC modes at different temperature and inlet gas compositions. Comparing SOEC and SOFC mode operation, the electrolysis mode resistance was higher than fuel cell mode noticed by higher slope in SOEC mode from IV curve. This can indicate that large molecule of  $\text{H}_2\text{O}$  precursor in SOEC mode leading the higher gas diffusion resistance of electrolysis mode greater than fuel cell mode. However, the gas diffusion resistance does not much depend on the temperature compared to another type of resistance such as oxide ion transfer [10]. Therefore, a larger portion of gas diffusion in SOEC when compare to SOFC mode can lead to less dependent on temperature in SOEC, noticed by the lower relative change of resistance of SOEC mode between 750 and 850 °C.

Even more amount of large molecule of  $\text{H}_2\text{O}$  precursor in SOEC mode provides higher resistant compared with SOFC mode, however, SOEC operation was limited by gas diffusion at the  $\text{H}_2$  electrode [74]. Significantly higher current can be reached with increasing humidity at all given cell voltage as shown in Fig. 22. The large difference of resistance was clearly seen between 50 and 70 vol% AH of humidities, indicated the limitation of SOEC.



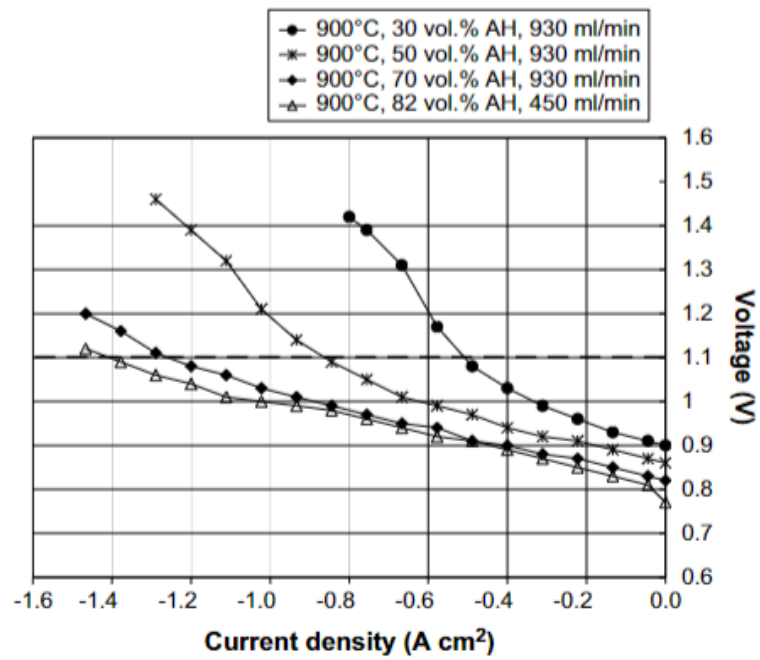


Fig. 22 IV curves in SOEC mode as a function of gas feed to electrode at 900 °C [74]

Similarly, the hydrogen production rate also depended on applied voltage, as presented in Fig. 23.

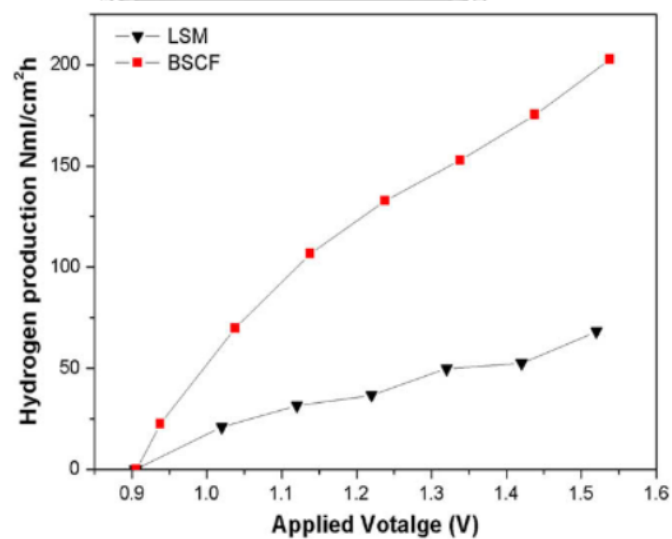


Fig. 23 Hydrogen production rate of BSCF and LSM as a function of voltages [72]

Fig. 23 showed the hydrogen production rate of SOEC consisting of Ni-YSZ/YSZ/BSCF and Ni-YSZ/YSZ/LSM at various electrolysis voltage under the same current density. It can be seen that the hydrogen production rate of both cells increased with applied voltage. High hydrogen production rate with low applied voltage can achieve by high cell performance usage, thus, the materials used as electrodes and electrolytes also affect the hydrogen production.



## CHAPTER III

### EXPERIMENTAL

In this research, scandium, cerium, and gadolinium doped zirconia electrolyte ( $\text{Sc}_{0.1}\text{Ce}_{0.005}\text{Gd}_{0.005}\text{Zr}_{0.89}\text{O}_2$ , SCGZ) for SOEC was studied, comparing with 8 mol% yttria-stabilized zirconia ( $\text{Y}_{0.08}\text{Zr}_{0.92}\text{O}_2$ , YSZ) and gadolinium doped ceria ( $\text{Gd}_{0.1}\text{Ce}_{0.9}\text{O}_{1.9}$ , GDC) electrolyte to optimize both high oxygen conductivity from ceria and chemical stability from zirconia-based material. Electrolyte-supported and cathode-supported cells were fabricated in order to determine performances of each electrolyte toward the hydrogen production from steam, together with the characterization of cells before and after electrolysis testing. In addition, bismuth oxide ( $\text{Bi}_2\text{O}_3$ )-doped in SCGZ (Bi10SCGZ) electrolyte was also studied through the electrolyte-supported cell. Phase stabilization, including electrolyte performance and properties, was carried out to compare with bare SCGZ.

Therefore, the experiment was divided into four main parts: electrolyte-supported cell fabrication; cathode-supported cell fabrication; electrochemical performance measurement; and, electrolyte powder characterization.

### 3.1 Chemicals and equipment

#### 3.1.1 Chemicals

- 3.1.1.1 Scandium, cerium and gadolinium doped zirconia, SCGZ (kceracell)
- 3.1.1.2 8 mol% Yttria-stabilized zirconia, YSZ (kceracell)
- 3.1.1.3 Gadolinium doped ceria, GDC (kceracell)
- 3.1.1.4 Barium strontium cobalt ferrite, BSCF5582 (Kceracell, Korea)
- 3.1.1.5 Bismuth oxide,  $\text{Bi}_2\text{O}_3$  (Sigma Aldrich, USA)
- 3.1.1.6  $\alpha$ -terpineol (Fuelcellmaterials, USA)
- 3.1.1.7 Polyvinylpyrrolidone, PVP (Mw 10000, Sigma Aldrich)

- 3.1.1.8 Polyvinyl butyral resin, Butvar 98 (Chemcruz, USA)
- 3.1.1.9 Polyethylene glycol, PEG400 (Merck KGaA, Germany)
- 3.1.1.10 Butyraldehyde ( $\geq 96.0\%$ , Sigma Aldrich)
- 3.1.1.11 Xylenes (98.5%, Sigma Aldrich)
- 3.1.1.12 Nickel (II) Oxide, NiO (99.8%, Sigma Aldrich)
- 3.1.1.13 Corn-starch powder
- 3.1.1.14 Ethanol (Absolute, Sigma Aldrich)
- 3.1.1.15 Hydrogen (High purity, TIG, Thailand)
- 3.1.1.16 Nitrogen (High purity, TIG, Thailand)
- 3.1.1.17 Distilled water
- 3.1.1.18 Platinum (Pt) conductive paste (Nexceris, 70 wt% Pt loading)
- 3.1.1.19 Gas sealant (Ultra-Temp 552, Aramco, USA)

### 3.1.2 Tool and equipment

- 3.1.2.1 Spoon
- 3.1.2.2 Beaker 50 ml
- 3.1.2.3 Magnetic stirrer
- 3.1.2.4 Weighing paper
- 3.1.2.5 Hydraulic pressing pressure 30 tons
- 3.1.2.6 Mold
- 3.1.2.7 Oven, max temperature = 250 °C
- 3.1.2.8 Furnace, max temperature = 1300 °C
- 3.1.2.9 Furnace, max temperature = 1500 °C
- 3.1.2.10 Hot plate
- 3.1.2.11 Cylinder 25 ml
- 3.1.2.12 Stainless Steel Lab Spatula
- 3.1.2.13 Zirconia balls (5 mm and 10 mm diameter)
- 3.1.2.14 Two-row mills (SLheater, max mill speed = 500 rpm)
- 3.1.2.15 HPLC liquid pump (Teledyne SSI, USA)
- 3.1.2.16 Potential stat (Metrohm Autolab, Netherlands)
- 3.1.2.17 Brunauer-Emmett-Teller, BET (ASAP2020, Micromeritics)

3.1.2.18 Scanning electron microscope (SEM, JEOL model S-3400)

3.1.2.19 X-Ray Diffractometer (XRD, BRUKER model D8 advance using  $K\alpha$  radiation of Cu)

3.1.2.20 Thermogravimetric analyses (TGA, TA Instruments SDT Q600)

## 3.2 Experimental

### 3.2.1 Electrolyte-supported cells fabrication

The electrolyte-supported SOECs having different electrolyte materials were fabricated with Pt electrodes (Pt/electrolyte/Pt). Three grams of electrolyte powders were pressed into a pellet at 1.7 MPa for 30 seconds, followed by sintering at 1300, 1450, and 1450 °C for 4 hours for GDC, YSZ, and SCGZ samples, respectively. For the GDC electrolyte, bi-layered GDC/YSZ was fabricated. The YSZ buffer layer was used to prevent the reduction of GDC single layer leading to electron conduction across the electrolyte [1-3]. The GDC pellet was two times dip-coated by YSZ slurry which prepared by mixing of 20 wt% of YSZ powder, 76.4 wt% of xylene and butyraldehyde as solvent, 1 wt% of PVP as dispersant, 0.6 wt% of butvar 98 as binder, and 2 wt% for PEG as plasticizer under temperature 60 °C, followed by fired at 1450 °C for 4 hours.

In case of  $\text{Bi}_2\text{O}_3$ -doped SCGZ electrolyte,  $\text{Bi}_2\text{O}_3$  powder was sintered at 600 °C for 4 hours with a constant heating rate of 5 °C per minute and added into the SCGZ electrolyte powder. The amounts of  $\text{Bi}_2\text{O}_3$  was varied from 0-2 mol%. The  $\text{Bi}_2\text{O}_3$ -doped SCGZ is denoted as 1Bi10SCGZ and 2Bi10SCGZ for 1 and 2 mol%  $\text{Bi}_2\text{O}_3$  doping, respectively. The mixture of  $\text{Bi}_2\text{O}_3$  and SCGZ powder was wet-milled with the rotating speed of 250 rpm for 24 hours using ethanol as a medium, and dried overnight at 105 °C. Three grams of the dried electrolyte powder was pressed into a pellet at 1.7 MPa for 30 seconds and then sintered at varied temperatures from 1150 to 1450 °C for 4 hours to produce an electrolyte pellet.

Relative density of the fabricated electrolyte was estimated by following the calculation method referred in appendix A. The sintered electrolyte

was then coated by platinum (Pt) conductive paste using doctor blade technique, followed by cured at 900 °C for 30 minutes. An electrode active area of 0.502 cm<sup>2</sup> with a thickness of ~30 μm was achieved for both electrodes. The electrolyte-supported cell preparation step was shown in Fig. 24-26.

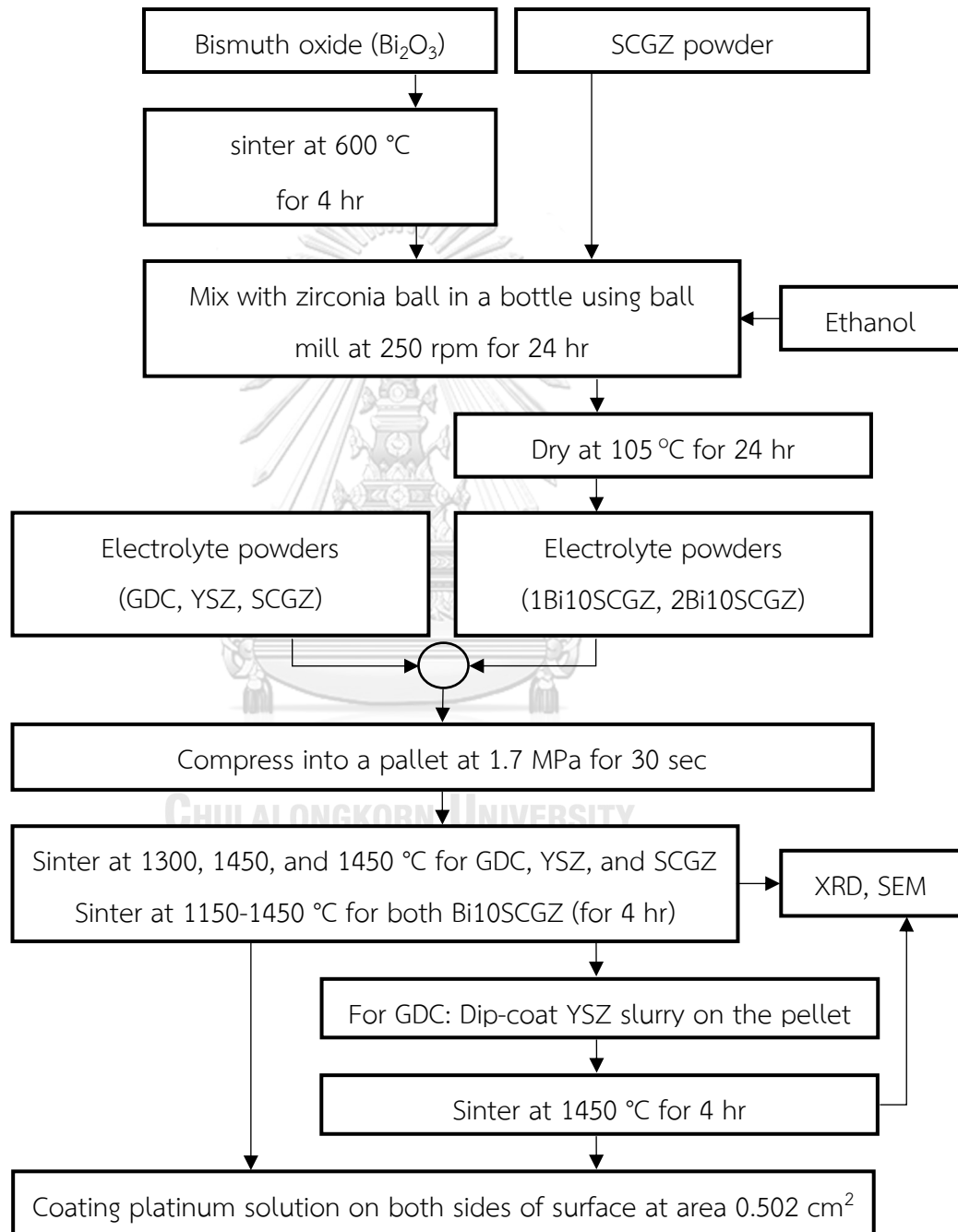
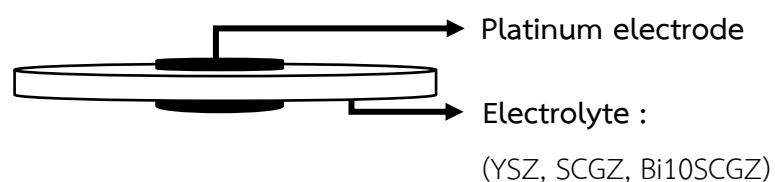
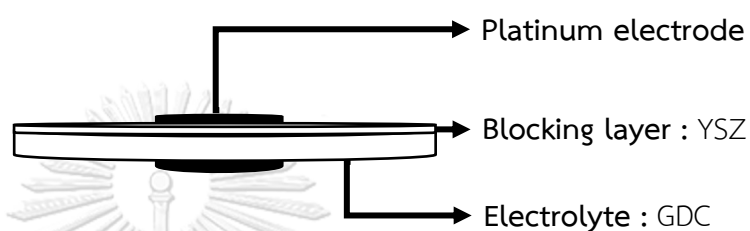


Fig. 24 Electrolyte-supported cells fabrication



**Fig. 25** Electrolyte-supported cells (cross-sectional view)



**Fig. 26** Electrolyte-supported cells (Pt/YSZ/GDC/Pt cross-sectional view)

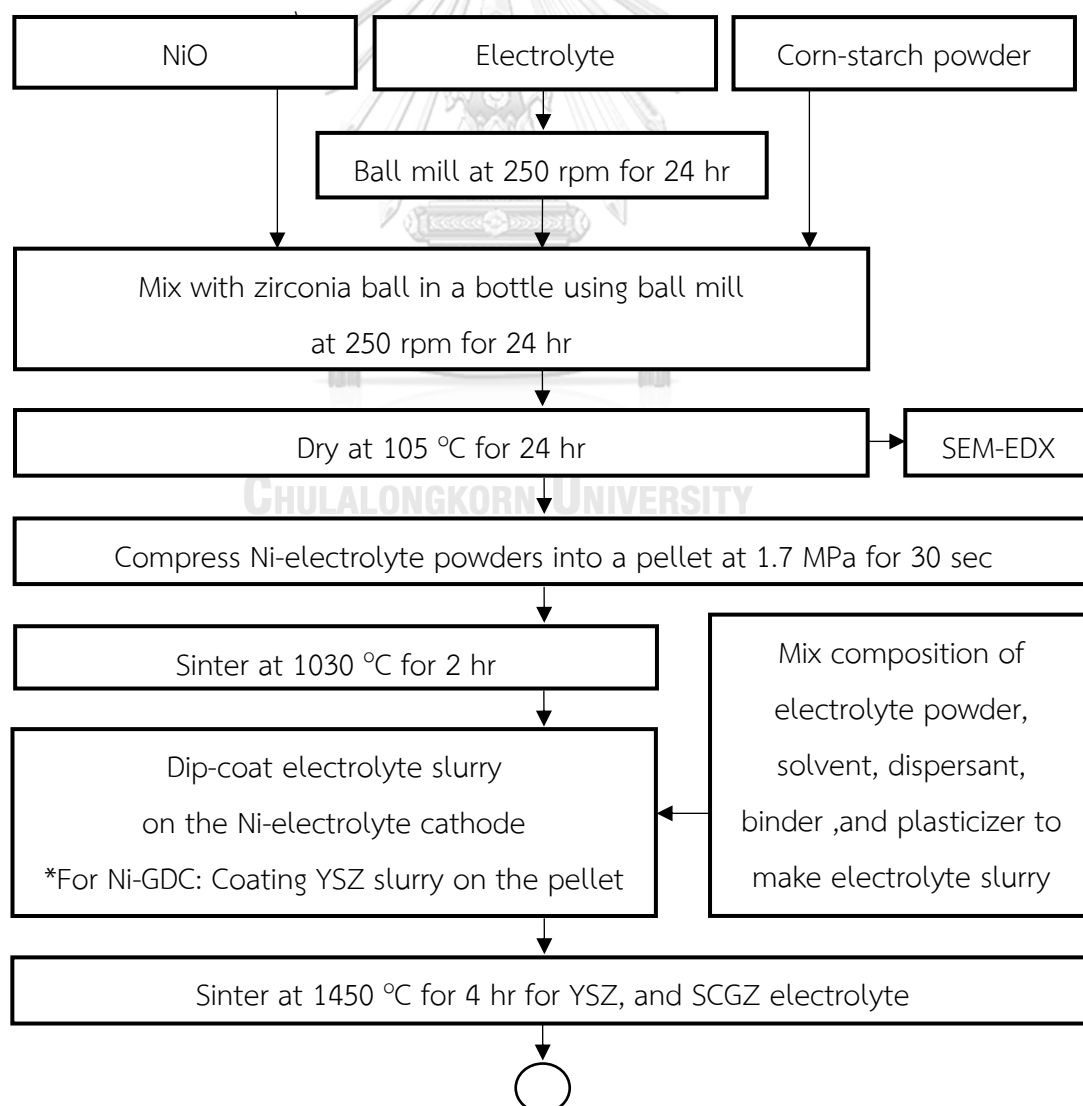
### 3.2.2 Cathode-supported cells fabrication

NiO-electrolyte cathode powder was prepared by wet-mixing NiO with electrolyte powder and corn-starch powder with a weight ratio of 66:34:10 for 24 hours. Before mixing, electrolyte powder size was reduced by ball mill for 24 hours with using proper amounts of zirconia balls (5 mm and 10 mm diameters). Ethanol was used as a medium to make a uniform mixing of cathode powder, and corn-starch powder was used to create sufficient porosity for the structure. Then, the mixed powder was dried to remove ethanol solvent at 105 °C for 24 hours. Three grams of the cathode powder was pressed into a pellet at 1.7 MPa for 30 seconds and sintered at 1030 °C for 2 hours to create both continuous electronic from Ni particle and ionic conducting paths from electrolyte particle.

The electrolyte slurry was prepared by mixing with compositions of 20 wt% of electrolyte powder, 76.4 wt% of xylene and butyraldehyde as solvent, 1 wt% of PVP as dispersant, 0.6 wt% of butvar 98 as binder, and 2 wt% for PEG as plasticizer under temperature at 60 °C. The NiO-electrolyte cathode was two-times dip-coated by electrolyte slurry to deposit electrolyte film with the thickness of ~20 μm,

followed by sintering at 1450 °C for 4 hours for YSZ and SCGZ samples. In case of Ni-GDC cathode, bi-layered GDC/YSZ was fabricated as mention earlier in electrolyte-supported cells fabrication. Therefore, Ni-GDC pellet was two times dip-coated by YSZ slurry first and then two times dip-coated by GDC slurry, followed by sintering at 1450 °C and 1350 °C for 4 hours, respectively.

The oxygen electrode ink was prepared. The  $\text{Ba}_{0.5}\text{Sr}_{0.5}\text{Co}_{0.8}\text{Fe}_{0.2}\text{O}_3$  (BSCF) powder was blended with  $\alpha$ -terpineol using 50:50 weight ratio to prepare BSCF electrode ink. The BSCF ink was then deposited on the as-prepared cells using doctor blade technique having the electrode active area of  $0.502 \text{ cm}^2$  and the thickness of  $\sim 30 \mu\text{m}$ . After that, the cell was then fired at 900 °C for 30 minutes. Cathode-supported cells preparation step were shown in Fig. 27-29.





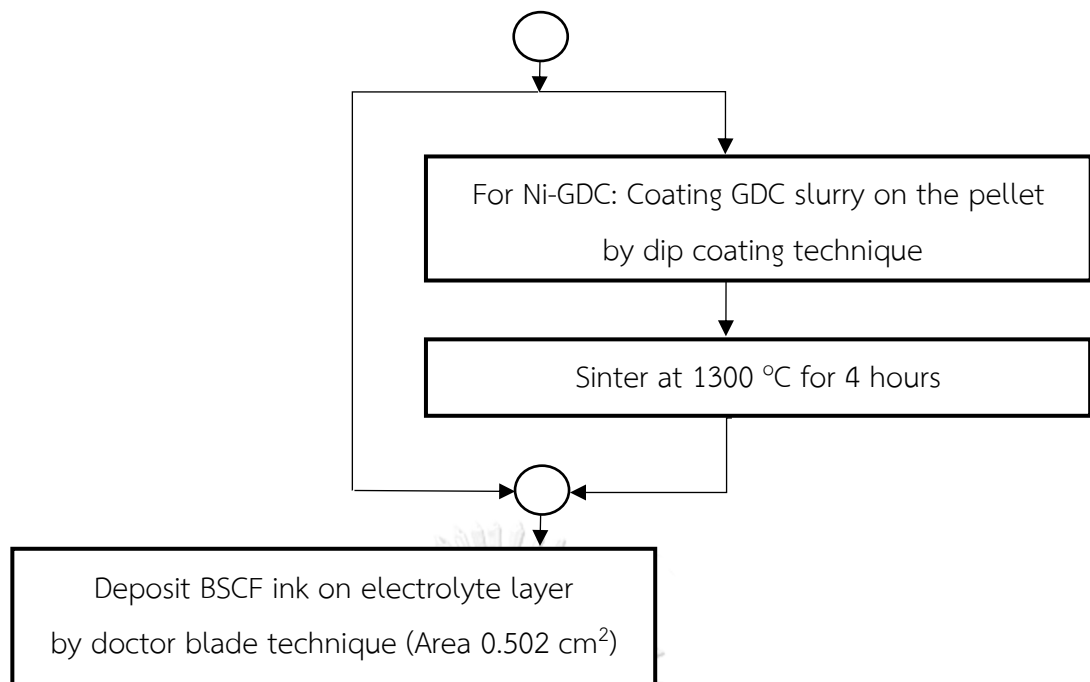


Fig. 27 Cathode-supported cells fabrication

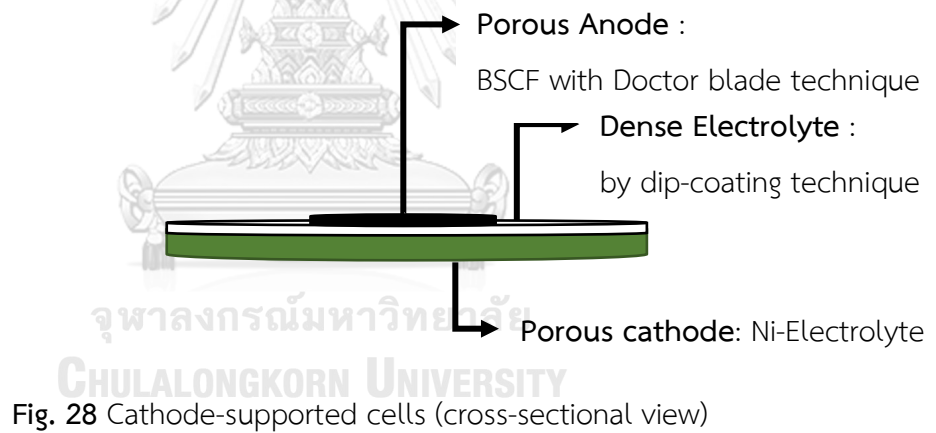


Fig. 28 Cathode-supported cells (cross-sectional view)

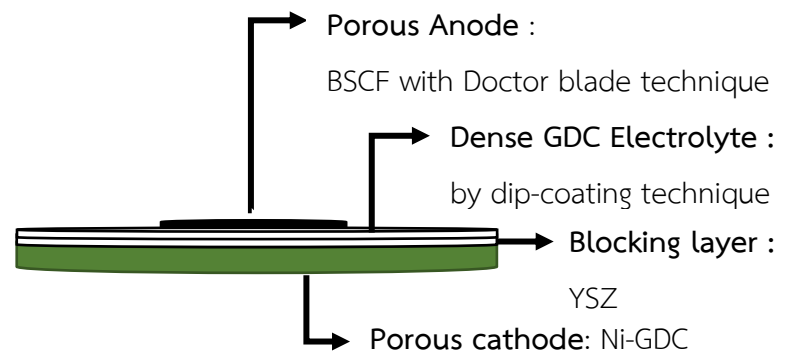


Fig. 29 Cathode-supported cells (Ni-GDC/YSZ/GDC/BSCF cross-sectional view)

### 3.2.3 Electrochemical performance measurement

The electrochemical performance measurement was carried out using potential stat. Platinum wire was attached to the cell for an electrical connection and was then coated by platinum paste again to increase the connection between wire and pellet, as shown in Fig. 30. The fabricated cell attached platinum mesh and wire was placed on a cell holder in furnace under compression to provide well electrical connection, and then sealed using glass sealant to prohibit the recombination of the exposed gas from each electrode. The operating temperature was controlled between 600-900 °C with the feed containing steam (325 ml min<sup>-1</sup> total flow rate), H<sub>2</sub> and N<sub>2</sub> at cathode chamber. The anode chamber was left in stagnant air. Steam was generated by supplying deionized water using HPLC liquid pump through a heated-tube, as presented in Fig. 31.



Fig. 30 platinum wire attachment for an electrical connection

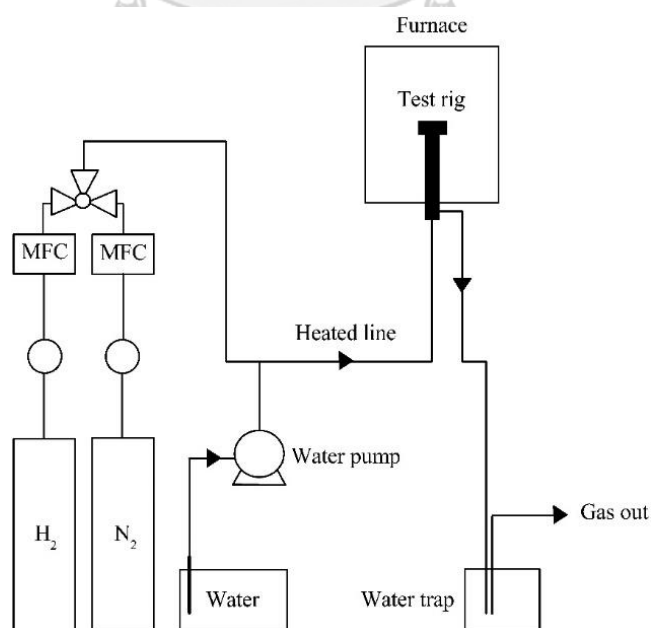


Fig. 31 Schematic drawing of the test system

The current/voltage (I/V) curves were generated using linear sweep current techniques by controlling voltage between 0.5 V and 1.8 V with a scan rate of  $0.1 \text{ Vs}^{-1}$ . The electrochemical impedance spectroscopy (EIS) were measured at OCV, 0.6 V and 1.1 V, by varying the frequency range from 0.1 MHz to 0.1 Hz with a sinusoidal signal amplitude of  $0.01 \text{ V}_{\text{rms}}$ . The ion conductivity as a function of temperature (600-800 °C), and the activation energy of conduction of electrolyte-supported cells were calculated from generated I/V curve using Arrhenius and activation energy of conduction equation referred in appendix C. It should be noted that the activation energy of conduction in this study was calculated from I/V curves at SOEC's operating condition. The slope of the I/V curve is total resistance which included electrode resistance. However, in electrolyte-supported cell Pt was applied as both electrodes (Pt/Electrolyte/Pt) and was expected to provide rather low resistance at operating conditions.

### 3.2.4 Characterization

The relative density of electrolyte pellet was calculated using Eq. (8). Volume shrinkage and linear shrinkage were also taken from direct measurements of the electrolyte pellet dimensions before and after the sintering [75].

$$\text{Relative density} = (\text{Actual density}/\text{Theoretical density}) \times 100 \quad (8)$$

X-ray diffraction pattern (XRD, Bruker D8 Advance powder X-ray diffractometer with  $\text{CuK}\alpha$  source) was used to identify phase in the electrolyte samples before and after electrochemical testing with  $2\theta$  scanned between 20-80 degree. Lattice parameters were reported and used for theoretical density calculation. The specific surface area of the electrolyte sample powders was determined using Brunauer-Emmett-Teller (BET, Micromeritics ASAP2020). The microstructure images of the fabricated cell before and after SOEC operation were taken using scanning electron microscope (SEM, JEOL model S-3400). Average grain size and grain size distributions were investigated and calculated by the SEM micrographs analyzing through the software ImageJ [76, 77]. The EDX-mapping was

used to investigate element distribution in sample. Thermogravimetric analysis (TGA, TA Instruments SDT Q600) was used to measure weight change in Ni-electrolyte cathode powder at 800 °C under 21% oxygen in ambient air, indicating the degree of oxidation of the cathode. The degree of oxidation of the cermet (DoO) was calculated using Eq. (9).

$$\text{DoO}(t) = \frac{M(t) - M_{\text{Ni-electrolyte}}}{M_{\text{NiO-electrolyte}} - M_{\text{Ni-electrolyte}}} \quad (9)$$

When  $M(t)$  is the mass at the oxidation time;  $M_{\text{Ni-electrolyte}}$  is the initial mass of sample, and  $M_{\text{NiO-electrolyte}}$  represents the mass of completed oxidation sample. The TGA/differential scanning calorimeter (DSC) of the electrolyte powders was also reported. The weight change in electrolytes powder between room temperature to 1000°C was also measured by thermogravimetric analysis/ differential scanning calorimeter (TGA/DSC, TA Instruments SDT Q600).

## CHAPTER IV

### RESULTS AND DISCUSSION

Scandium, cerium and gadolinium doped zirconia ( $\text{Sc}_{0.1}\text{Ce}_{0.005}\text{Gd}_{0.005}\text{Zr}_{0.89}\text{O}_2$ , SCGZ) electrolyte for solid oxide electrolysis cell was studied, comparing with 8 mol% yttria-stabilized zirconia ( $\text{Y}_{0.08}\text{Zr}_{0.92}\text{O}_2$ , YSZ) and gadolinium doped ceria ( $\text{Gd}_{0.1}\text{Ce}_{0.9}\text{O}_{1.9}$ , GDC) electrolyte. Electrolyte-supported cells (Pt/electrolyte/Pt) were fabricated to determine the electrolyte performance in terms of activation energy of conduction. In addition, cathode-supported cells of Ni-electrolyte/electrolyte/BSCF ( $\text{Ba}_{0.5}\text{Sr}_{0.5}\text{Co}_{0.8}\text{Fe}_{0.2}\text{O}_3$ ) were also fabricated to assess the electrochemical performance of the cells over a range of steam partial pressures and temperatures as well as the cell durability. Phase and microstructure of cathode-supported cells before and after cell durability test, as well as the oxidation tolerance, were compared as well.

#### 4.1 Phase and microstructure analysis of electrolyte

The BET surface area of the GDC, YSZ and SCGZ powders are 13.5, 11.27 and 14.23  $\text{m}^2 \text{g}^{-1}$ , respectively. The SCGZ starting powder exhibited the highest surface area, indicating the finer particles of the SCGZ, which can help achieving densification of the electrolyte pellet after sintering. It should be noted that fine and uniform particle size can be controlled using sonochemical approach for starting powder synthesis [78-81]. To study the crystalline phases of SCGZ powder and sintered SCGZ electrolyte pellet, The XRD patterns was shown in Figs. 32 and 33, respectively.

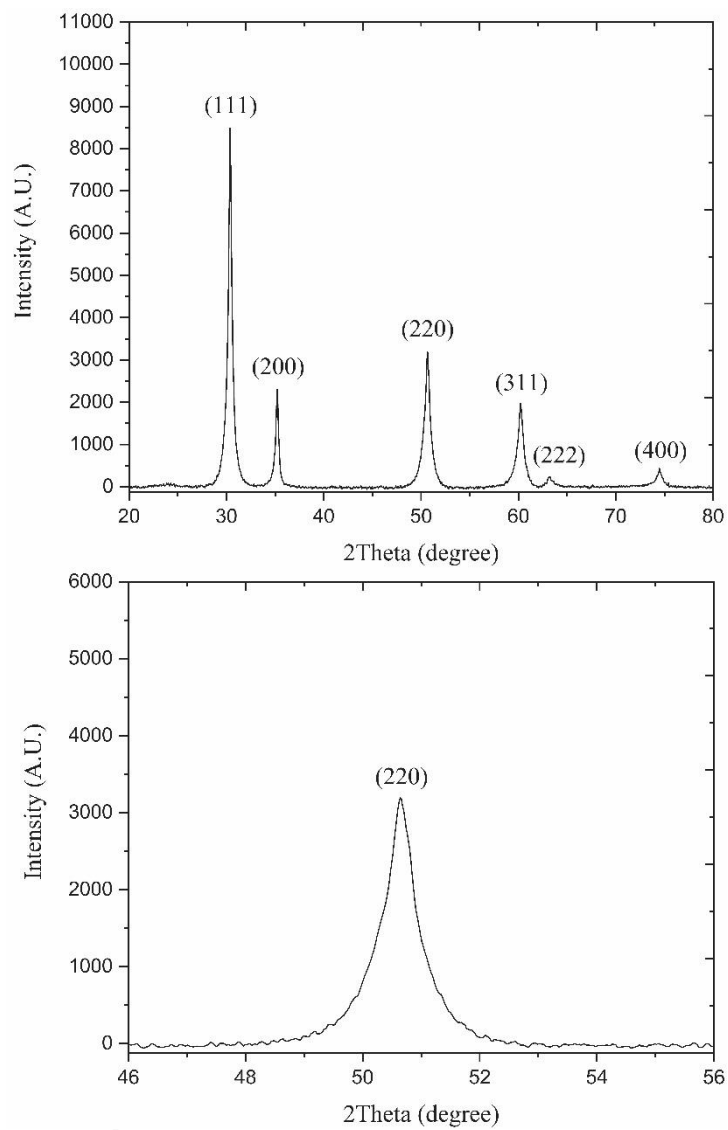
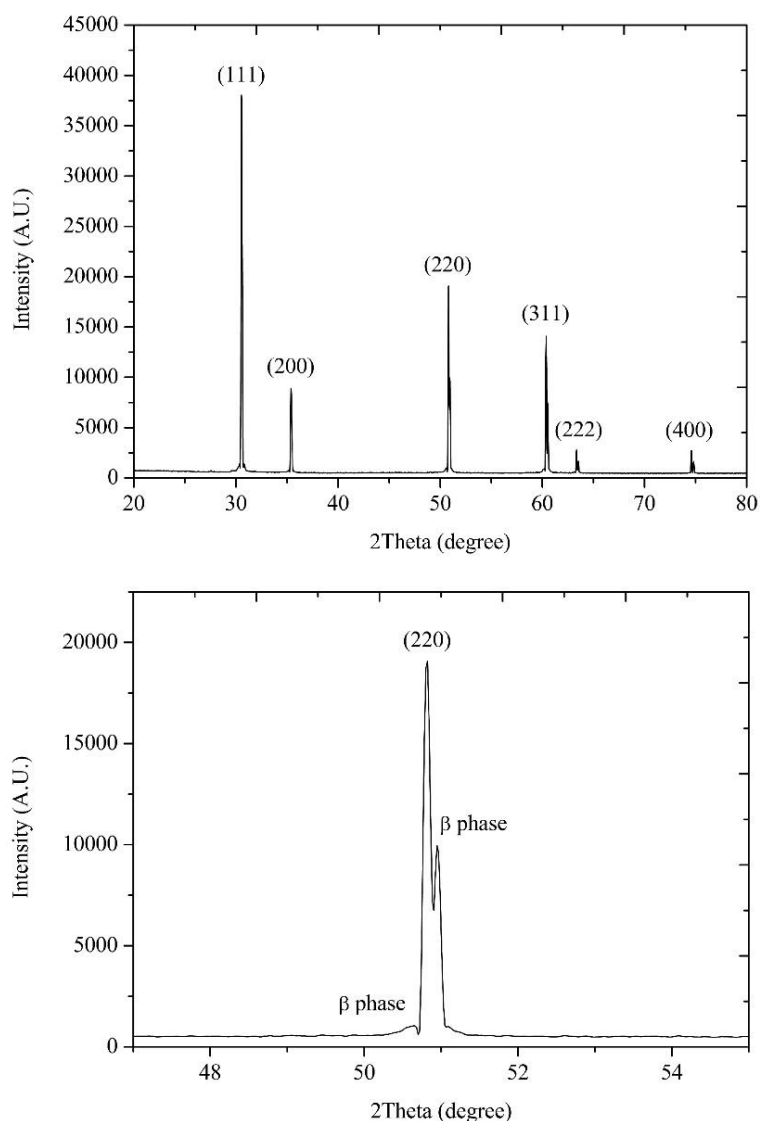


Fig. 32 X-ray diffraction pattern: (top) SCGZ electrolyte powder (bottom) magnified peak over  $2\theta$  ranging from  $46^\circ$  to  $56^\circ$



**Fig. 33** X-ray diffraction pattern: (top) sintered SCGZ electrolyte (bottom) magnified peak over  $2\theta$  ranging from  $46^\circ$  to  $56^\circ$

No impurity or secondary phase was detected in fresh SCGZ powder (Fig. 32). In SCGZ pellet (after electrolyte fabrication), a rhombohedral  $\beta$ -phase ( $\text{Sc}_2\text{ZrO}_{17}$ , JCPDS No. 89-5486), which is a low-conductivity phase, existed together with the main cubic phase (JCPDS No. 89-5485). It was reported that large amount of  $\text{Sc}_2\text{ZrO}_{17}$   $\beta$  phase in ScSZ (Scandia Stabilized Zirconia) can lead to degradation in SOFC performance [27, 82-85]. It was also reported that weak intensity of this  $\beta$  phase was commonly observed in larger trivalent cations substitute  $\text{Zr}^{4+}$  [86, 87]. However, this indicates that phase transformation of SCGZ can occur after electrolyte sintering at

high temperature. Therefore, decreasing the sintering temperature of SCGZ electrolyte is one of the promising issues for further study. Although in this study  $\text{Sc}_2\text{ZrO}_{17}$  did not affect cell durability, the role and influence of the phase transformation in SCGZ should be further investigated.

For the electrolyte-supported cells, different electrolytes provided different pellet diameter and volume shrinkage after the sintering process, as presented in Fig. 34. The GDC, YSZ, and SCGZ pellets after sintering had a diameter of 2.22, 2.02, and 1.99 cm with 32.89%, 55.55%, and 60.78% volume shrinkage, respectively (Table 7). In case of GDC electrolyte, The YSZ blocking layer was deposited on the pellet to prevent the reduction of GDC single layer, caused the electron conduction across the electrolyte. After depositing YSZ buffer layer and firing, the cell diameter of bi-layered GDC/YSZ pellet reduced to 2.15 cm with 46.05% of volume reduction. The GDC/YSZ cell exhibited rather high volume shrinkage but the pellet densification was rather low.

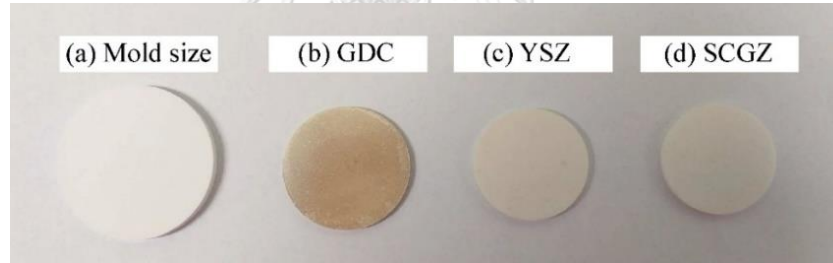


Fig. 34 Images of different electrolyte pellets after sintering



**Table 7** Effect of sintering temperature and pressing pressure on the volume shrinkage and relative density of GDC, YSZ, and SCGZ electrolyte

Sintering temperature (°C)	GDC		YSZ		SCGZ	
	Volume shrinkage (%)	Relative density (%)	Volume shrinkage (%)	Relative density (%)	Volume shrinkage (%)	Relative density (%)
	1200	36.91	87.76	-	-	-
1250	40.11	92.44	-	-	-	-
1300 (20 MPa)	41.67	94.92	-	-	-	-
1300 (1.7 MPa)	32.89	76	-	-	-	-
1350	47.44	>95	-	-	-	-
1400	48.84	>95	-	-	-	-
1450	49.76	>95	-	-	-	-
1450 (1.7 MPa)	-	-	55.55	98	60.78	> 95

SEM images revealed that the SCGZ and YSZ electrolytes were dense with the relative density of >95% and 98% for SCGZ and YSZ pellets, respectively while the GDC pellet was relatively less densified as presented in Fig. 35. The SCGZ pellet exhibited the largest grain size - the average grain size was 3.70  $\mu\text{m}$  for SCGZ and 2.12  $\mu\text{m}$  for YSZ, respectively. For bi-layered GDC/YSZ a thin layer of YSZ ( $\sim 3 \mu\text{m}$ ) on the GDC electrolyte was sufficiently dense, as presented in Fig. 35(d), corresponding to the work which was reported that 1-2  $\mu\text{m}$  thick YSZ was enough to prevent electronic conduction [88].

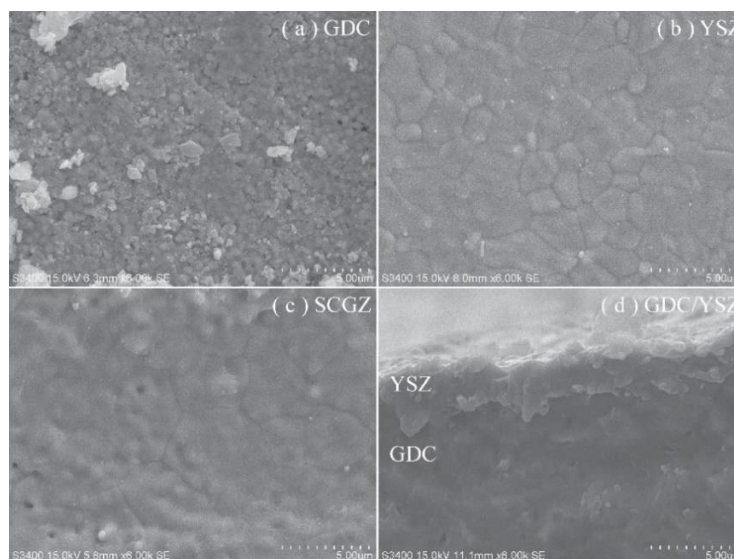


**Fig. 35** SEM images of (a) GDC sintered at 1300 °C, (b) YSZ sintered at 1450 °C, (c) SCGZ sintered at 1450 °C, and (d) cross-sectional image of the bi-layered GDC/YSZ electrolyte

Since the GDC pellet was rather difficult to be densified, the sintering behavior of the GDC pellets at different temperatures was investigated. The GDC electrolyte were pressed in a mold using different pressing pressures (20 MPa and 1.7 MPa) and fired at different temperatures (1200-1450 °C). Fig. 36 presents SEM images of the GDC pellets. When sintering temperature increased from 1200 °C to 1450 °C, the densification of the pellets increased. The shrinkage of the GDC pellet increased from 36.91 to 49.76% with increasing relative density of the pellet, as presented in Table 7. However, as increasing temperature (>1300 °C), cracking and color changing to brownish was observed on the pellet. The change in color can be ascribed to the phase changing in the material [87, 89, 90], adversely affecting the electrochemical performance of the GDC electrolyte. Therefore, the GDC sintering temperature of 1300 °C was chosen in this study. Different pressing pressure was also found to affect the relative density of the GDC electrolyte.

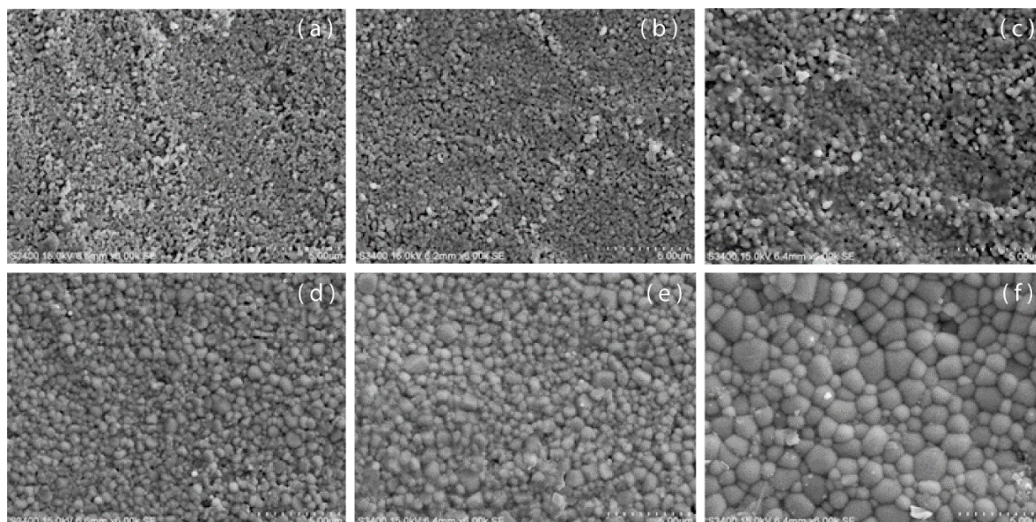


Fig. 36 SEM images of GDC electrolyte sintered at (a) 1200 °C, (b) 1250 °C, (c) 1300 °C, (d) 1350 °C, (d) 1400 °C, and (e) 1450 °C

## 4.2 Activation energy of conduction

Fig. 37 presents the conductivity of Pt/electrolyte/Pt cells observed in SOEC operation under steam to H<sub>2</sub> ratio of 70:30 at the cathode chamber (54%H<sub>2</sub>O, 23%H<sub>2</sub> and 23%N<sub>2</sub>, 325 ml min<sup>-1</sup> total flow rate) and ambient air at the anode chamber.

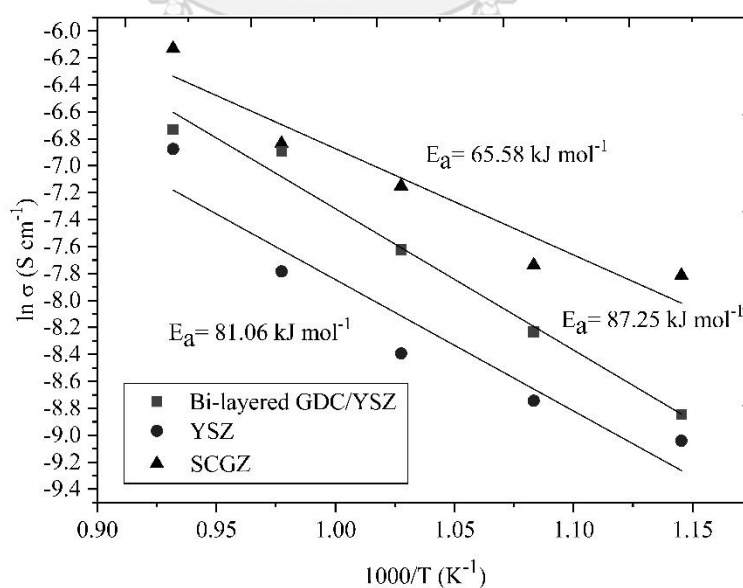
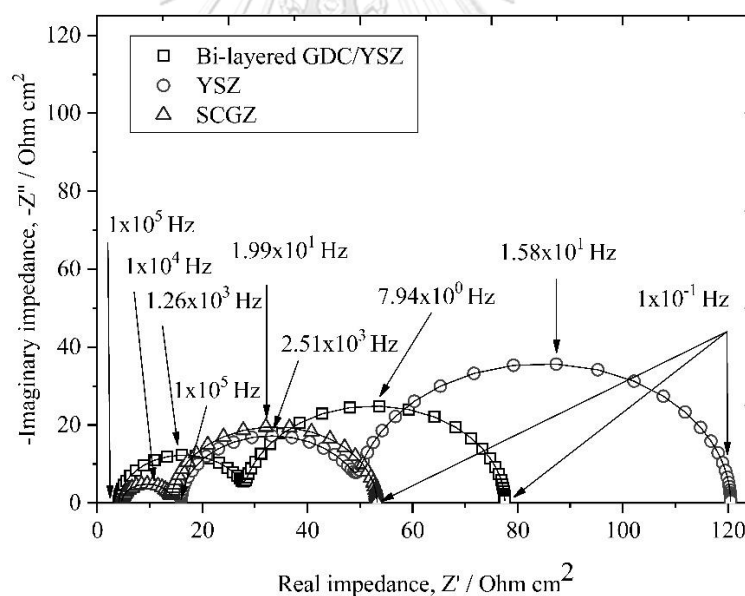


Fig. 37 Activation energy of conduction ( $E_a$ ) and the conductivity of Bi-layered GDC/YSZ, YSZ and SCGZ electrolyte at various operating temperatures

The activation energy of conduction was 65.58 and 81.06 and 87.25 kJ mol<sup>-1</sup> for SCGZ, YSZ and bi-layered GDC/YSZ, respectively. Although the conductivity was rather low, the activation energy of conduction of the YSZ and bi-layered GDC/YSZ electrolytes corresponded to the results reported from other works [82, 91]. The activation energy of conduction of the SCGZ (65.58 kJ mol<sup>-1</sup>) was relatively lowest among the studied electrolytes but slightly higher than ScSZ reported in literatures (~ 62 kJ mol<sup>-1</sup>) [24, 92]. It was reported that ionic radii of cation dopant significantly affects ionic conductivity of the electrolyte. Doping with the larger cations size such as Gd<sup>3+</sup> and Ce<sup>4+</sup> can block the migration of vacancies, leading to higher activation energy of ionic conduction [29, 82, 93]. Although small amounts of Gd<sup>3+</sup> and Ce<sup>4+</sup> (0.5 mol%, Sc<sub>0.1</sub>Ce<sub>0.005</sub>Gd<sub>0.005</sub>Zr<sub>0.89</sub>O<sub>2</sub>) were doped into ScSZ, they could affect the conductivity of the oxygen ions. The ionic radii of Sc<sup>3+</sup>, Y<sup>3+</sup>, Gd<sup>3+</sup>, Ce<sup>3+</sup>, Ce<sup>4+</sup> and Zr<sup>4+</sup> are 0.87 Å, 1.019 Å, 1.053 Å, 1.143 Å, 0.97 Å and 0.84 Å, respectively [24, 94]. The conductivity increased as a function of temperature and the results present that the SCGZ electrolyte could achieve higher performance than the YSZ and the bi-layered GDC/YSZ electrolyte. It was likely that the larger size of Y<sup>3+</sup> dopant compared with the host cation (Zr<sup>4+</sup>) adversely contributes to a larger steric blocking effect and hinders the oxygen ion migration through vacancy, comparing to doping smaller Sc<sup>3+</sup> ion [29, 82, 93]. The similar ionic radius between Sc<sup>3+</sup> dopant and Zr<sup>4+</sup> ion in the SCGZ electrolyte resulted in less steric blocking effect of oxygen-ion movement [24, 93, 95-98]. In case of the bi-layered GDC/YSZ electrolyte, rather low conductivity compared with other electrolytes was likely due to low densification of the electrolyte which has been reported to affect the cell conductivity [2, 3, 99]. The YSZ buffer layer was likely to cause low conductivity in the bi-layered GDC/YSZ electrolyte. It is worth noting that at lower temperature range, the difference in conductivity between the SCGZ and other electrolytes became larger, suggesting that SCGZ can be a promising candidate for an intermediate temperature operation (<650 °C).

### 4.3 Electrochemical performance of electrolyte-supported cells

The EIS of Pt/electrolyte/Pt electrolyte-supported cells were measured in SOEC mode at a constant potential of 1.1 V (800 °C and H<sub>2</sub>O to H<sub>2</sub> ratio of 70:30). The EIS response was fitted to an equivalent circuit composed of a resistor in series with two parallel constant phase elements. As presented in Fig. 38, all electrolytes exhibited two overlapping arcs. The high frequency (HF) intercept was due to the electrolyte lattice and lead response (i.e. bulk), arc at the high frequency region was due to electrolyte grain boundary. Lower frequency (LF) than the response of grain boundary including the lower frequency arc can be due to electrode response [73, 100]. The expected processes are  $10^{-12}$  F for the lattice;  $10^{-8}$  F for the grain boundary; and,  $10^{-5}$  F for the electrode. The HF intercept represents a low-time constant response such as lead resistance [101, 102].



**Fig. 38** The EIS response of Pt/electrolyte/Pt at controlled potential of 1.1 V, operating temperature of 800 °C, and H<sub>2</sub>O:H<sub>2</sub> ratio of 70:30 at the cathode chamber and ambient air at the anode chamber

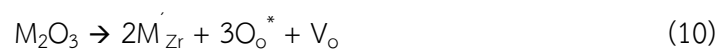
Table 8 presents the parameters extracted from the EIS response. The values of R and C were derived from equivalent circuit fitting. The sample thickness was

0.12 cm for GDC/YSZ and 0.16 cm for SCGZ and YSZ pellets and the electrode area was 0.502 cm<sup>2</sup>. Different electrolyte materials affected both HF-intercept, HF and LF arcs. The SCGZ electrolyte exhibited significantly smallest HF and LF arcs. This behavior corresponded well with the results in Fig. 37 in that the SCGZ electrolyte exhibited higher ionic conductivity than the YSZ electrolyte more than two times, especially in the intermediate temperature range.

**Table 8** Parameters extracted from the EIS response of Pt/electrolyte/Pt operating at controlled potential of 1.1 V, temperature of 800 °C, and H<sub>2</sub>O:H<sub>2</sub> ratio of 70:30 the cathode chamber and ambient air at the anode chamber

Parameter	Pt/YSZ/GDC/Pt	Pt/YSZ/Pt	Pt/SCGZ/Pt
HF intercept ( $\Omega \text{ cm}^2$ )	4.131	38.1	4.639
$R_{\text{HF}}$ ( $\Omega \text{ cm}^2$ )	23.92	80.23	9.512
$C_{\text{HF}}$ (F cm <sup>2</sup> )	$5.31 \times 10^{-6}$	$7.6 \times 10^{-7}$	$2.59 \times 10^{-6}$
$R_{\text{LF}}$ ( $\Omega \text{ cm}^2$ )	49.5	170	39.07
$C_{\text{LF}}$ (F cm <sup>2</sup> )	$3.9 \times 10^{-4}$	$5.53 \times 10^{-5}$	$2.2 \times 10^{-4}$
Total resistance ( $\Omega \text{ cm}^2$ )	77.551	288.33	53.221

The doping ZrO<sub>2</sub> with lower valent cation was reported to increase the oxygen vacancies formation leading to higher ionic conductivity, according to Kröger-Vink notation in Eq. (10).



Therefore, oxygen vacancies increase with the dopant contents, resulting in higher ionic conductivity [103]. However, as increasing dopant content, the complex defects between formed oxygen vacancies and dopant can occur and eventually lower the ionic conductivity [16]. In SCGZ, due to the closer ionic radius between Sc<sup>3+</sup> dopant and Zr<sup>4+</sup> host, doping with Sc<sup>3+</sup> provides more ion conductivity than doping Y<sup>3+</sup>. Large-size Y<sup>3+</sup> cation substituted Zr<sup>4+</sup> in YSZ will hinder the motion of oxygen and increase the elastic strain energy leading to lower ionic conductivity [16, 32]. It was

reported that the co-doping of  $Gd^{3+}$  with  $Sc^{3+}$  provides a higher ionic conductivity than the  $Sc^{3+}$  dopant in zirconia-based electrolyte [32]. In case of  $Ce^{4+}$  substitution, the oxygen vacancies are not formed. Nonetheless, the large ion radius of  $Ce^{4+}$  prefers to be eight-fold coordinated. Hence, the cubic symmetry is enhanced, leading to increasing ion conductivity [32, 85, 86, 104]. More amount of large dopant  $Y^{3+}$  substitution in YSZ than  $Ce^{4+}$  and  $Gd^{3+}$  substitution in SCGZ can also cause lower oxygen ion transportation. In addition, SCGZ exhibited a larger grain size which results in a lower grain boundary resistance to oxygen ion transportation as shown in Fig 35. For all these reasons, SCGZ could achieve the highest electrochemical performance among studied electrolytes. Although the GDC electrolyte should obtain high ionic conductivity due to the large ionic radius of  $Ce^{4+}$  host in ceria-based electrolyte, providing more open structure and facilitating oxygen ions conduction [103]. Low densification of the GDC could be attributed to low conductivity in the electrolyte. As can be seen in Fig. 35, the smaller grain size was observed, which played a drawback effect to the conductivity of oxygen ions leading to increasing grain boundary and resistance to oxygen ions transport and resulting in a lower ionic conductivity in the electrolyte. Moreover, the thermal expansion mismatch between YSZ and GDC in bi-layers as well as low ionic conductivity of YSZ buffer layer comparing to the GDC layer could contribute to a reduction in conductivity of the bi-layered electrolyte [88, 105].

A comparison of I/V curve of different electrolyte-supported cells was presented in Fig. 39. The operating potential was controlled from 0.5-1.8 V and operating temperature of 800 °C when  $H_2O:H_2$  at 70:30 was introduced to the cathode chamber and ambient air at the anode chamber.

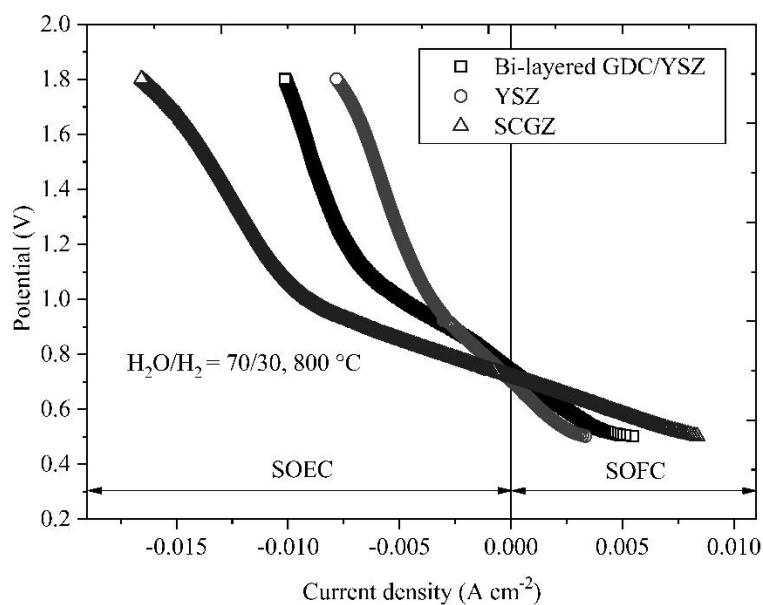


**Fig. 39** I/V response of Pt/electrolyte/Pt when the electrolyte is Bi-layered GDC/YSZ, YSZ and SCGZ, under H<sub>2</sub>O:H<sub>2</sub> ratio of 70:30 at the cathode chamber and ambient air at the anode chamber

The open circuit voltage (OCV) in this study was lower than the theoretical OCV which was calculated by Nernst potential equation. The OCV was 0.74, 0.71, and 0.72 V for bi-layered GDC/YSZ, YSZ, and SCGZ, respectively. The SCGZ electrolyte exhibited the lowest resistance in SOEC operation in accordance with the EIS response in Fig. 38. The hydrogen production rate was calculated from the I/V curve using Faraday's law. For electrolyte supported cell, the hydrogen production rate was also calculated at the apply voltage of 1.1 V from the I/V curve, and the rate was  $3.4 \times 10^{-8}$ ,  $2.20 \times 10^{-8}$ , and  $5.42 \times 10^{-8}$  mol s<sup>-1</sup> for bi-layered GDC/YSZ, YSZ and SCGZ cell, respectively.

#### 4.4 Microstructure analysis of Ni-SCGZ/SCGZ/BSCF cathode-supported cell

The cathode-supported cell (Ni-SCGZ/SCGZ/BSCF) was fabricated. Fig. 40 shows the SEM images of the cell - a layer of cathode, electrolyte, and anode. In an electrode structure, not only the connectivity of Ni metal and ceramic are required



for electron and ionic conduction, but a porous cathode structure is also required for diffusion of reactant gas to three phase boundary (electronic-conducting phase, ionic-conducting phase, and gas phase) [73, 99, 106]. In this study, the Ni-SCGZ cathode formed well Ni-ceramic networks but the structure was rather dense (Fig. 40(a)). Dense layer of electrolyte ( $\sim 20 \mu\text{m}$ ) was observed without delamination between electrolyte and electrode layers (Fig. 40(b)-(c)).

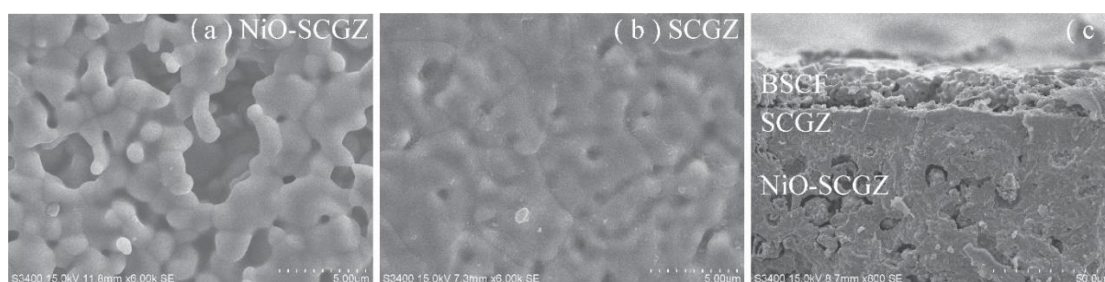


**Fig. 40** SEM image of (a) Ni-SCGZ electrode, (b) SCGZ electrolyte, and (c) cross-sectional image of Ni-SCGZ/SCGZ/BSCF layers

## 4.5 Electrochemical performance of cathode-supported cell

In order to evaluate the electrochemical performance of cathode-supported cells having different electrolyte materials, the  $I/V$  curve of the cells were taken under varied conditions. The variation of cell's performance with operating temperature (600-900 °C) and steam content ( $\text{H}_2\text{O}:\text{H}_2 = 60:40, 70:30$  and  $90:10$ ) was investigated. Moreover, the durability test of cathode-supported cells having different electrolytes was also carried out to determine the SOEC degradation.

### 4.5.1 Performance discrepancy between the electrolysis and galvanic modes

A comparison of  $I/V$  curve of different cathode-supported cells operated at 800 °C under steam to  $\text{H}_2$  ratio of 70:30 was shown as Fig. 41.

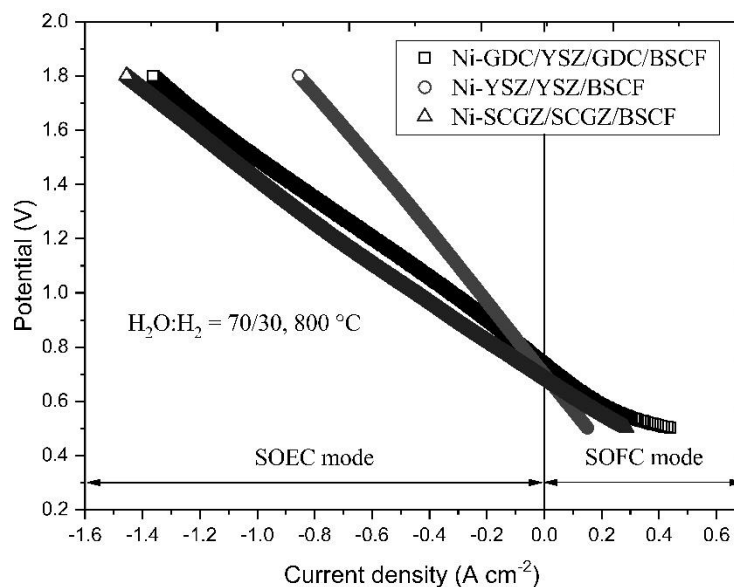


**Fig. 41** I/V response of Ni-electrolyte/electrolyte/BSCF when the electrolyte was Bi-layered GDC/YSZ, YSZ and SCGZ, operated at 800 °C under H<sub>2</sub>O to H<sub>2</sub> of 70:30 at the cathode and ambient air at the anode

As presented in Fig. 41, I/V response shows that the cathode-supported Ni-SCGZ/SCGZ/BSCF exhibited the highest performance in SOEC mode while the performance in SOFC mode was lower than that of Ni-GDC/YSZ/GDC/BSCF. The lower performance of the SCGZ cell in galvanic mode corresponded with the EIS response in Fig. 42. Interestingly, the result shows that the LF arc of the SCGZ cell significantly increased in galvanic mode when compared to the OCV and electrolytic mode even though the BSCF electrode was reported to exhibit lower performance in electrolysis mode [101]. The HF-intercept and the HF arc were rather similar. As shown in Table 9, the  $R_{LF}$  values significantly varied for different operating modes. This behavior seemed to be a sign of mass transport polarization due to low  $p_{H_2}$  in the galvanic operation.

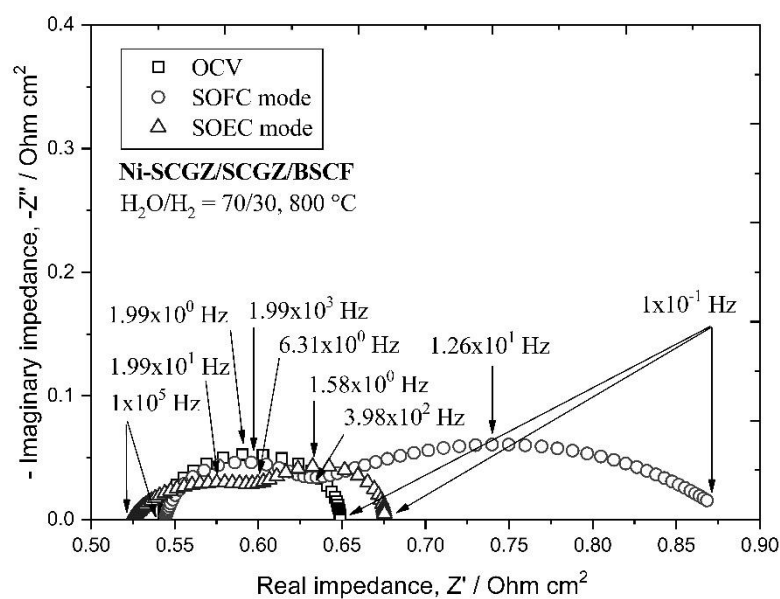


**Fig. 42** The EIS response of Ni-SCGZ/SCGZ/BSCF in electrolytic (1.1 V) and galvanic modes (0.6 V) at 800 °C under H<sub>2</sub>O:H<sub>2</sub> ratio of 70:30 at the cathode chamber and ambient air at the anode chamber

**Table 9** Parameters extracted from the EIS response of Ni-SCGZ/SCGZ/BSCF in electrolytic (1.1 V) and galvanic modes (0.6 V) at temperature of 800 °C and H<sub>2</sub>O:H<sub>2</sub> ratio of 70:30 the cathode chamber and ambient air at the anode chamber

Parameter	SOFC mode	SOEC mode
HF intercept ( $\Omega \text{ cm}^2$ )	2.095	2.034
$R_{\text{HF}}$ ( $\Omega \text{ cm}^2$ )	0.268	0.2014
$C_{\text{HF}}$ (F $\text{cm}^2$ )	$2.44 \times 10^{-4}$	$1.11 \times 10^{-2}$
$R_{\text{LF}}$ ( $\Omega \text{ cm}^2$ )	1.044	0.3929
$C_{\text{LF}}$ (F $\text{cm}^2$ )	$1.45 \times 10^{-2}$	0.2138
Total resistance ( $\Omega \text{ cm}^2$ )	3.407	2.6283

When the voltage of 1.1 V was applied at 800 °C under steam to H<sub>2</sub> ratio at 70:30, the cathode-supported cell gave H<sub>2</sub> production rate of  $2.4 \times 10^{-6}$ ,  $1.6 \times 10^{-6}$ , and  $3.00 \times 10^{-6} \text{ mol s}^{-1}$  for GDC/YSZ, YSZ, SCGZ cells, respectively. The gap of

H<sub>2</sub> production rate between SCGZ and YSZ cell was larger when the apply potential increased (see Table 10).

**Table 10** H<sub>2</sub> production rate of Ni-electrolyte/electrolyte/BSCF operating at varied applied potential 0.9-1.8 V at 800 °C under H<sub>2</sub>O to H<sub>2</sub> ratio of 70:30 at the cathode and ambient air at the anode

Applied potential (V)	H <sub>2</sub> production rate (μmol s <sup>-1</sup> )		
	GDC/YSZ	YSZ	SCGZ
0.9	1.02	0.78	1.60
1.2	3.09	1.95	3.75
1.5	5.22	3.16	5.68
1.8	7.07	4.43	7.54

#### 4.5.2 Effect of temperature

The operating temperature was varied ranging from 600 °C to 900 °C for the Ni-SCGZ/SCGZ/BSCF cathode-support cells as shown in Fig. 43. The H<sub>2</sub>O:H<sub>2</sub> was controlled at constant 70:30 during this experiment. The results showed that performance in both SOEC and SOFC modes were improved when increasing operating temperature, accounting for increasing ionic conductivity of the electrolyte and faster kinetics of the electrode which facilitated the reaction rates [72, 107, 108]. The behavior corresponded well with the results in Fig. 40 that the SCGZ cell exhibited dense electrolyte and porous cathode structure. However, it should be noted that high operating temperature can faster the cell degradation due to the coarsening of the Ni particle which can reduce the porosity of the electrode [109].

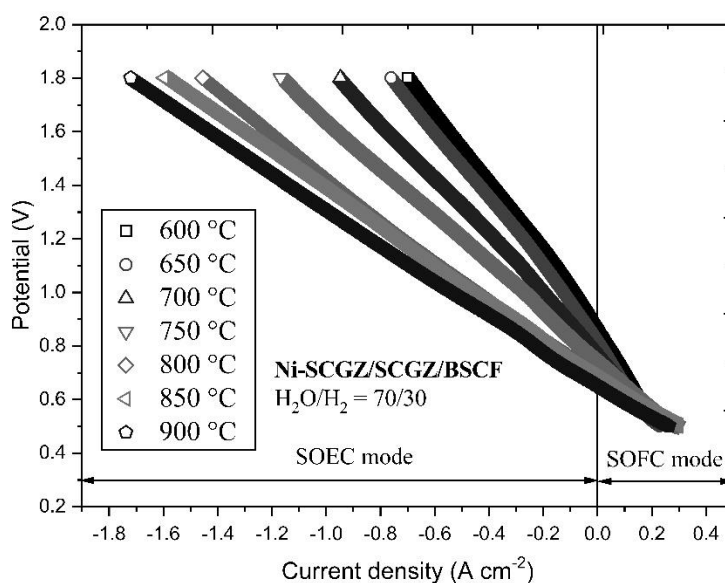


**Fig. 43** The I/V response of Ni-SCGZ/SCGZ/BSCF at varied operating temperatures from 600 °C to 900 °C ( $H_2O:H_2$  of 70:30 at the cathode chamber and ambient air at the anode chamber)

#### 4.5.3 Effect of steam content at hydrogen electrode

The effect of steam to hydrogen ratio at the hydrogen electrode in both electrolytic and galvanic modes was showed in term of I/V response in Fig. 44. In this experiment, the  $H_2O:H_2$  was varied over a range of 60:40 to 90:10 at controlled temperature of 800 °C. As presented in Fig. 44, varying steam to hydrogen ratio did not significantly affect the cell performance when the potential was controlled under 1.1 V. The discrepancy between SOEC and SOFC operation was insignificant at low applied potential. However, at higher applied potential, the effect of steam content was observed in SOEC operation and the discrepancy was seen. The hydrogen electrode could obtain more energy to break the bonds of steam and it was also reported that the oxygen can achieve more electrochemically transport from hydrogen electrode to the other side [109].

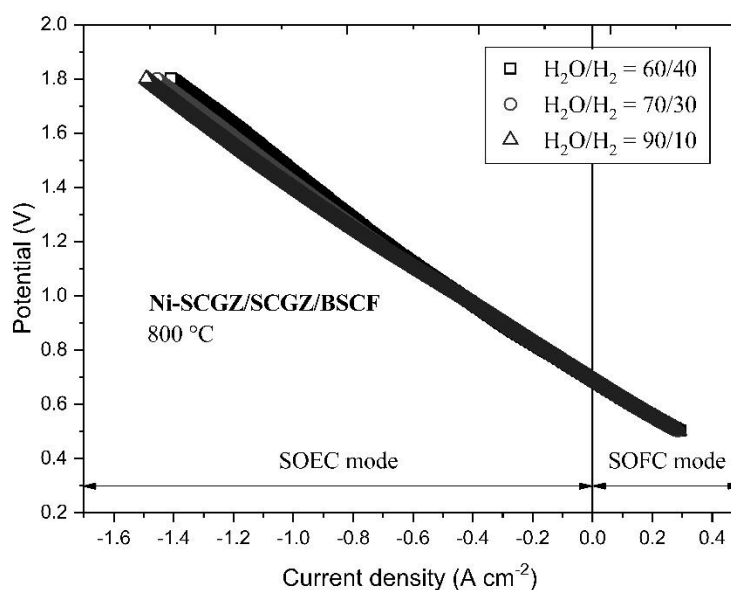


**Fig. 44** The I/V response of Ni-SCGZ/SCGZ/BSCF at varied steam to hydrogen from 60:40 to 90:10 at 800 °C

#### 4.5.4 Durability test

For durability test, the potential of cathode-supported cell (Ni-electrolyte/electrolyte/BSCF) was monitored at constant current density of 0.3 A cm<sup>-2</sup> for 60 hours at 800 °C under steam to H<sub>2</sub> ratio of 70:30 (Fig. 45). A significant decay of performance was observed for Ni-GDC/YSZ/GDC/BSCF - increasing voltage from initial 0.798 V to 1.269 V (degradation rate of 0.0057 V h<sup>-1</sup>). Despite showing relatively low initial performance of 1.34 V, Ni-YSZ/YSZ/BSCF cell showed insignificant performance degradation under the same operating conditions. Ni-SCGZ/SCGZ/BSCF also showed rather stable performance over 60 h of operation. The SEM images of the cell after durability test were presented in Fig. 46. Although, Ni-SCGZ electrode seemed rather dense due to Ni coarsening, SCGZ electrolyte was still dense without any cracking. In this study, BSCF electrode remained attaching to the SCGZ electrolyte although in our previous study, BSCF showed a sign of detachment from YSZ electrolyte after prolong operation [48]. It was reported that oxygen electrode detachment can be observed in case of using highly Co doped-cathode material [48, 110]. Moreover, BSCF has a large thermal expansion coefficient (TEC, 19.6×10<sup>-6</sup> K<sup>-1</sup>) when compared with YSZ (9.0×10<sup>-6</sup> K<sup>-1</sup>), and SCGZ (10.3×10<sup>-6</sup> K<sup>-1</sup>) [111, 112]. It should be noted that

the TEC of YSZ is for 8 mol% yttria doping – Increasing yttrium content decreases TEC of YSZ [112]. It was likely that less difference of TEC between SCGZ and BSCF may affect the attachment of BSCF after durability test.

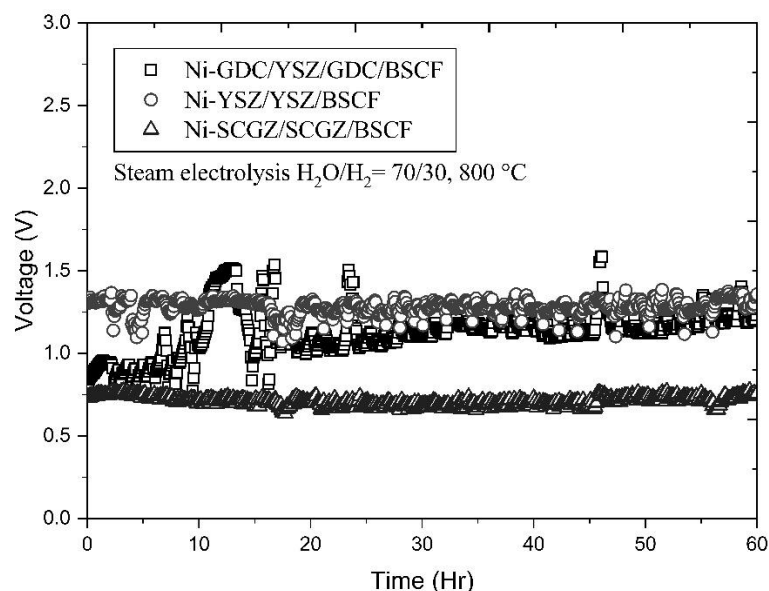


**Fig. 45** Potential monitoring of cathode-supported cells under electrolysis condition ( $0.3 \text{ A cm}^{-2}$  for Ni-GDC/YSZ/GDC/BSCF, Ni-YSZ/YSZ/BSCF and Ni-SCGZ/SCGZ/BSCF,  $800 \text{ }^\circ\text{C}$ ,  $\text{H}_2\text{O}:\text{H}_2 = 70:30$ , 60 h)

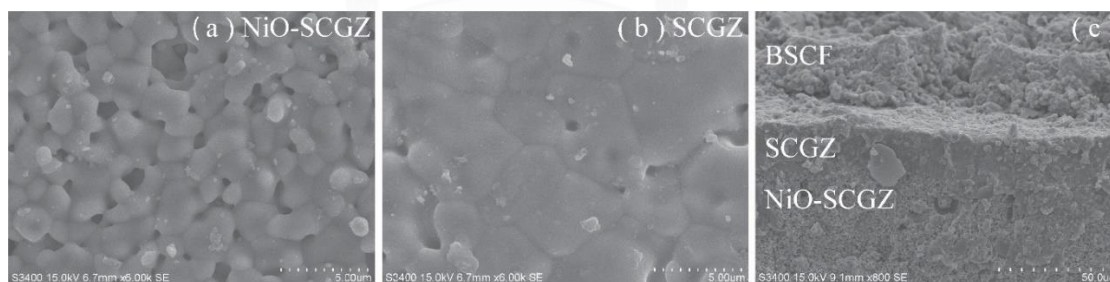


**Fig. 46** SEM images of (a) Ni-SCGZ electrode, (b) SCGZ electrolyte, and (c) cross-sectional image of Ni-SCGZ/SCGZ/BSCF layers after durability test

XRD patterns of Ni-SCGZ/SCGZ/BSCF after durability test was shown in Fig. 47. Comparing to the XRD patterns of fresh SCGZ (Fig. 32), it was clearly seen that there was no additional rhombohedral  $\beta$  phase ( $\text{Sc}_2\text{ZrO}_{17}$ ) after prolong operation with high temperature.

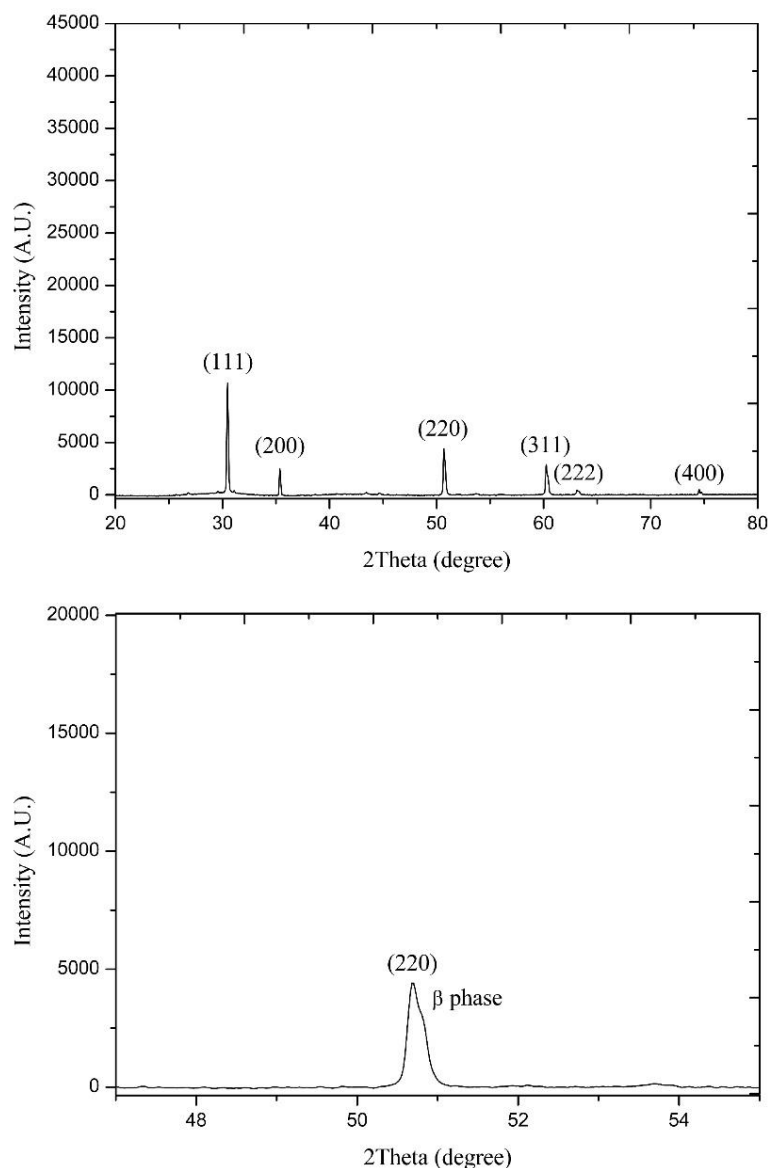


Fig. 47 X-ray diffraction pattern after durability test: (top) sintered SCGZ electrolyte (bottom) magnified peak over  $2\theta$  ranging from  $46^\circ$  to  $56^\circ$

#### 4.6 Oxidation tolerance of Ni-electrolyte

The oxidation of Ni to NiO for Ni-electrolyte powder was investigated at  $800^\circ\text{C}$  in air by TGA technique to measure the weight change of the samples. The test was to determine the stability of the cathode in oxidizing environment with different electrolytes. It is noted that the oxidation in air was rather severe condition when compared to the SOEC operating condition with a partial pressure of steam in the



cathode chamber. A full oxidation of Ni-electrolyte powder occurred within a few minutes as shown in Fig. 48.

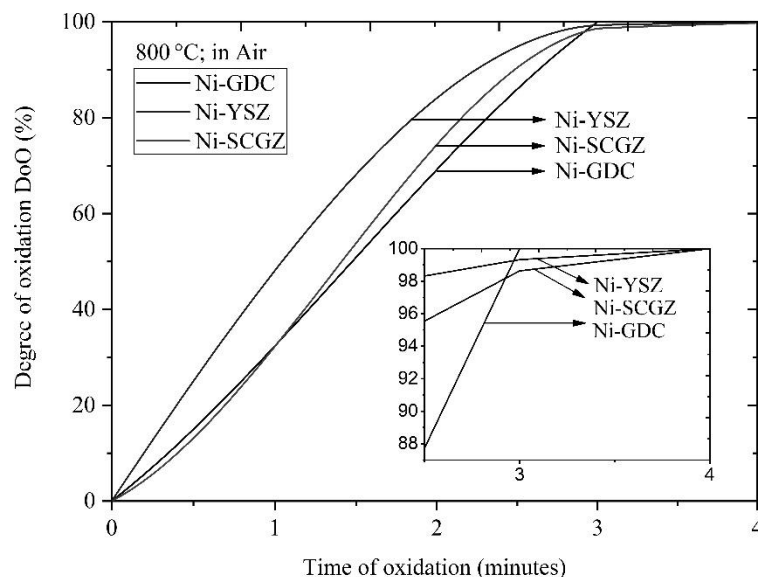


**Fig. 48** The oxidation of Ni-electrolyte (GDC/YSZ, SCGZ and YSZ) cermet at 800 °C in air

Among the different electrolytes, Ni-GDC cathode reached full oxidation within the shortest time (~3 minutes) although initially showed slower oxidation rate, followed by the Ni-YSZ (~4 minutes) and Ni-SCGZ (~4 minutes), respectively. The TGA/DSC analysis of electrolyte powders from room temperature to 1000 °C was reported in Fig. 49. The SCGZ electrolyte powder exhibited the lowest weight loss comparing to other electrolytes. Weight loss of the electrolyte powder were 0.86%, 1.08%, and 0.75% for GDC, YSZ and SCGZ respectively.

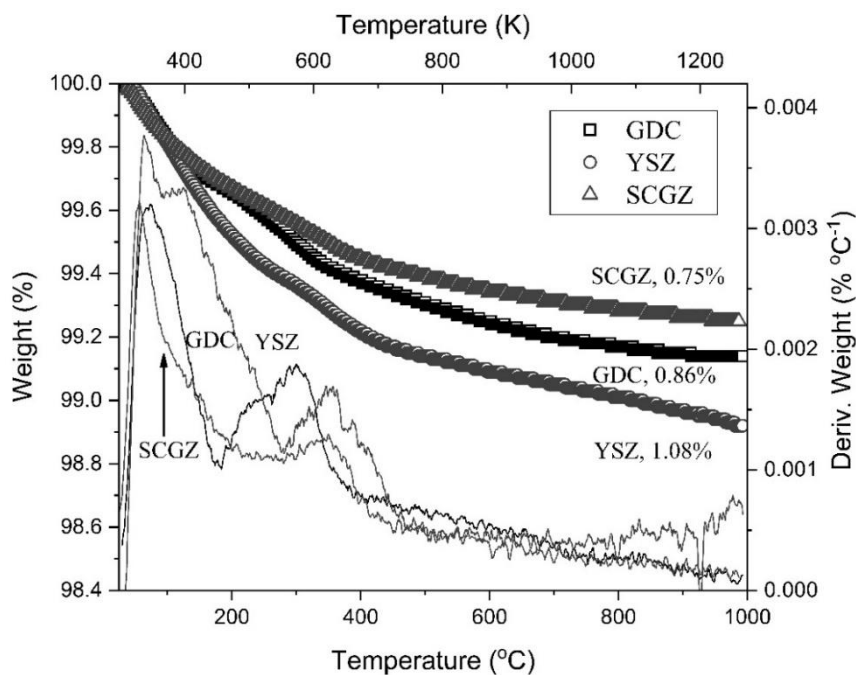


Fig. 49 TGA/DSC of electrolyte powder (GDC, SCGZ and YSZ)

#### 4.7 Rhombohedral phase suppression for SCGZ electrolyte

In previous study demonstrated that low conducting phase (rhombohedral  $\beta$ -phase,  $\text{Sc}_2\text{ZrO}_{17}$ ) was detected in the SCGZ electrolyte after sintering at high temperature. The rhombohedral  $\text{Sc}_2\text{ZrO}_{17}$  phase was reported to distort the lattice structure, leading to a reduction in ion conductivity. In addition, high sintering temperature is inevitable when using the micron- or submicron-sized powders [113].

However, the weak intensity of  $\beta$  phase was commonly observed in larger trivalent cations substitute  $\text{Zr}^{4+}$ . Bismuth oxide ( $\text{Bi}_2\text{O}_3$ ) was reported to be used as a sintering aid to decrease sintering temperature together with suppression of the rhombohedral phase in ScSZ [35, 114-116]. Therefore, the phase characterization, sintering behavior, and electrochemical performance over a range of temperatures for 1-2 mol% of  $\text{Bi}_2\text{O}_3$  doped in SCGZ electrolyte were investigated comparing to the bare SCGZ. Decreasing unwanted rhombohedral  $\beta$ -phase, lowering sintering temperature, and increasing ion conductivity were expected in the presence of  $\text{Bi}_2\text{O}_3$ .

#### 4.7.1 Phase analysis and microstructure

X-ray diffraction (XRD) patterns of the sintered SCGZ electrolyte pellet at 500-1450 °C are shown in Figs. 50-51. The SCGZ electrolyte without Bi<sub>2</sub>O<sub>3</sub> doping exhibited the rhombohedral β phase (Sc<sub>2</sub>Zr<sub>7</sub>O<sub>17</sub>, JCPDS No. 89-5486), which is a low conducting phase, together with the main cubic phase (JCPDS No. 89-5485) at sintering temperature above 1300 °C. The intensity of the peak increased with sintering temperature, noticed by the ratio of the peak area of the rhombohedral to the cubic phase as a function of temperature, as shown in Table 11.

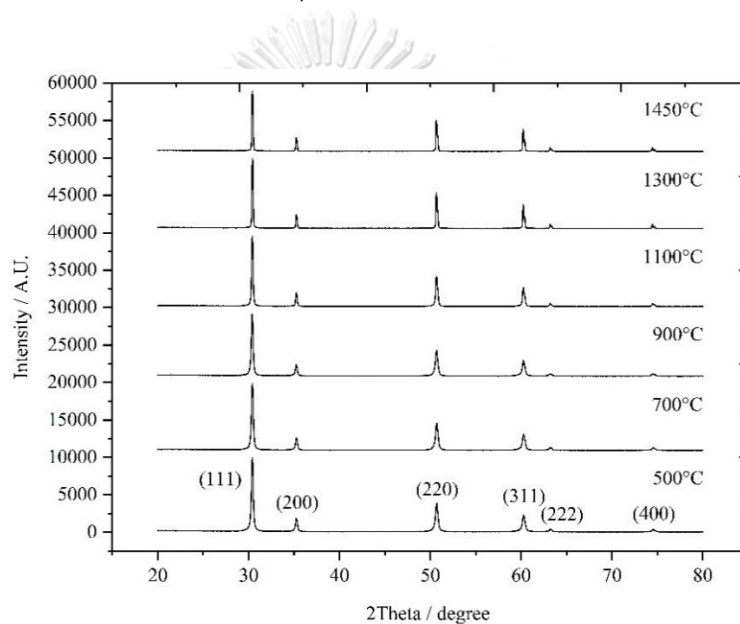
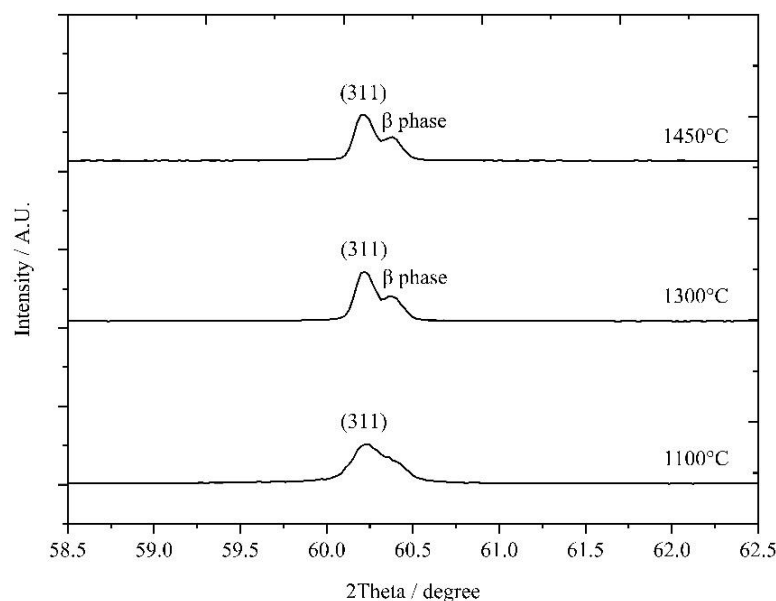


Fig. 50 The XRD patterns of the SCGZ pellets sintered at 500 °C to 1450 °C



**Fig. 51** Magnified scale of the XRD pattern of the SCGZ sintered at 1100-1450 °C

**Table 11** The XRD peak area ratio of the rhombohedral to the cubic phase (sintered SCGZ electrolyte at 1300 °C and 1450 °C for 4 hours)

Temperature (°C)	Rhombohedral/cubic peak area ratio	Peak area of Cubic phase	Peak area of Rhombohedral phase
1300	0.746	106.064	79.124
1450	0.767	101.658	77.972

Therefore, decreasing the sintering temperature of the SCGZ electrolyte below 1300 °C was expected to be a promising way to prohibit the formation of rhombohedral  $\beta$  phase. However, less densified electrolyte with a porous structure was observed when sintering temperature was below 1300 °C as shown in Fig. 52. It is known that the electrolytes in SOEC should have the relative density above 90% to prohibit the recombination of  $H_2$  and  $O_2$  from both electrode chambers, corresponded with previous studies that the SCGZ sintered at 1450 °C could achieve sufficient densification [117, 118].

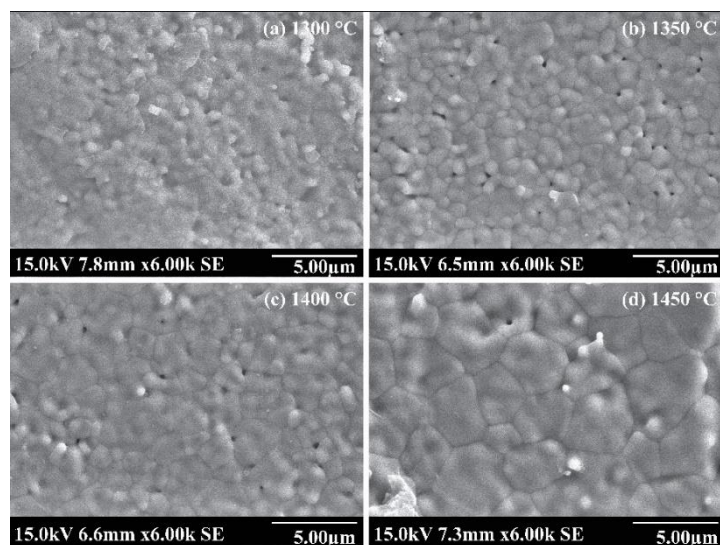


**Fig. 52** SEM images of the SCGZ electrolyte sintered at varied temperatures: (a) 1300 °C; (b) 1350 °C; (c) 1400 °C; and (d) 1450 °C

Thus,  $\text{Bi}_2\text{O}_3$  was doped into the SCGZ. Phase formation of 1 and 2 mol%  $\text{Bi}_2\text{O}_3$ -added SCGZ (1Bi10SCGZ, 2Bi10SCGZ) compared to bare SCGZ electrolyte sintered at 1450 °C were studied. Fig. 53 shows the XRD patterns of the SCGZ with different  $\text{Bi}_2\text{O}_3$  contents, sintered at 1450 °C.

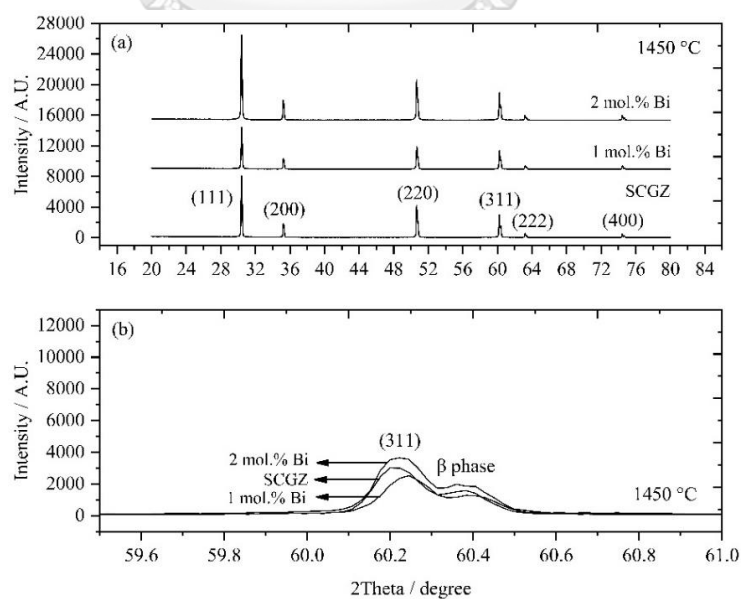


**Fig. 53** The XRD patterns of (a) the SCGZ with different  $\text{Bi}_2\text{O}_3$  contents, sintered at 1450 °C (b) magnified scale over  $2\theta$  ranging from 59.5° to 61°

It can be seen that the (311) peak position of 1 and 2 mol% Bi<sub>2</sub>O<sub>3</sub>-doped SCGZ shifted to the higher diffraction angle compared to the XRD pattern of bare SCGZ, corresponded with no detection of separated Bi<sub>2</sub>O<sub>3</sub> peaks. The shrinkage in lattice parameter from 5.0914 to 5.0891 Å was detected when doping 1 mol% Bi<sub>2</sub>O<sub>3</sub> into SCGZ structure. This can confirm that the Bi<sup>3+</sup> was incorporated in the structure, forming the solid solution of Bi<sub>2</sub>O<sub>3</sub> and SCGZ. It should be noted that the oxidation number of most doping elements are +3 and the ionic radius of Bi<sup>3+</sup> (0.96 Å) are similar enough to the Sc<sup>+3</sup> (0.87 Å), Zr<sup>+4</sup> (0.84 Å) and Gd<sup>+3</sup> (1.053 Å) ions to form a solid solution. It was reported that the difference of ionic radius between Sm<sup>3+</sup> and Zr<sup>4+</sup> was approximately 0.24 Å and it was able to form a solid solution [31, 119]. Therefore, these cations are most likely to be substituted by Bi<sup>3+</sup>, forming a solid solution. However, the Bi<sub>2</sub>O<sub>3</sub>-doped SCGZ electrolyte in this study still exhibited the mixture of cubic and rhombohedral β phase. According to the kinetics report, it is difficult to reach an equilibrium phase assemblage for scandia-zirconia system due to a close ionic radius between Sc<sup>+3</sup> (0.87 Å) and Zr<sup>+4</sup> (0.84 Å), leading to the slow diffusion kinetics of cations in structure; allowing the formation of rhombohedral β phase [120].

As the most diffraction angles of the cubic and rhombohedral phases were nearly close [115], therefore, the ratio of the peak area of rhombohedral to cubic phase was calculated as a function of Bi<sub>2</sub>O<sub>3</sub> concentration as shown in Fig. 54. Although the area of the rhombohedral peak (impurity phase) did not show a decreasing trend along with increasing Bi<sub>2</sub>O<sub>3</sub> dopant concentration due to the differences in the baseline levels effecting the peak intensity; however, the peak area ratio of rhombohedral to cubic phase (main phase) decreased as increasing Bi<sub>2</sub>O<sub>3</sub> concentration indicating that the addition of Bi<sub>2</sub>O<sub>3</sub> could suppress the unwanted rhombohedral phase in SCGZ. The peak area ratio of 0.77, 0.73 and 0.70 were obtained for the addition of 0, 1 and 2 mol% Bi<sub>2</sub>O<sub>3</sub>, respectively. It is worth comparing this work to other works. In this study, with 2 mol% Bi<sub>2</sub>O<sub>3</sub> dopant the SCGZ exhibited 41% of rhombohedral phase while in other work, with 3.3 mol% Al<sub>2</sub>O<sub>3</sub> dopant the ScSZ exhibited 50% of rhombohedral phase [27]. It should be noted that different fabricating process can also affect the amount of the unwanted

phase although similar composition of dopant is used [121]. Bai et al. [35, 122] also reported that a small amount of rhombohedral phase was observed for CeO<sub>2</sub>-doped scandia-stabilized zirconia (10Sc1CeSZ) sintered at high temperature (1400 °C) as well as 2 mol% Bi<sub>2</sub>O<sub>3</sub>-doped ScSZ sintered above 1300°C. This indicates that the rhombohedral phase of zirconia thermodynamically prefers high sintering temperatures, even the dopant has been added to stabilize the cubic phase. This corresponded well with the results in this study in that the formation of rhombohedral phase was not completely inhibited at sintering temperature above 1300°C, even adding Bi<sub>2</sub>O<sub>3</sub> dopant. For this reason, sintering behavior of the 1-2 mol% Bi<sub>2</sub>O<sub>3</sub>-doped SCGZ samples at different temperatures was further studied.

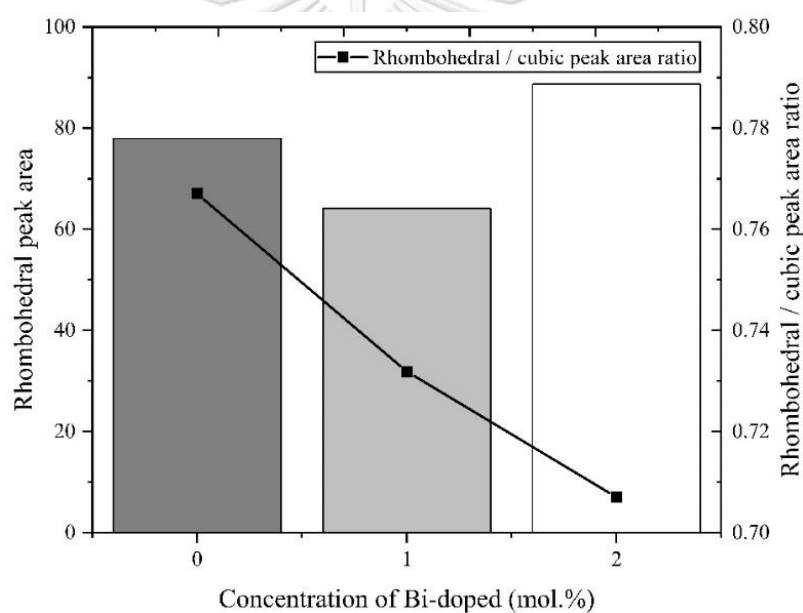


**Fig. 54** The XRD peak area ratio of rhombohedral to cubic phase in SCGZ with different Bi<sub>2</sub>O<sub>3</sub> concentrations, sintered at 1450 °C for 4 hours

Different amounts of Bi<sub>2</sub>O<sub>3</sub> adding into SCGZ structure provided different linear shrinkage and relative density, as presented in Table 12.

**Table 12** The percentages of volume shrinkage and relative density of 0-2 mol% Bi<sub>2</sub>O<sub>3</sub>-doped SCGZ electrolyte at different sintering temperatures

Temperature (°C)	SCGZ		1 mol% Bi <sub>2</sub> O <sub>3</sub>		2 mol% Bi <sub>2</sub> O <sub>3</sub>	
	Linear shrinkage (%)	Relative density (%)	Linear shrinkage (%)	Relative density (%)	Linear shrinkage (%)	Relative density (%)
	1150	11.40	55.23	12.13	56.16	13.97
1200	15.07	66.45	15.44	67.03	16.54	72.63
1250	21.32	77.42	21.32	77.42	21.32	86.53
1300	23.16	81.17	23.16	93.68	24.63	94.57
1350	25.73	91.72	26.10		26.84	
1400	26.83	>95	27.57	> 95	27.57	> 95
1450	26.83		27.57		27.94	

Increasing sintering temperature could increase both linear shrinkage and relative density of the samples. The linear shrinkage of 1 and 2 mol% Bi<sub>2</sub>O<sub>3</sub>-doped SCGZ was significantly higher than undoped SCGZ over the range of 1150-1450 °C, and 2 mol% Bi<sub>2</sub>O<sub>3</sub>-doped SCGZ exhibited the highest shrinkage rate. The linear shrinkage of 1 mol% Bi<sub>2</sub>O<sub>3</sub>-doped SCGZ was higher than undoped SCGZ about 2-7% while it was 4-23% for 2 mol% Bi<sub>2</sub>O<sub>3</sub>-doped SCGZ. As increasing sintering temperature (1150-1450 °C), percentage difference of the linear shrinkage between doped and undoped sample decreased. This indicates that doping SCGZ with Bi<sub>2</sub>O<sub>3</sub> improved the sinterability and the linear shrinkage was not linearly proportional, especially at high sintering temperature. As increasing sintering temperature from 1150 to 1450 °C, the relative density of 0, 1 and 2 mol% Bi<sub>2</sub>O<sub>3</sub>-doped SCGZ increased from 55.23 to >95%, 56.15 to >95% and from 61.52 to >95%, respectively. In this study, more amount of Bi<sub>2</sub>O<sub>3</sub> dopants also provided higher densification in the electrolyte pellet at lower sintering temperatures. For SCGZ, sintering temperature up to 1450 °C was used to reach high relative density in electrolyte (>95%). For both of 1Bi10SCGZ and 2Bi10SCGZ, a lower sintering temperature of approximately 1350



°C was sufficient to reach high relative density, corresponding to SEM images presented in Figs. 55 and 56. It should be noted that not only sintering aid can improve the sinterability of electrolyte but the use of nanometer- or submicron-electrolyte starting-powders derived from wet synthesis, e.g. sol-gel [123], can facilitate the growth of electrolyte densification [124].

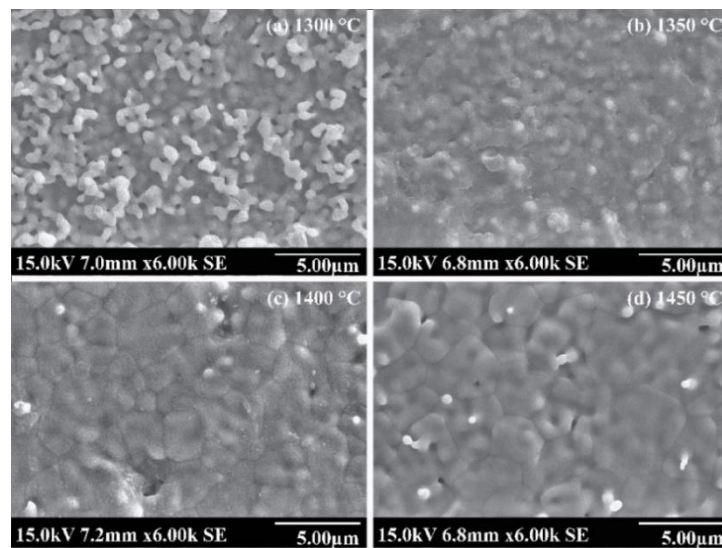


**Fig. 55** SEM images of 1 mol% Bi<sub>2</sub>O<sub>3</sub>-doped SCGZ at different sintering temperatures: (a) 1300 °C; (b) 1350 °C; (c) 1400 °C; and (d) 1450 °C

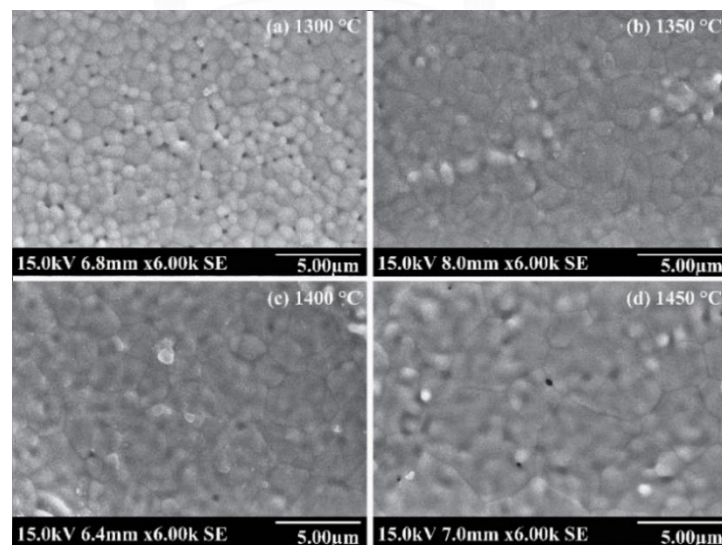


**Fig. 56** SEM images of 2 mol% Bi<sub>2</sub>O<sub>3</sub>-doped SCGZ at different sintering temperatures: (a) 1300 °C; (b) 1350 °C; (c) 1400 °C; and (d) 1450 °C

However, at sintering lower than 1350°C, the grain boundaries were not obviously observed on 1Bi10SCGZ electrolyte. There are reports that small grain size can increase the density of grain boundaries and inhibit ion mobility in oxygen vacancies, resulting in the lower ion conductivity of an electrolyte [86, 125]. Therefore, 1350 °C is the lowest temperature which can suppress the unwanted rhombohedral phase while maintaining sufficient electrolyte density and providing a large grain size for 2Bi10SCGZ electrolyte. In this study, Bi<sub>2</sub>O<sub>3</sub> was found to act as both phase stabilizer and sintering aid to help decrease unwanted rhombohedral phase while increasing electrolyte densification. It should be noted that there are several variables affecting phase stabilization; e.g. incomplete phase reaction, thermal properties of ceramic, type of host, the amount of dopant, and fabrication procedures. Therefore, it is possible to observe the partially stabilize cubic structure for phase stabilizer addition [31, 82, 126].

The grain size increased with increasing sintering temperature and the amount of Bi<sub>2</sub>O<sub>3</sub>, as shown in Table 13.

**Table 13** Average grain size of the sintered SCGZ electrolyte with and without Bi<sub>2</sub>O<sub>3</sub> doping (1-2 mol%)

Temperature (°C)	Average Grain Size (µm)		
	SCGZ	1Bi10SCGZ	2Bi10SCGZ
1300	-	-	1.16
1350	1.01	-	1.92
1400	2.21	2.28	2.54
1450	3.45	3.57	3.66

The 2Bi10SCGZ (2 mol% Bi<sub>2</sub>O<sub>3</sub>-doped SCGZ) sintered at 1350 °C exhibited the grain size of 1.92 µm, which relatively higher than the SCGZ without Bi<sub>2</sub>O<sub>3</sub> (1.01 µm) at the same sintering temperature. In comparison, the grain size distribution of the 2Bi10SCGZ was broader than SCGZ. The grain size distribution of SCGZ ranged from 0.49 to 2.34 µm while the 2Bi10SCGZ ranged from 0.91 to 3.44

$\mu\text{m}$ . However, the grain size distribution in 2Bi10SCGZ was more uniform with a tendency toward a normal distribution, as shown in Fig. 57.

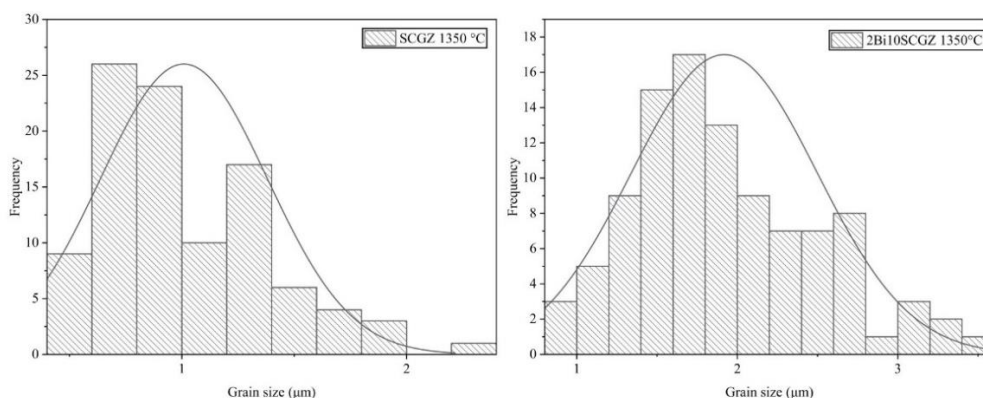


**Fig. 57** Grain size distribution of SCGZ (left) and 2Bi10SCGZ (right) sintered at 1350 °C

When compared to other sintering aid such as CuO, the SCGZ with 0.5 wt% CuO exhibited relatively larger grain size of 3.32  $\mu\text{m}$  [127]. The different electrolyte morphology, especially grain size and its boundary, was affected by the type of sintering aid [34, 115]. In this study, 1-2 mol% Bi<sub>2</sub>O<sub>3</sub> doping did not significantly change the grain size of the SCGZ electrolyte. This can be caused by the formation of solid solution. The Bi<sup>3+</sup> seemingly incorporated into the SCGZ structure, confirming by the XRD patterns as mentioned earlier. Generally, the increasing grain size with sintering aid can be explained by the liquid-phase sintering [113]. Due to the low melting point of sintering aid, electrolyte particles were surrounded by liquid phase of sintering aid. The surface atom of the electrolyte can diffuse greatly in liquid phase; thus, the grain growth rate increases in this environment [128, 129]. Moreover, the pore filling process by liquid-phase sintering aid can promote the densification, resulting in the electrolyte pellet with a larger grain size and a higher relative density [130].

#### 4.7.2 Electrochemical performance measurement

The electrochemical performance of the Pt/electrolyte/Pt cells were examined using a current linear sweep method and the AC impedance measurement

(EIS response). The conductivity and activation energy of conduction of electrolyte significantly depend on the electrolyte sintering condition since different microstructure and electrolyte densification can affect oxygen ion transport [131]. Therefore, sintering temperature which provided sufficient densification of the electrolyte was used to study the electrochemical performance. The conductivity and activation energy of conduction of SCGZ sintered at 1450 °C and 2Bi10SCGZ sintered at 1350 °C (2Bi10SCGZ, 1350 °C) were calculated from I/V curves in SOEC operation under the H<sub>2</sub>O:H<sub>2</sub> ratio of 70:30 at the cathode chamber varied from 600-800 °C as presented in Fig 58.

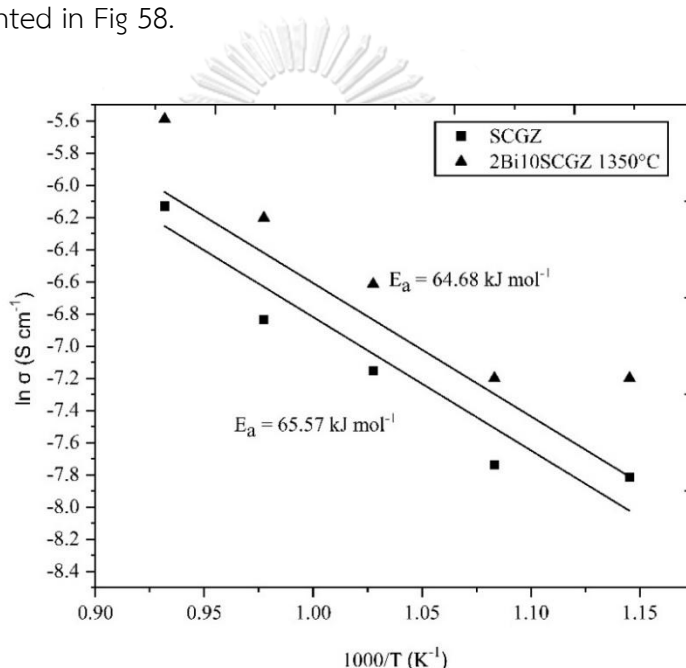


**Fig. 58** Activation energy of conduction ( $E_a$ ) and the conductivity of SCGZ sintered at 1450 °C and 2Bi10SCGZ sintered at 1350 °C

The activation energy ( $E_a$ ) of conduction of SCGZ sintered at 1450 °C and 2Bi10SCGZ sintered 1350 °C was 65.57 and 64.68 KJ mol<sup>-1</sup>, respectively. The activation energy of conduction of 2Bi10ScSZ was rather similar to the SCGZ electrolyte although the conductivity of 2Bi10SCGZ was higher than the bare SCGZ. Comparing to other works, the activation energy of conduction of 2 mol% Bi<sub>2</sub>O<sub>3</sub> doped SCGZ (2Bi10SCGZ) in this study was still higher than that of ScSZ (about 60 kJ mol<sup>-1</sup>, [24]) and 1 mol% Bi<sub>2</sub>O<sub>3</sub> doped ScSZ (63.9 kJ mol<sup>-1</sup>, [132]). For ScSZ, the oxygen

vacancies are generated by  $\text{Sc}^{3+}$  substituted  $\text{Zr}^{4+}$ , corresponded with Kroger-Vink notation. For  $\text{Bi}_2\text{O}_3$ -doped in ScSZ,  $\text{Bi}^{3+}$  exhibits larger radii (0.96 Å) than  $\text{Sc}^{3+}$  (0.87 Å) [132, 133]. The larger radii of dopants compared with the  $\text{Zr}^{4+}$  host (0.84 Å) can lead to more elastic strain and migration enthalpy which makes it more difficult for oxygen vacancy migration [129]. Although  $\text{Bi}_2\text{O}_3$  was found to act as an oxygen barrier, relatively higher conductivity of 2Bi10SCGZ electrolyte was achieved in this study, likely due to increased densification in the electrolyte and phase stabilization. Doping of  $\text{Bi}_2\text{O}_3$  into SCGZ can enhance the conductivity although the  $\text{Bi}_2\text{O}_3$ -doped SCGZ had a smaller grain size (1.92  $\mu\text{m}$ ) compared with the bare SCGZ (3.45  $\mu\text{m}$ ). This agrees well with the works of Mori et al. and Sarat et al. who reported that the small amount of Bi diffuses into the lattice structure of ScSZ, stabilizes high conducting cubic phase of ScSZ and improves ionic conductivity [115, 134]. In this study, the  $\text{Bi}_2\text{O}_3$  was found to act as both phase stabilizer and sintering aid.

Comparing between SCGZ and ScSZ,  $\text{Bi}_2\text{O}_3$  dopant provides a better benefit to SCGZ in term of increasing conductivity. The conductivity of  $\text{Bi}^{3+}$ -doped ScSZ is relatively lower than ScSZ reported in other work [135], unlike  $\text{Bi}^{3+}$ -doped SCGZ in this study which provide higher conductivity than bare SCGZ. It was like that ScSZ exhibited more open structure, leading to higher oxygen ion mobility. For SCGZ, the larger dopants than  $\text{Bi}^{3+}$  (e.g.  $\text{Gd}^{3+}$  (1.053 Å) and  $\text{Ce}^{4+}$  (0.97 Å)) was incorporated in the structure, reducing the open structure.

The impedance analysis of electrolyte-supported cells was measured at 800 °C under potentiostatic mode of 1.1 V (SOEC mode) and  $\text{H}_2\text{O}:\text{H}_2$  ratio of 70:30, as presented in Fig. 59. SCGZ electrolyte was sintered at 1450 °C and 2Bi10SCGZ electrolyte was sintered at 1350 °C. Table 14 shows the parameters obtained from the EIS response. The EIS response was fitted to an equivalent circuit consisting of a resistor in series with two parallel of CPE/resistor. The high-frequency intercept of EIS presents the lead response and electrolyte lattice resistance. The high-frequency arc presents the oxygen ion mobility of electrolyte and electrolyte grain boundary while the low-frequency arc presents mass transport effect as well as electrode response [73, 100]. It was reported that the capacity for lattice or bulk, grain boundary and electrode is  $10^{-12}$  F,  $10^{-11}$ - $10^{-8}$  and  $10^{-7}$ - $10^{-5}$ , respectively [101, 136]. It was observed

that the impedance resistance decreased in 2Bi10SCGZ, compared with undoped SCGZ. HF-intercept and LF arc significantly decreased in 2Bi10SCGZ while HF arc slightly increased. It should be noted that to achieve >95% relative density, the SCGZ was sintered at 1450 °C and the 2Bi10SCGZ was sintered at 1350 °C. Different electrolyte composition and sintering temperature can cause different impedance spectra of the samples.

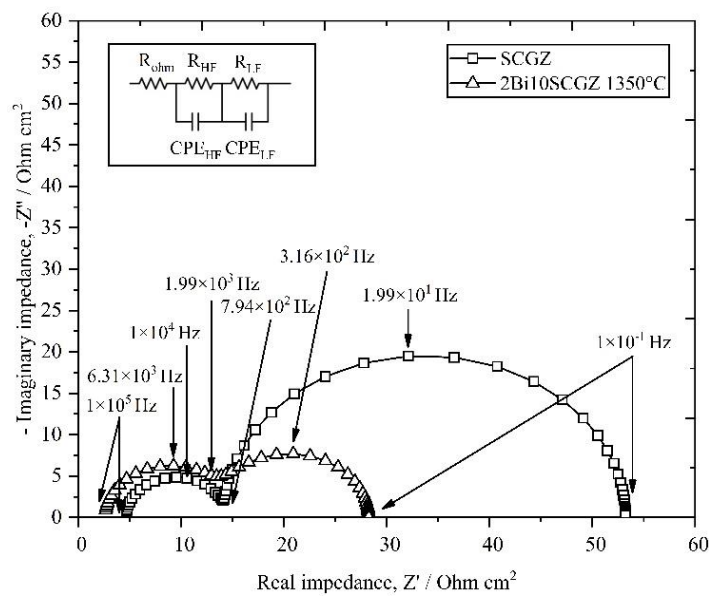


**Fig. 59** EIS response of Pt/SCGZ/Pt and Pt/2Bi10SCGZ/Pt at operating temperature of 800 °C under potentiostatic mode of 1.1 V and H<sub>2</sub>O:H<sub>2</sub> ratio of 70:30

**Table 14** The parameters obtained from the EIS response of Pt/SCGZ/Pt and Pt/2Bi10SCGZ/Pt at operating temperature of 800 °C under potentiostatic mode of 1.1 V and H<sub>2</sub>O:H<sub>2</sub> ratio of 70:30

Parameter	Pt/SCGZ/Pt	Pt/2Bi10SCGZ/Pt
HF intercept ( $\Omega \text{ cm}^2$ )	4.639	2.57
$R_{\text{HF}}$ ( $\Omega \text{ cm}^2$ )	9.512	11.44
$C_{\text{HF}}$ (F $\text{cm}^2$ )	$2.59 \times 10^{-6}$	$1.88 \times 10^{-6}$
$R_{\text{LF}}$ ( $\Omega \text{ cm}^2$ )	39.07	14.25
$C_{\text{LF}}$ (F $\text{cm}^2$ )	$2.2 \times 10^{-4}$	$3.6 \times 10^{-5}$
Total resistance ( $\Omega \text{ cm}^2$ )	53.22	28.26

In accordance with the I/V curve of SCGZ sintered at 1450 °C and 2Bi10SCGZ sintered at 1350 °C presented in Fig. 60, the 2Bi10SCGZ electrolyte exhibited lower resistance in SOEC operation. The hydrogen production rate at the voltage of 1.1 V was calculated by Faraday's law from I/V curve. The 2Bi10SCGZ gave H<sub>2</sub> production rate of  $5.69 \times 10^{-8} \text{ mol s}^{-1}$  higher than that from the SCGZ cell ( $3.58 \times 10^{-8} \text{ mol s}^{-1}$ ). In this study, the different performance of both cells was a result of different electrolyte densification. Apart from electrolyte densification and thickness, the electrolyte performance was reported to depend largely on the operating temperature for thermally activated electrochemical reaction [14] as well as the compatibility between electrolyte and electrode during electrolysis condition [137].

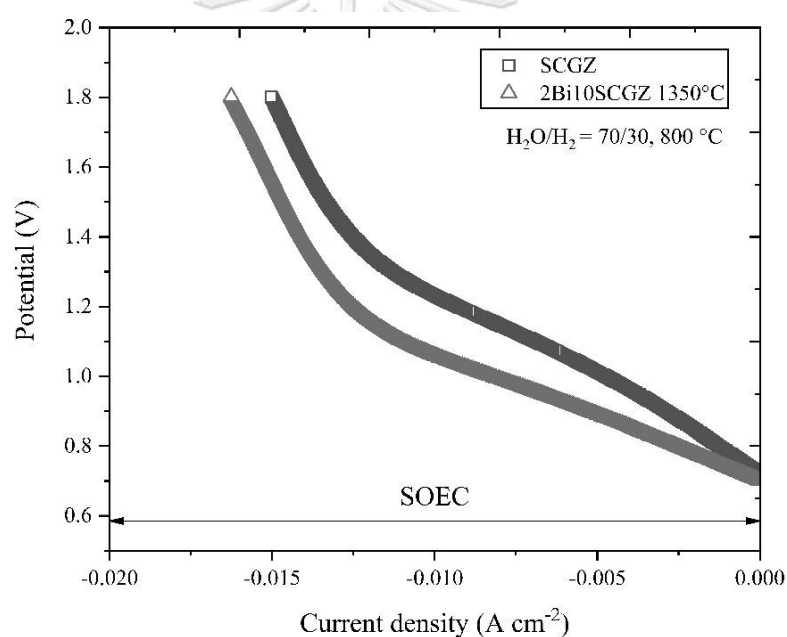


**Fig. 60** I/V curve of Pt/SCGZ/Pt and Pt/2Bi10SCGZ/Pt at operating temperature of 800 °C under steam electrolysis and H<sub>2</sub>O:H<sub>2</sub> ratio of 70:30

#### 4.7.3 Structural stability test

The SCGZ and 2Bi10SCGZ pellet was annealed under 800 °C for 48 hours to investigate structural stability at SOEC operating temperature. XRD patterns of both electrolytes was shown in Fig. 61.

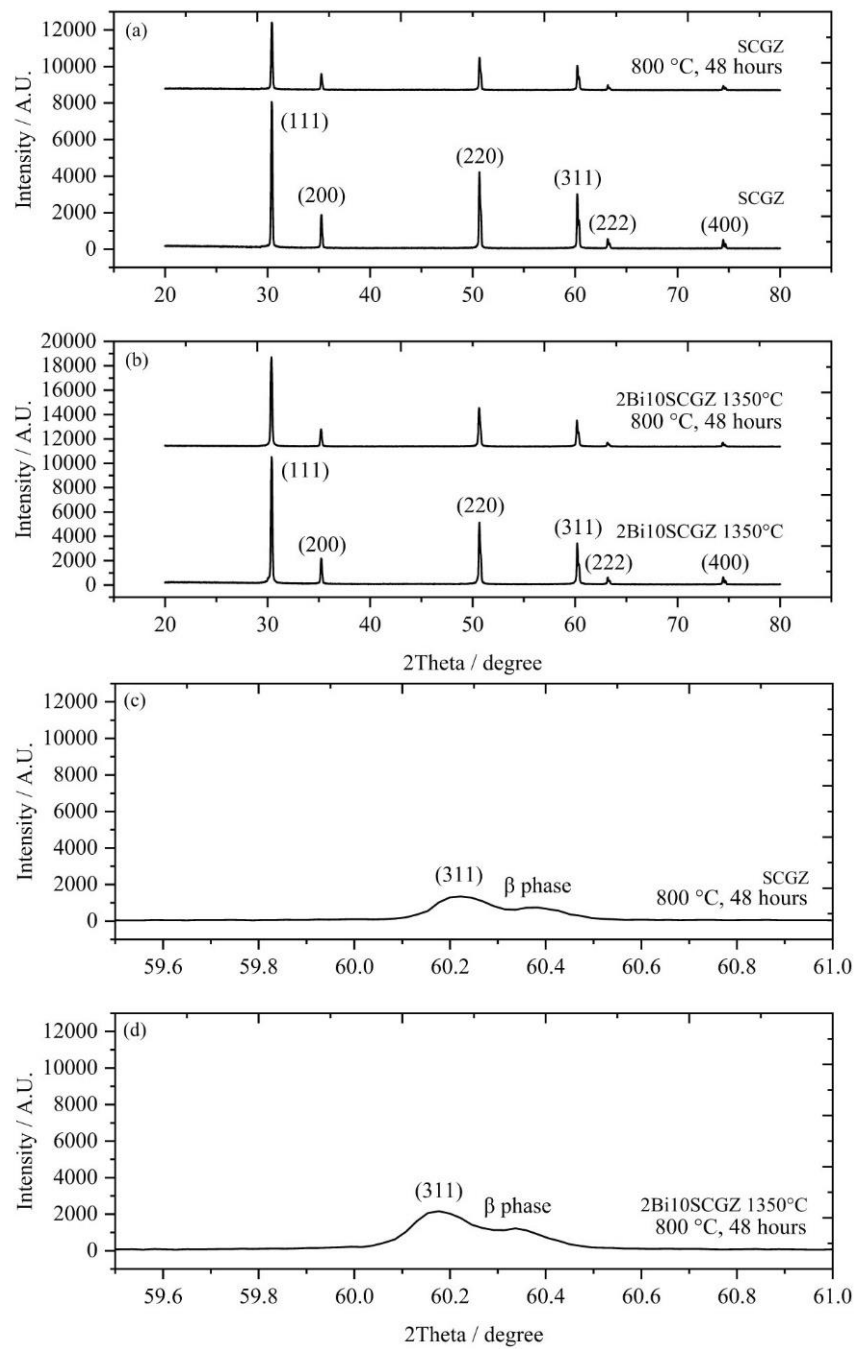


**Fig. 61** The XRD patterns of: (a) SCGZ sintered at 1450 °C; (b) 2Bi10SCGZ sintered at 1350 °C before and after annealing (800 °C for 48 hours); (c) the magnified scale over  $2\theta$  ranging from 59.5° to 61° of SCGZ sintered at 1450 °C after annealing; and, (d) 2Bi10SCGZ sintered at 1350 °C after annealing



The phase existing in SCGZ and 2Bi10SCGZ were still a mixture of rhombohedral and the cubic phase. Additional rhombohedral phase ( $\text{Sc}_2\text{ZrO}_{17}$ ) was not observed for both electrolytes after sample annealing at 800 °C (Fig. 61(a) and (b)). The SEM images of the cell after annealing was presented in Fig. 62. Both electrolytes were still dense without any cracking, and relatively larger grain size was observed after annealing. The EDX-mapping of 2Bi10SCGZ before and after annealing presented a good distribution of Bi element within the electrolyte even after the annealing (Fig 62(c) and (d)).

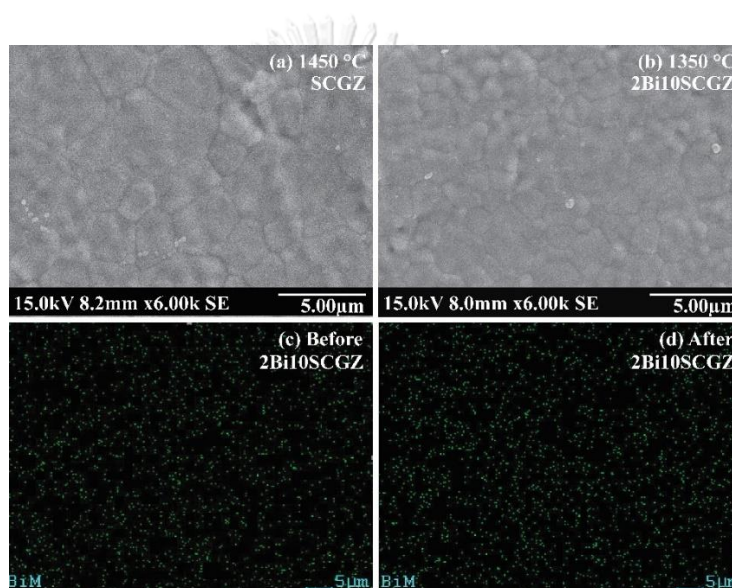


**Fig. 62** SEM images of the electrolyte after annealing at 800°C for 48 hours: (a) SCGZ sintered at 1450 °C, (b) 2Bi10SCGZ sintered at 1350 °C; and EDX-mapping of 2Bi10SCGZ sintered at 1350 °C (c) before and (d) after annealing

The TGA/DSC analysis of SCGZ and 2Bi10SCGZ powder in the range of room temperature to 1000 °C was presented in Fig. 63. Weight loss of the electrolyte powder were 0.75% and 0.74% for SCGZ and 2Bi10SCGZ, respectively. Both electrolytes exhibited slight weight loss during room temperature to 1000 °C, representing the comparable high thermal stability of both electrolytes up to 1000 °C.

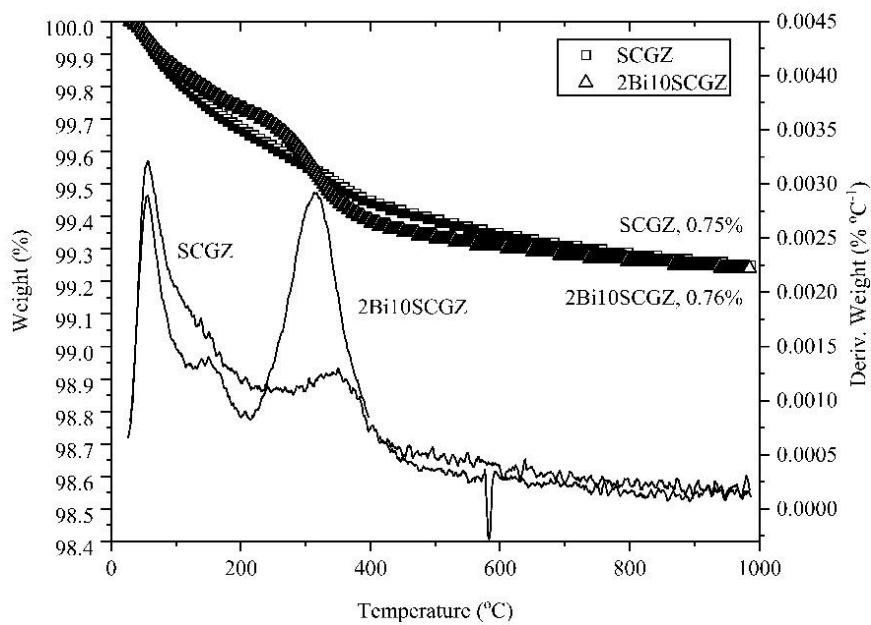


Fig. 63 TGA/DSC of electrolyte powder (SCGZ and 2Bi10SCGZ)



## CHAPTER V

### CONCLUSIONS AND RECOMENDATIONS

#### 5.1 Conclusions

High and durable performance electrolyte is a major issue for SOEC. Therefore, SCGZ was studied with an attempt to gain both performance and chemical stability. The SCGZ were compared with YSZ and GDC electrolyte. Electrolyte-supported cells were fabricated to determine the activation energy of conduction of electrolyte. In this research, bi-layered GDC/YSZ was fabricated to prevent electronic leak current through the GDC electrolyte. The SCGZ and YSZ electrolyte were dense with >95% relative density while GDC was less densified. The electrochemical performance of electrolyte-supported cells was studied. The activation energy of conduction of SCGZ, YSZ and bi-layered GDC/YSZ electrolyte was 65.58 and 81.06 and 87.25 kJ mol<sup>-1</sup>, respectively. SCGZ achieved highest ion conductivity with lowest the activation energy of conduction among the studied electrolytes.

The electrochemical performance of cathode-supported cells having GDC/YSZ, YSZ and SCGZ electrolyte was also studied to measure cells performance and durability toward hydrogen production. The cell performance improved with increasing temperature while steam content insignificantly affected the performance at low potential (<1.1 V). Ni-SCGZ/SCGZ/BSCF cell showed the highest performance among the cells studied, corresponding well with the lowest activation energy of conduction of the material and densified electrolyte structure. However, significant performance decay of the Ni-GDC/YSZ/GDC/BSCF cell was observed after operating under electrolysis mode for 60 hours (0.3 A cm<sup>-2</sup>, 800 °C, and H<sub>2</sub>O:H<sub>2</sub> = 70:30) when compared with Ni-SCGZ/SCGZ/BSCF and Ni-YSZ/YSZ/BSCF which were rather stable under the same operating conditions. Although Ni-SCGZ seemed rather dense due to

Ni coarsening after 60 hours operation, BSCF still remained attaching to the electrolyte.

However, heat treatment during the SCGZ electrolyte fabrication resulted in a low conducting secondary phase (the rhombohedral  $\beta$  phase of  $\text{Sc}_2\text{ZrO}_{17}$ ) together with the main cubic phase. Although the rhombohedral  $\beta$  phase in SCGZ did not affect the durability of the cell in this study, reducing sintering temperature of SCGZ electrolyte to prevent phase transformation into rhombohedral  $\beta$  phase while maintaining densification was studied. When sintered above 1300 °C, the SCGZ electrolyte exhibited a mixture of desired cubic phase and unwanted rhombohedral phase. Thus,  $\text{Bi}_2\text{O}_3$  was added into the SCGZ electrolyte to stabilize the cubic phase. The effect of 1-2 mol%  $\text{Bi}_2\text{O}_3$ -doped SCGZ on the structure and electrochemical performance have been studied. The  $\text{Bi}_2\text{O}_3$  was found to help decrease the unwanted phase and increase densification of the electrolyte pellet, maintaining high ion conductivity of the electrolyte. More amount of  $\text{Bi}_2\text{O}_3$  dopants offered the lower ratio of the rhombohedral to the cubic phase and the higher relative density in the electrolyte. The lower sintering temperature was also found to prevent the unwanted rhombohedral phase. Thus, the lowest sintering temperature which could provide sufficiently densified electrolyte was needed. In this study, a high relative density of the SCGZ electrolyte (>95%) was achieved from 2 mol%  $\text{Bi}_2\text{O}_3$ -doped SCGZ (2Bi10SCGZ) sintered at 1350 °C while it was required up to 1450 °C to achieve the densification for bare SCGZ electrolyte. Moreover, the electrochemical performance of the SOEC was improved by doping  $\text{Bi}_2\text{O}_3$ . In this study, the  $\text{Bi}_2\text{O}_3$  was found to act as both phase stabilizer and sintering additive.

## 5.2 Recommendations

There are several variables affecting phase stabilization of SOEC electrolyte; e.g. thermal properties of ceramic, type of host, the amount of dopant, and fabrication procedures. Therefore, it is worth studying suitable dopant, amount of dopant, and fabrication procedures for SCGZ electrolyte to gain only desired cubic phase and maintain the durability of the cell in prolonged operation. In addition, the

cathode-supported cell for 2Bi10SCGZ electrolyte should also be studied to measure cell performance and durability toward hydrogen production.



## REFERENCES

- [1] Kim-Lohsoontorn P, Laosiripojana N, Bae J. Performance of solid oxide electrolysis cell having bi-layered electrolyte during steam electrolysis and carbon dioxide electrolysis. *Current Applied Physics*. 2011;11:S223-S8.
- [2] Yang S-H, Choi H-W. Fabrication of YSZ/GDC bilayer electrolyte thin film for solid oxide fuel cells. *Transactions on Electrical and Electronic Materials*. 2014;15:189-92.
- [3] Cho S, Kim Y, Kim J-H, Manthiram A, Wang H. High power density thin film SOFCs with YSZ/GDC bilayer electrolyte. *Electrochimica Acta*. 2011;56:5472-7.
- [4] Spiegel C. *Designing and building fuel cells*: Citeseer; 2007.
- [5] Kothari R, Buddhi D, Sawhney R. Comparison of environmental and economic aspects of various hydrogen production methods. *Renewable and Sustainable Energy Reviews*. 2008;12:553-63.
- [6] Ni M, Leung MK, Sumathy K, Leung DY. Potential of renewable hydrogen production for energy supply in Hong Kong. *International Journal of Hydrogen Energy*. 2006;31:1401-12.
- [7] Larminie J, Dicks A, McDonald MS. *Fuel cell systems explained*: J. Wiley Chichester, UK; 2003.
- [8] Udagawa J, Aguiar P, Brandon N. Hydrogen production through steam electrolysis: Control strategies for a cathode-supported intermediate temperature solid oxide electrolysis cell. *Journal of Power Sources*. 2008;180:354-64.
- [9] Dönitz W, Dietrich G, Erdle E, Streicher R. Electrochemical high temperature technology for hydrogen production or direct electricity generation. *International journal of hydrogen energy*. 1988;13:283-7.
- [10] Jensen SH, Larsen PH, Mogensen M. Hydrogen and synthetic fuel production from renewable energy sources. *International Journal of Hydrogen Energy*. 2007;32:3253-7.

- [11] Godula-Jopek A. Hydrogen production: by electrolysis: John Wiley & Sons; 2015.
- [12] Lovera P, Blein F, Vulliet J. Operational Modelling of High Temperature Electrolysis (HTE). Proceedings of the 16th World Hydrogen Energy Conference 2006.
- [13] Wendt H. Electrochemical hydrogen technologies: Electrochemical production and combustion of hydrogen: Elsevier Science Ltd; 1990.
- [14] Gómez SY, Hotza D. Current developments in reversible solid oxide fuel cells. Renewable and Sustainable Energy Reviews. 2016;61:155-74.
- [15] Strickler D, Carlson W. Ionic conductivity of cubic solid solutions in the system  $\text{CaO}-\text{Y}_2\text{O}_3-\text{ZrO}_2$ . Journal of the American Ceramic Society. 1964;47:122-7.
- [16] Ni M, Leung MK, Leung DY. Technological development of hydrogen production by solid oxide electrolyzer cell (SOEC). International Journal of Hydrogen Energy. 2008;33:2337-54.
- [17] Fergus JW. Electrolytes for solid oxide fuel cells. Journal of Power Sources. 2006;162:30-40.
- [18] Kilner JA, Brook RJ. A study of oxygen ion conductivity in doped non-stoichiometric oxides. Solid State Ionics. 1982;6:237-52.
- [19] Yamamoto O, Arachi Y, Sakai H, Takeda Y, Imanishi N, Mizutani Y, et al. Zirconia based oxide ion conductors for solid oxide fuel cells. Ionics. 1998;4:403-8.
- [20] Strickler D, Carlson W. Electrical conductivity in the  $\text{ZrO}_2$ -rich region of several  $\text{M}_2\text{O}_3-\text{ZrO}_2$  systems. Journal of the American Ceramic Society. 1965;48:286-9.
- [21] Arachi Y, Sakai H, Yamamoto O, Takeda Y, Imanishi N. Electrical conductivity of the  $\text{ZrO}_2-\text{Ln}_2\text{O}_3$  (Ln=lanthanides) system. Solid State Ionics. 1999;121:133-9.
- [22] Kharton VV, Naumovich EN, Vecher AA. Research on the electrochemistry of oxygen ion conductors in the former Soviet Union. I.  $\text{ZrO}_2$ -based ceramic materials. Journal of Solid State Electrochemistry. 1999;3:61-81.
- [23] Tianshu Z, Hing P, Huang H, Kilner J. Ionic conductivity in the  $\text{CeO}_2-\text{Gd}_2\text{O}_3$  system

( $0.05 \leq \text{Gd/Ce} \leq 0.4$ ) prepared by oxalate coprecipitation. *Solid State Ionics*. 2002;148:567-73.

[24] Yamamoto O, Arati Y, Takeda Y, Imanishi N, Mizutani Y, Kawai M, et al. Electrical conductivity of stabilized zirconia with ytterbia and scandia. *Solid State Ionics*. 1995;79:137-42.

[25] Chiba R, Yoshimura F, Yamaki J, Ishii T, Yonezawa T, Endou K. Ionic conductivity and morphology in  $\text{Sc}_2\text{O}_3$  and  $\text{Al}_2\text{O}_3$  doped  $\text{ZrO}_2$  films prepared by the sol-gel method. *Solid State Ionics*. 1997;104:259-66.

[26] Haering C, Roosen A, Schichtl H, Schnöller M. Degradation of the electrical conductivity in stabilised zirconia system: Part II: Scandia-stabilised zirconia. *Solid State Ionics*. 2005;176:261-8.

[27] Haering C, Roosen A, Schichtl H, Schnöller M. Degradation of the electrical conductivity in stabilised zirconia system: Part II: Scandia-stabilised zirconia. *Solid State Ionics*. 2005;176:261-8.

[28] Liu T, Zhang X, Wang X, Yu J, Li L. A review of zirconia-based solid electrolytes. *Ionics*. 2016;22:2249-62.

[29] Wang Z, Cheng M, Bi Z, Dong Y, Zhang H, Zhang J, et al. Structure and impedance of  $\text{ZrO}_2$  doped with  $\text{Sc}_2\text{O}_3$  and  $\text{CeO}_2$ . *Materials Letters*. 2005;59:2579-82.

[30] Lei Z, Zhu Q. Low temperature processing of dense nanocrystalline scandia-doped zirconia (ScSZ) ceramics. *Solid State Ionics*. 2005;176:2791-7.

[31] Shin HC, Yu JH, Lim KT, Lee HL, Baik KH, Shin HC, et al. Effects of Partial Substitution of  $\text{CeO}_2$  with  $\text{M}_2\text{O}_3$  (M= Yb, Gd, Sm) on Electrical Degradation of  $\text{Sc}_2\text{O}_3$  and  $\text{CeO}_2$  Co-doped  $\text{ZrO}_2$ . *Journal of the Korean Ceramic Society*. 2016;53:500-5.

[32] Kumar CS, Bauri R. Enhancing the phase stability and ionic conductivity of scandia stabilized zirconia by rare earth co-doping. *Journal of Physics and Chemistry of Solids*. 2014;75:642-50.

[33] Yarmolenko S, Sankar J, Bernier N, Klimov M, Kapat J, Orlovskaya N. Phase stability



and sintering behavior of 10 mol%  $\text{Sc}_2\text{O}_3$ -1 mol%  $\text{CeO}_2$ - $\text{ZrO}_2$  ceramics. *Journal of fuel cell science and technology*. 2009;6.

[34] Hirano M, Oda T, Ukai K, Mizutani Y. Effect of  $\text{Bi}_2\text{O}_3$  additives in Sc stabilized zirconia electrolyte on a stability of crystal phase and electrolyte properties. *Solid State Ionics*. 2003;158:215-23.

[35] Bai B, Sammes N, Smirnova A. Physical and electrochemical characterization of  $\text{Bi}_2\text{O}_3$ -doped scandia stabilized zirconia. *Journal of power sources*. 2008;176:76-81.

[36] Horita T, Kawada T, Sakai N, Yokokawa H, Dokiya M. Low temperature fabrication of (Y, Gd, Sm)-doped ceria electrolyte. *Solid State Ionics*. 1996;86:1255-8.

[37] Li N. The Interaction of LSM-YSZ Composite and Improvement of the Solid Oxide Cell Durability by Mn-modified YSZ. 2014.

[38] Zhu S, Wang Y, Rao Y, Zhan Z, Xia C. Chemically-induced mechanical instability of samaria-doped ceria electrolyte for solid oxide electrolysis cells. *International journal of hydrogen energy*. 2014;39:12440-7.

[39] Mogensen M, Sammes NM, Tompsett GA. Physical, chemical and electrochemical properties of pure and doped ceria. *Solid State Ionics*. 2000;129:63-94.

[40] Steele BCH. Appraisal of  $\text{Ce}_{1-y}\text{Gd}_y\text{O}_{2-y/2}$  electrolytes for IT-SOFC operation at 500°C. *Solid State Ionics*. 2000;129:95-110.

[41] Kim S-G, Yoon SP, Nam SW, Hyun S-H, Hong S-A. Fabrication and characterization of a YSZ/YDC composite electrolyte by a sol-gel coating method. *Journal of Power Sources*. 2002;110:222-8.

[42] Doenitz W, Schmidberger R, Steinheil E, Streicher R. Hydrogen production by high temperature electrolysis of water vapour. *International Journal of Hydrogen Energy*. 1980;5:55-63.

[43] Iwahara H, Uchida H, Yamasaki I. High-temperature steam electrolysis using  $\text{SrCeO}_3$ -based proton conductive solid electrolyte. *International Journal of Hydrogen Energy*.

1987;12:73-7.

[44] Prakash BS, Kumar SS, Aruna S. Properties and development of Ni/YSZ as an anode material in solid oxide fuel cell: a review. *Renewable and Sustainable Energy Reviews*. 2014;36:149-79.

[45] Chan SH. A review of anode materials development in solid oxide fuel cells. *Journal of materials science*. 2004;39:4405-39.

[46] Lim HH, Sulistya E, Wong MY, Salamatinia B, Horri BA. Ceramic Nanocomposites for Solid Oxide Fuel Cells. *Sol-gel Based Nanoceramic Materials: Preparation, Properties and Applications*: Springer; 2017. p. 157-83.

[47] Islam S, Hill JM. Barium oxide promoted Ni/YSZ solid-oxide fuel cells for direct utilization of methane. *Journal of Materials Chemistry A*. 2014;2:1922-9.

[48] Kim-Lohsoontorn P, Brett D, Laosiripojana N, Kim Y, Bae J. Performance of solid oxide electrolysis cells based on composite  $\text{La}_{0.8}\text{Sr}_{0.2}\text{MnO}_{3-\delta}$ -yttria stabilized zirconia and  $\text{Ba}_{0.5}\text{Sr}_{0.5}\text{Co}_{0.8}\text{Fe}_{0.2}\text{O}_{3-\delta}$  oxygen electrodes. *International Journal of hydrogen energy*. 2010;35:3958-66.

[49] Laguna-Bercero M. Recent advances in high temperature electrolysis using solid oxide fuel cells: A review. *Journal of Power sources*. 2012;203:4-16.

[50] Jin C, Yang C, Zhao F, Cui D, Chen F.  $\text{La}_{0.75}\text{Sr}_{0.25}\text{Cr}_{0.5}\text{Mn}_{0.5}\text{O}_3$  as hydrogen electrode for solid oxide electrolysis cells. *International journal of hydrogen energy*. 2011;36:3340-6.

[51] Liu Q, Yang C, Dong X, Chen F. Perovskite  $\text{Sr}_2\text{Fe}_{1.5}\text{Mo}_{0.5}\text{O}_{6-\delta}$  as electrode materials for symmetrical solid oxide electrolysis cells. *International Journal of Hydrogen Energy*. 2010;35:10039-44.

[52] Ge X, Zhang L, Fang Y, Zeng J, Chan SH. Robust solid oxide cells for alternate power generation and carbon conversion. *RSC advances*. 2011;1:715-24.

[53] Yang X, Irvine JT.  $(\text{La}_{0.75}\text{Sr}_{0.25})_{0.95}\text{Mn}_{0.5}\text{Cr}_{0.5}\text{O}_3$  as the cathode of solid oxide electrolysis cells for high temperature hydrogen production from steam. *Journal of*

Materials Chemistry. 2008;18:2349-54.

[54] Ebbesen SD, Jensen SH, Hauch A, Mogensen MB. High temperature electrolysis in alkaline cells, solid proton conducting cells, and solid oxide cells. Chemical reviews. 2014;114:10697-734.

[55] Pratihari SK, Dassharma A, Maiti HS. Properties of Ni/YSZ porous cermets prepared by electroless coating technique for SOFC anode application. Journal of materials science. 2007;42:7220-6.

[56] Pratihari S, Basu RN, Mazumder S, Maiti HS. Electrical conductivity and microstructure of Ni-YSZ anode prepared by liquid dispersion method. ECS Proceedings Volumes. 1999;1999:513-21.

[57] Somalu MR, Yufit V, Cumming D, Lorente E, Brandon NP. Fabrication and characterization of Ni/ScSZ cermet anodes for IT-SOFCs. International Journal of Hydrogen Energy. 2011;36:5557-66.

[58] Mingyi L, Bo Y, Jingming X, Jing C. Influence of pore formers on physical properties and microstructures of supporting cathodes of solid oxide electrolysis cells. International Journal of Hydrogen Energy. 2010;35:2670-4.

[59] Clemmer RMC, Corbin SF. The influence of pore and Ni morphology on the electrical conductivity of porous Ni/YSZ composite anodes for use in solid oxide fuel cell applications. Solid State Ionics. 2009;180:721-30.

[60] Jiang SP. Development of lanthanum strontium manganite perovskite cathode materials of solid oxide fuel cells: a review. Journal of Materials Science. 2008;43:6799-833.

[61] Fleig J. Solid oxide fuel cell cathodes: Polarization mechanisms and modeling of the electrochemical performance. Annual Review of Materials Research. 2003;33:361-82.

[62] Van Roosmalen J, Cordfunke E. The defect chemistry of  $\text{LaMnO}_{3\pm\delta}$ : 4. Defect model for  $\text{LaMnO}_{3+\delta}$ . Journal of Solid State Chemistry. 1994;110:109-12.

- [63] Kuo J, Anderson H, Sparlin D. Oxidation-reduction behavior of undoped and Sr-doped  $\text{LaMnO}_3$ : Defect structure, electrical conductivity, and thermoelectric power. *Journal of Solid State Chemistry*. 1990;87:55-63.
- [64] Bo Y, Wenqiang Z, Jingming X, Jing C. Status and research of highly efficient hydrogen production through high temperature steam electrolysis at INET. *International Journal of Hydrogen Energy*. 2010;35:2829-35.
- [65] Kim J-D, Kim G-D, Moon J-W, Lee H-W, Lee K-T, Kim C-E. The effect of percolation on electrochemical performance. *Solid State Ionics*. 2000;133:67-77.
- [66] Wilson JR, Cronin JS, Duong AT, Rukes S, Chen H-Y, Thornton K, et al. Effect of composition of  $(\text{La}_{0.8}\text{Sr}_{0.2}\text{MnO}_3\text{-Y}_2\text{O}_3\text{-stabilized ZrO}_2)$  cathodes: Correlating three-dimensional microstructure and polarization resistance. *Journal of Power Sources*. 2010;195:1829-40.
- [67] Østergård M, Clausen C, Bagger C, Mogensen M. Manganite-zirconia composite cathodes for SOFC: Influence of structure and composition. *Electrochimica acta*. 1995;40:1971-81.
- [68] Eguchi K, Hataishi T, Arai H. Power generation and steam electrolysis characteristics of an electrochemical cell with a zirconia-or ceria-based electrolyte. *Solid State Ionics*. 1996;86:1245-9.
- [69] Chroneos A, Yildiz B, Tarancón A, Parfitt D, Kilner JA. Oxygen diffusion in solid oxide fuel cell cathode and electrolyte materials: mechanistic insights from atomistic simulations. *Energy & Environmental Science*. 2011;4:2774-89.
- [70] Rembelski D, Viricelle J-P, Combemale L, Rieu M. Characterization and comparison of different cathode materials for SC-SOFC: LSM, BSCF, SSC, and LSCF. *Fuel Cells*. 2012;12:256-64.
- [71] Petric A, Huang P, Tietz F. Evaluation of La-Sr-Co-Fe-O perovskites for solid oxide fuel cells and gas separation membranes. *Solid State Ionics*. 2000;135:719-25.
- [72] Bo Y, Wenqiang Z, Jingming X, Jing C. Microstructural characterization and

electrochemical properties of  $\text{Ba}_{0.5}\text{Sr}_{0.5}\text{Co}_{0.8}\text{Fe}_{0.2}\text{O}_{3-\delta}$  and its application for anode of SOEC. International journal of hydrogen energy. 2008;33:6873-7.

[73] Kim Y-M, Kim-Lohsoontorn P, Baek S-W, Bae J. Electrochemical performance of unsintered  $\text{Ba}_{0.5}\text{Sr}_{0.5}\text{Co}_{0.8}\text{Fe}_{0.2}\text{O}_{3-\delta}$ ,  $\text{La}_{0.6}\text{Sr}_{0.4}\text{Co}_{0.8}\text{Fe}_{0.2}\text{O}_{3-\delta}$ , and  $\text{La}_{0.8}\text{Sr}_{0.2}\text{MnO}_{3-\delta}$  cathodes for metal-supported solid oxide fuel cells. International Journal of Hydrogen Energy. 2011;36:3138-46.

[74] Brisse A, Schefold J, Zahid M. High temperature water electrolysis in solid oxide cells. International journal of hydrogen energy. 2008;33:5375-82.

[75] Choi H-J, Na Y-H, Kwak M, Kim TW, Seo D-W, Woo S-K, et al. Development of solid oxide cells by co-sintering of GDC diffusion barriers with LSCF air electrode. Ceramics International. 2017;43:13653-60.

[76] Villas-Boas LA, Goulart CA, Kiminami RHGA, de Souza DPF. A case study of ceramic processing: Microstructural development and electrical properties of  $\text{Ce}_{0.8}\text{Gd}_{0.2}\text{O}_{1.9}$ . Ceramics International. 2020;46:12318-28.

[77] Hayd J, Dieterle L, Guntow U, Gerthsen D, Ivers-Tiffée E. Nanoscaled  $\text{La}_{0.6}\text{Sr}_{0.4}\text{CoO}_{3-\delta}$  as intermediate temperature solid oxide fuel cell cathode: Microstructure and electrochemical performance. Journal of Power Sources. 2011;196:7263-70.

[78] Masjedi-Arani M, Salavati-Niasari M. A simple sonochemical approach for synthesis and characterization of  $\text{Zn}_2\text{SiO}_4$  nanostructures. Ultrasonics Sonochemistry. 2016;29:226-35.

[79] Seeharaj P, Boonchom B, Charoonsuk P, Kim-Lohsoontorn P, Vittayakorn N. Barium zirconate titanate nanoparticles synthesized by the sonochemical method. Ceramics International. 2013;39:S559-S62.

[80] Kim-Lohsoontorn P, Paichitra C, Vorathamthongdee S, Seeharaj P. Low-temperature preparation of  $\text{BaCeO}_3$  through ultrasonic-assisted precipitation for application in solid oxide electrolysis cell. Chemical Engineering Journal. 2015;278:13-8.

[81] Kim-Lohsoontorn P, Tiyapongpattana V, Asarasri N, Seeharaj P, Laosiripojana N.

Preparation of CeO<sub>2</sub> Nano Rods Through a Sonication-Assisted Precipitation. International Journal of Applied Ceramic Technology. 2014;11:645-53.

[82] Badwal S. Zirconia-based solid electrolytes: microstructure, stability and ionic conductivity. Solid State Ionics. 1992;52:23-32.

[83] LIM KT, LEE HL, SHIN HC. Scandia-stabilized zirconia electrolyte for solid oxide fuel cell having improved stability in reducing atmosphere. Google Patents; 2019.

[84] Badwal S, Ciacchi F, Milosevic D. Scandia-zirconia electrolytes for intermediate temperature solid oxide fuel cell operation. Solid State Ionics. 2000;136:91-9.

[85] Kumar A, Jaiswal A, Sanbui M, Omar S. Scandia stabilized zirconia-ceria solid electrolyte ( $x\text{Sc}_1\text{CeSZ}$ ,  $5 < x < 11$ ) for IT-SOFCs: Structure and conductivity studies. Scripta Materialia. 2016;121:10-3.

[86] Arachi Y, Asai T, Yamamoto O, Takeda Y, Imanishi N, Kawate K, et al. Electrical Conductivity of ZrO<sub>2</sub>-Sc<sub>2</sub>O<sub>3</sub> Doped with HfO<sub>2</sub>, CeO<sub>2</sub>, and Ga<sub>2</sub>O<sub>3</sub>. Journal of the Electrochemical Society. 2001;148:A520-A3.

[87] Fini D, Badwal SPS, Giddey S, Kulkarni AP, Bhattacharya S. Evaluation of Sc<sub>2</sub>O<sub>3</sub>-CeO<sub>2</sub>-ZrO<sub>2</sub> electrolyte-based tubular fuel cells using activated charcoal and hydrogen fuels. Electrochimica Acta. 2018;259:143-50.

[88] Sherif SA, Goswami DY, Stefanakos EK, Steinfeld A. Handbook of hydrogen energy: CRC Press New York, NY, USA.; 2014.

[89] Omar S, Najib WB, Bonanos N. Conductivity ageing studies on 1M10ScSZ ( $M^{4+} = \text{Ce}, \text{Hf}$ ). Solid State Ionics. 2011;189:100-6.

[90] Yasuda K, Uemura K, Shiota T. Sintering and mechanical properties of gadolinium-doped ceria ceramics. Journal of Physics: Conference Series: IOP Publishing; 2012. p. 012006.

[91] Mehranjani A, Cumming D, Sinclair D, Rothman R. Low-temperature co-sintering for fabrication of zirconia/ceria bi-layer electrolyte via tape casting using a Fe<sub>2</sub>O<sub>3</sub> sintering

aid. Journal of the European Ceramic Society. 2017;37:3981-93.

[92] Irvine JT, Dobson JW, Politova T, Martín SG, Shenouda A. Co-doping of scandia-zirconia electrolytes for SOFCs. Faraday discussions. 2007;134:41-9.

[93] Xue QN, Wang LG, Huang XW, Zhang JX, Zhang H. Influence of codoping on the conductivity of Sc-doped zirconia by first-principles calculations and experiments. Materials & Design. 2018;160:131-7.

[94] DS VT, Padala PR, Renju U. Influence of aliovalent cation substitution on structural and electrical properties of  $Gd_2(Zr_{1-x}M_x)2O_{7-\delta}$  (M= Sc, Y) systems. RSC Advances. 2015;5:88675-85.

[95] Vijaya Lakshmi V, Bauri R, Gandhi AS, Paul S. Synthesis and characterization of nanocrystalline ScSZ electrolyte for SOFCs. International Journal of Hydrogen Energy. 2011;36:14936-42.

[96] Kan Y, Li S, Wang P, Zhang G-J, Van der Biest O, Vleugels J. Preparation and conductivity of  $Yb_2O_3$ - $Y_2O_3$  and  $Gd_2O_3$ - $Y_2O_3$  co-doped zirconia ceramics. Solid State Ionics. 2008;179:1531-4.

[97] Hong S, Son J, Lim Y, Yang H, Prinz FB, Kim Y-B. A homogeneous grain-controlled ScSZ functional layer for high performance low-temperature solid oxide fuel cells. Journal of Materials Chemistry A. 2018;6:16506-14.

[98] Cho GY, Lee YH, Hong SW, Bae J, An J, Kim YB, et al. High-performance thin film solid oxide fuel cells with scandia-stabilized zirconia (ScSZ) thin film electrolyte. International Journal of Hydrogen Energy. 2015;40:15704-8.

[99] Murata K, Fukui T, Abe H, Naito M, Nogi K. Morphology control of  $La(Sr)Fe(Co)O_{3-a}$  cathodes for IT-SOFCs. Journal of Power Sources. 2005;145:257-61.

[100] Dias T, Souza DPFd. Electrical and microstructural characterization of Gd-doped Ceria/Y-doped Zirconia bi-layer electrolyte prepared by tape casting. Matéria (Rio de Janeiro). 2017;22.

[101] Irvine JT, Sinclair DC, West AR. Electroceramics: characterization by impedance

spectroscopy. *Advanced Materials*. 1990;2:132-8.

[102] Fan H, Han M. Improved performance and stability of Ag-infiltrated nanocomposite  $\text{La}_{0.6}\text{Sr}_{0.4}\text{Co}_{0.2}\text{Fe}_{0.8}\text{O}_{3-\delta}-(\text{Y}_2\text{O}_3)_{0.08}(\text{ZrO}_2)_{0.92}$  oxygen electrode for  $\text{H}_2\text{O}/\text{CO}_2$  co-electrolysis. *Journal of Power Sources*. 2016;336:179-85.

[103] Sikalidis C. *Advances in ceramics: synthesis and characterization, processing and specific applications: BoD–Books on Demand*; 2011.

[104] áSakib Khan M, áSaiful Islam M, Bates D. Cation doping and oxygen diffusion in zirconia: a combined atomistic simulation and molecular dynamics study. *Journal of Materials Chemistry*. 1998;8:2299-307.

[105] Coddet P, Amany M-L, Vulliet J, Caillard A, Thomann A-L. YSZ/GDC bilayer and gradient barrier layers deposited by reactive magnetron sputtering for solid oxide cells. *Surface and Coatings Technology*. 2019;357:103-13.

[106] Kim C, Park H, Jang I, Kim S, Kim K, Yoon H, et al. Morphologically well-defined  $\text{Gd}_{0.1}\text{Ce}_{0.9}\text{O}_{1.95}$  embedded  $\text{Ba}_{0.5}\text{Sr}_{0.5}\text{Co}_{0.8}\text{Fe}_{0.2}\text{O}_{3-\delta}$  nanofiber with an enhanced triple phase boundary as cathode for low-temperature solid oxide fuel cells. *Journal of Power Sources*. 2018;378:404-11.

[107] Yan J, A. Nomeli M. *Handbook of Clean Energy Systems, 6 Volume Set* 2015.

[108] Yue X, Irvine JT.  $(\text{La,Sr})(\text{Cr,Mn})\text{O}_3/\text{GDC}$  cathode for high temperature steam electrolysis and steam-carbon dioxide co-electrolysis. *Solid State Ionics*. 2012;225:131-5.

[109] Walch G, Opitz AK, Kogler S, Fleig J. Correlation between hydrogen production rate, current, and electrode overpotential in a solid oxide electrolysis cell with  $\text{La}_{0.6}\text{Sr}_{0.4}\text{FeO}_{3-\delta}$  thin-film cathode. *Monatshefte für Chemie-Chemical Monthly*. 2014;145:1055-61.

[110] Wiedenmann D, Hauch A, Grobóty B, Mogensen M, Vogt UF. Complementary techniques for solid oxide electrolysis cell characterisation at the micro- and nano-scale. *International Journal of Hydrogen Energy*. 2010;35:5053-60.

[111] Zhu Q, Jin T, Wang Y. Thermal expansion behavior and chemical compatibility of



$Ba_xSr_{1-x}Co_{1-y}Fe_yO_{3-\delta}$  with 8YSZ and 20GDC. Solid State Ionics. 2006;177:1199-204.

[112] Hayashi H, Saitou T, Maruyama N, Inaba H, Kawamura K, Mori M. Thermal expansion coefficient of yttria stabilized zirconia for various yttria contents. Solid state ionics. 2005;176:613-9.

[113] Xu Z, Sankar J. Liquid-phase sintering of ScSZ electrolytes for solid oxide fuel cells. ASME 2007 International Mechanical Engineering Congress and Exposition: American Society of Mechanical Engineers Digital Collection; 2007. p. 195-9.

[114] Hirano M, Oda T, Ukai K, Mizutani Y. Suppression of rhombohedral-phase appearance and low-temperature sintering of scandia-doped cubic-zirconia. Journal of the American Ceramic Society. 2002;85:1336-8.

[115] Sarat S, Sammes N, Smirnova A. Bismuth oxide doped scandia-stabilized zirconia electrolyte for the intermediate temperature solid oxide fuel cells. Journal of Power Sources. 2006;160:892-6.

[116] Yeh TH, Kusuma GE, Suresh MB, Chou CC. Effect of sintering process on the microstructures of  $Bi_2O_3$ -doped yttria stabilized zirconia. Materials Research Bulletin. 2010;45:318-23.

[117] Tong J, Clark D, Bernau L, Subramaniyan A, O'Hayre R. Proton-conducting yttrium-doped barium cerate ceramics synthesized by a cost-effective solid-state reactive sintering method. Solid State Ionics. 2010;181:1486-98.

[118] Likhittaphon S, Pukkrueapun T, Seeharaj P, Wetwathana Hartley U, Laosiripojana N, Kim-Lohsoontorn P. Effect of sintering additives on barium cerate based solid oxide electrolysis cell for syngas production from carbon dioxide and steam. Fuel Processing Technology. 2018;173:119-25.

[119] Kimpton J, Randle TH, Drennan J. Investigation of electrical conductivity as a function of dopant-ion radius in the systems  $Zr_{0.75}Ce_{0.08}M_{0.17}O_{1.92}$  (M=Nd, Sm, Gd, Dy, Ho, Y, Er, Yb, Sc). Solid State Ionics. 2002;149:89-98.

[120] Badwal S, Ciacchi F. Oxygen-ion conducting electrolyte materials for solid oxide

fuel cells. *Ionics*. 2000;6:1-21.

[121] Lakshmi VV, Bauri R. Phase formation and ionic conductivity studies on ytterbia co-doped scandia stabilized zirconia ( $0.9\text{ZrO}_2-0.09\text{Sc}_2\text{O}_3-0.01\text{Yb}_2\text{O}_3$ ) electrolyte for SOFCs. *Solid state sciences*. 2011;13:1520-5.

[122] Bai B, McPhee W, Smirnova A, Sammes N. A Comparison and Characterization of  $\text{CeO}_2$ -doped and  $\text{Bi}_2\text{O}_3$ -doped Scandia Stabilized Zirconia as IT-SOFC Electrolytes. *ECS Transactions*. 2007;7.

[123] Orooji Y, Mohassel R, Amiri O, Sobhani A, Salavati-Niasari M.  $\text{Gd}_2\text{ZnMnO}_6/\text{ZnO}$  nanocomposites: Green sol-gel auto-combustion synthesis, characterization and photocatalytic degradation of different dye pollutants in water. *Journal of Alloys and Compounds*. 2020;835:155240.

[124] Accardo G, Bae JK, Yoon SP. Evaluation of the Microstructure and the Electrochemical Properties of  $\text{Ce}_{0.8(1-x)}\text{Gd}_{0.2(1-x)}\text{Cu}_x\text{O}_{[1.9(1-x)+x]}$  Electrolytes for IT-SOFCs. *Applied Sciences*. 2020;10:4573.

[125] Zhu B. Solid oxide fuel cell (SOFC) technical challenges and solutions from nano-aspects. *International Journal of Energy Research*. 2009;33:1126-37.

[126] Sundh A, Molin M, Sjögren G. Fracture resistance of yttrium oxide partially-stabilized zirconia all-ceramic bridges after veneering and mechanical fatigue testing. *Dent Mater*. 2005;21:476-82.

[127] Visvanichkul, Peng O, Ngampuengpis, Sirimungkalakul, Puengjinda P, Jiwanuruk T, et al. Effect of CuO as Sintering Additive in Scandium Cerium and Gadolinium-Doped Zirconia-Based Solid Oxide Electrolysis Cell for Steam Electrolysis. *Processes*. 2019;7:868.

[128] Leng H, Nie J, Luo J. Combining cold sintering and  $\text{Bi}_2\text{O}_3$ -Activated liquid-phase sintering to fabricate high-conductivity Mg-doped NASICON at reduced temperatures. *Journal of Materiomics*. 2019;5:237-46.

[129] Meenakshi P, Promila K, Sitharaman U, Nagarajan R. Evaluation of solid solution

formation between  $\text{ThO}_2$  and  $\delta\text{-Bi}_2\text{O}_3$  by molecular precursor route. *Materials Research Bulletin*. 2018;107:66-73.

[130] Fisher JG, Le PG, Han H-S, Jeong S-M, de Leon NKC, Lopez AD. Use of Vanadium Oxide as a Liquid Phase Sintering Aid for Barium Hexaferrite. *Journal of Magnetism*. 2018;23:409-15.

[131] Lee JG, Yoon H. Synthesis and Characterization of Cu- and Co-Doped  $\text{Bi}_4\text{V}_2\text{O}_{11}$  for Intermediate-Temperature Solid Oxide Fuel Cell Electrolytes by Carbonate Coprecipitation. *Japanese Journal of Applied Physics*. 2011;50.

[132] Puchalska M, Zych E, Bolek P. Luminescences of  $\text{Bi}^{3+}$  and  $\text{Bi}^{2+}$  ions in Bi-doped  $\text{CaAl}_4\text{O}_7$  phosphor powders obtained via modified Pechini citrate process. *Journal of Alloys and Compounds*. 2019;806:798-805.

[133] Wang F, Lyu Y, Chu D, Jin Z, Zhang G, Wang D. The electrolyte materials for SOFCs of low-intermediate temperature. *Materials Science and Technology*. 2019;35:1551-62.

[134] Mori M, Liu Y, Ma S, Hashimoto S-i, Yasumoto K. Effects of Bi Addition on Sintering and Electrical Properties of Scandia Stabilized Zirconia as Intermediate-Temperature SOFC Electrolyte. *Electrochemistry*. 2009;77:184-9.

[135] Bai B, Sammes NM, Smirnova AL, Tompsett G. Characterization of scandia stabilized zirconia doped with various  $\text{Bi}_2\text{O}_3$  additions as an intermediate temperature solid oxide fuel cell electrolyte. *Journal of Fuel Cell Science and Technology*. 2010;7.

[136] Shaofei W, Liquan C. Interfacial transport in lithium-ion conductors. 2016.

[137] Yoon KJ, Lee S-i, An H, Kim J, Son J-W, Lee J-H, et al. Gas transport in hydrogen electrode of solid oxide regenerative fuel cells for power generation and hydrogen production. *International Journal of Hydrogen Energy*. 2014;39:3868-78.



APPENDIX

จุฬาลงกรณ์มหาวิทยาลัย  
**CHULALONGKORN UNIVERSITY**

## APPENDIX A

### LATTICE PARAMETER AND CELL PROPERTIES CALCULATION

#### 1. Lattice parameter calculation

The Lattice parameter  $\text{Bi}_2\text{O}_3$ -doped SCGZ samples were calculated by using Bragg's law equation to find out the spacing of the crystal layers, Eq. (A.1):

$$n\lambda = 2d_{hkl}\sin\theta \quad (\text{A.1})$$

$n$  = an integer

$\lambda$  = the wavelength of the x-ray ( $\text{CuK}\alpha = 1.5406 \text{ \AA}$ )

$d_{hkl}$  = the spacing of the crystal layers (hkl)

$\theta$  = the angle between incident ray and the scatter plane

The value of spacing of the crystal layers ( $d_{hkl}$ ) was substituted in lattice parameter equation for cubic structure, as shown in Eq. (A.2)

$$a = d_{hkl}\sqrt{h^2+k^2+l^2} \quad (\text{A.2})$$

$a$  = lattice parameter

$d_{hkl}$  = the spacing of the crystal layers (hkl)

Example of lattice parameter calculation was presented following equation mention earlier. XRD pattern of 1 mol%  $\text{Bi}_2\text{O}_3$ -doped SCGZ (1Bi10SCGZ) was shown in Fig. A.1.

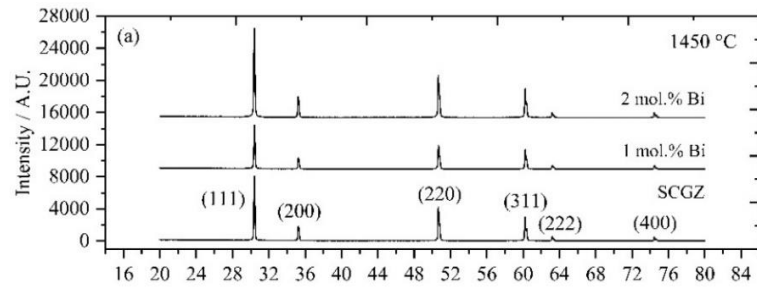


Fig. A.1 XRD patterns of the SCGZ with different  $\text{Bi}_2\text{O}_3$  contents sintered at 1450 °C

First,  $n$  and  $\lambda$  were used to substituted in Bragg's law equation. 4 equations were calculated for each  $\theta$  value from 4 highest cubic peak, giving 4 parameters ( $d_{hkl}$ ) to calculate the lattice parameter.

For  $2\theta = 30.4161$ ; Using Eq. (A.1)

$$n\lambda = 2d_{hkl}\sin\theta$$

$$(1)(1.5406) = 2d_{hkl}\sin(15.2081)$$

$$d_{hkl} = 2.9364 \text{ \AA}$$

$d_{hkl}$  value together with the spacing of the crystal layers ( $h$ ,  $k$ , and  $l$ ), obtained from JCPDS No. 89-5485 of main cubic phase (ScSZ data), were substituted in the lattice parameter equation (Eq. (A.2)).

$$a = d_{hkl}\sqrt{h^2+k^2+l^2}$$

$$a = (2.9364)\sqrt{1^2+1^2+1^2}$$

$$a = 5.0861 \text{ \AA}$$

The calculated data of spacing of the crystal layers ( $d_{hkl}$ ) and the lattice parameter for 1 mol%  $\text{Bi}_2\text{O}_3$ -doped SCGZ (1Bi10SCGZ) were presented in Tables A.1-2, respectively.

**Table A.1** The calculated data of spacing of the crystal layers ( $d_{hkl}$ ) for 1Bi10SCGZ

Peak	$2\theta$	(hkl)	$d_{hkl}$ (Å)
1	30.4161	(111)	2.9364
2	35.2464	(200)	2.5443
3	50.6760	(220)	1.7999
4	60.2451	(311)	1.5349

**Table A.2** The calculated data of lattice parameter for 1Bi10SCGZ

Peak	$d_{hkl}$ (Å)	(hkl)	a (Å)
1	2.9364	(111)	5.0860
2	2.5443	(200)	5.0886
3	1.7999	(220)	5.0910
4	1.5349	(311)	5.0907
Average lattice parameter			5.0891

## 2. Cell relative density calculation

The percentage of relative density of cell was calculated by following equations (A.3-4). The lattice parameters of SCGZ structure were used for theoretical density calculation. The theoretical density of SCGZ was  $5.67 \text{ g cm}^{-3}$ .

$$\% \text{ Relative density} = \frac{D_{\text{pellet}}}{D_{\text{theoretical}}} \times 100 \quad (\text{A.3})$$

$$D_{\text{pellet}} = \text{Mass of pellet} / \text{Volume of pellet} \quad (\text{A.4})$$

When

$D_{\text{pellet}}$  = density of pellet ( $\text{g cm}^{-3}$ ),

$D_{\text{theoretical}}$  = theoretical density ( $\text{g cm}^{-3}$ )

### 3. Linear shrinkage and volume shrinkage calculation

The percentage of linear and volume shrinkage of cell was also taken from direct measurement of the electrolyte pellet dimension and thickness before and after the sintering, followed by substitution in equation (A.5-6).

$$\% \text{ Linear shrinkage} = \frac{l_2 - l_1}{l_1} \times 100 \quad (\text{A.5})$$

$$\% \text{ Volume shrinkage} = \frac{V_2 - V_1}{V_1} \times 100 \quad (\text{A.6})$$

When

$l_1$  = cell diameter before sintering (cm),

$l_2$  = cell diameter after sintering (cm),

$V_1$  = volume of pellet before sintering ( $\text{cm}^3$ ),

$V_2$  = volume of pellet before sintering ( $\text{cm}^3$ )

### 4. Degree of oxidation (DoO) calculation

The degree of oxidation (DoO) was carried out using equations (A.7) to study the oxidation tolerance of Ni-electrolyte cathode.

$$\text{DoO (t)} = \frac{W(t) - W_1}{W_2 - W_1} \times 100 \quad (\text{A.7})$$

When

$W$  = weight as a function of measurement time (g),

$W_1$  = initial weight (g),

$W_2$  = final weight (g)



## APPENDIX B

### ELECTROCHEMICAL MEASUREMENT CONDITION

The effect of steam to hydrogen ratio at the hydrogen electrode in both electrolytic and galvanic modes was studied. In the experiment, the H<sub>2</sub>O:H<sub>2</sub> was varied over a range of 60:40, 70:30 and 90:10 which controlled by maintaining different gas flow rate to cathode, as shown in Table B.1.

**Table B.1** Gas flow rate to cathode at varied H<sub>2</sub>O:H<sub>2</sub> from 60:40 to 90:10

steam to H <sub>2</sub> ratio	H <sub>2</sub> (mL/min)	N <sub>2</sub> (mL/min)	Steam (mL/min)	Total gas flow to cathode (mL/min)
60:40	100	75	150	325
70:30	75	75	175	325
90:10	25	75	225	325

## APPENDIX C

### ELECTROCHEMICAL CALCULATION

#### 1. Oxygen ion conductivity

Oxygen ion conductivity was calculated from Arrhenius equation:

$$\sigma = \frac{L}{RA} \quad (C.1)$$

When

$\sigma$  = oxygen ion conductivity ( $S\ cm^{-1}$ ),

L = cell thickness (cm),

R = total resistance of cell ( $\Omega$ ),

A = area of electrode ( $cm^2$ )

Total resistance of cell (R) is calculated from the slope of IV curve generated using linear sweep current techniques, as shown in Fig. C.1.

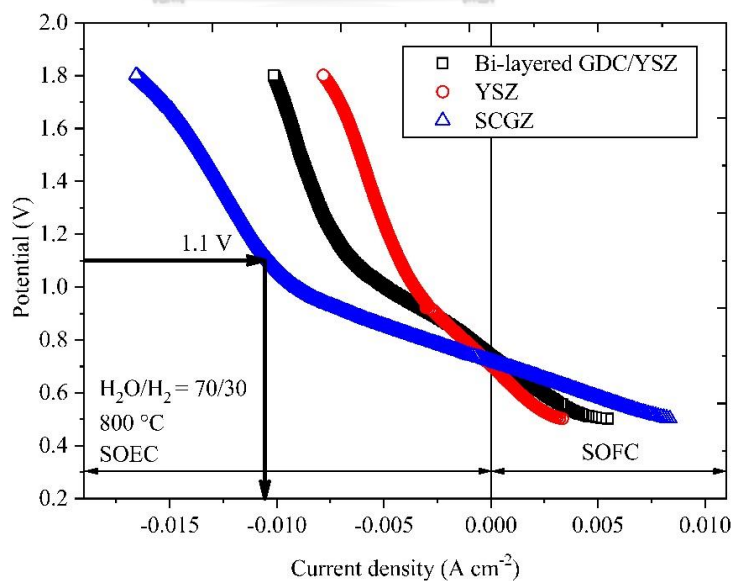


Fig. C.1 I/V response of Pt/electrolyte/Pt when the electrolyte is Bi-layered GDC/YSZ, YSZ and SCGZ, under  $H_2O:H_2$  ratio of 70:30 at 800 °C

For calculation example, the oxygen ion conductivity of Pt/SCGZ/Pt cell was used to be a case study. As shown in Fig. C.1, It can be seen that the slope of SCGZ electrolyte graph (total resistance of the cell) in the range of 1.1 V (SOEC operation) was approximately  $73.54 \Omega \text{ cm}^2$ . After that, the values of cell total resistance (R) and cell thickness (L) were substituted into equation (C.1). It should be noted that the thickness of the cell was 0.16 cm.

$$\sigma = \frac{0.16}{73.54}$$

$$\sigma = 0.002175 \text{ S cm}^{-1}$$

## 2. Activation energy of conduction

Activation energy of conduction equation was presented, Eq. (C.2):

$$\ln(\sigma) = -\frac{E_a}{RT} + \ln\left(\frac{A}{T}\right) \quad (\text{C.2})$$

when

- $\sigma$  = oxygen ion conductivity ( $\text{S cm}^{-1}$ ),
- $E_a$  = activation energy of conduction ( $\text{J mol}^{-1}$ ),
- $R$  = gas constant ( $8.314 \text{ J K}^{-1} \text{ mol}^{-1}$ ),
- $T$  = temperature (K),
- $A$  = area of electrode ( $\text{cm}^2$ )

The activation energy of conduction ( $E_a$ ) was calculated by using the slope of the graph relation between the natural logarithm of oxygen ion conductivity and the inverse of operating temperature, as presented in Fig. C.2.

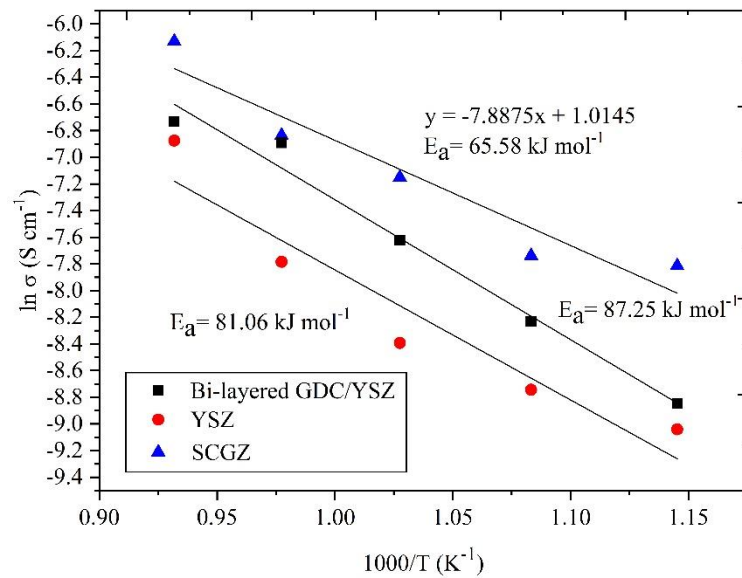


Fig. C.2 Activation energy of conduction ( $E_a$ ) and the conductivity of Bi-layered GDC/YSZ, YSZ and SCGZ electrolyte at various operating temperatures

Fig. C.2 exhibited that the slope of SCGZ electrolyte graph was  $-7.8875$ . Comparing with Eq. (C.2), the slope of the graph represents  $-E_a/R$  (gas constant) value. Therefore, the activation energy of conduction was calculated through this relation:

$$\text{Slope of graph} = \frac{-E_a}{R}$$

$$-7.8875 = \frac{-E_a}{8.314}$$

$$E_a = (-7.8875)(-8.314)$$

$$E_a = 65.5766 \text{ kJ mol}^{-1}$$

### 3. Hydrogen production rate

Faraday's laws of electrolysis equation was used to calculate the hydrogen production rate in theoretical, as presented in Eq. (C.3).

$$m = \frac{I}{nF} \quad (\text{C.3})$$

When

$m$  = amount of generated mole,

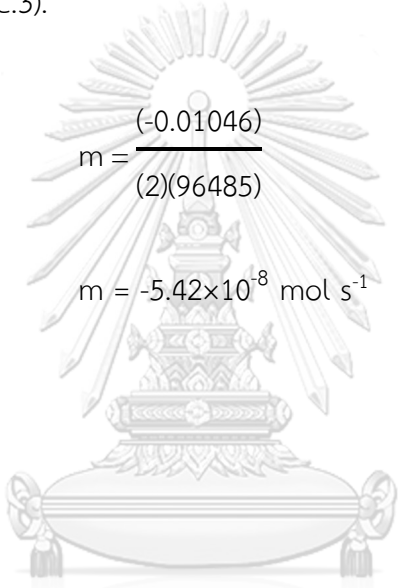
$I$  = current (A or Coulomb  $s^{-1}$ ),

$n$  = amount of electron generated in reaction,

$F$  = Faraday's constant ( $96,485 \text{ C mol}^{-1}$ )

As mention earlier in Fig. C.1, The current ( $I$ ) of Pt/SCGZ/Pt cell was  $-0.01046 \text{ A}$  measured at a constant potential of  $1.1 \text{ V}$  (SOEC operation). The current of the cell ( $I$ ) was substituted in Eq. (C.3).

$$m = \frac{(-0.01046)}{(2)(96485)}$$

$$m = -5.42 \times 10^{-8} \text{ mol s}^{-1}$$


จุฬาลงกรณ์มหาวิทยาลัย  
CHULALONGKORN UNIVERSITY

## VITA

**NAME** Parintorn Temluxame

**DATE OF BIRTH** 05 December 1995

**PLACE OF BIRTH** Bangkok, Thailand

**INSTITUTIONS ATTENDED** Mahidol University, 2014-2018  
Bachelor of Engineering (B.Eng.)

Chulalongkorn University, 2018-2020  
Master of Engineering (M.Eng.)

**HOME ADDRESS** Nimitmai 12, Sai kong din, Klong sam wa, Bangkok  
Email: parintornmookk@gmail.com

**PUBLICATION** P. Temluxame, P. Puengjinda, S. Peng-ont, W. Ngampuengpis, N. Sirimungkalakul, T. Jiwanuruk, T. Sornchamni, P. Kim-Lohsoontorn, Comparison of ceria and zirconia based electrolyte for solid oxide electrolysis cells. International Journal of Hydrogen Energy. 2020.

P. Temluxame, N. Laosiripojana, S. Assabumrungrat, P. Puengjinda, P. Kim-Lohsoontorn, Phase Transformation and Electrical Properties of Bismuth Oxide Doped Scandium Cerium and Gadolinium Stabilized Zirconia (0.5Gd0.5Ce10ScSZ) for Solid Oxide Electrolysis Cell. International Journal of Hydrogen Energy. 2020.